Available online at www.sciencedirect.com
ScienceDirect
Materials Science and Engineering R 54 (2006) 49–120
Reports: A Review Journal
www.elsevier.com/locate/mser

Ion implantation of organisms

Huiyun Feng [a,b], Zengliang Yu [a,*], Paul K. Chu [b,**]

[a] *Key Laboratory of Ion Beam Bioengineering, Institute of Plasma Physics, Chinese Academy of Sciences, P.O. Box 1126, Hefei 230031, Anhui, China*

[b] *Department of Physics and Material Science, City University of Hong Kong, Tat Chee Avenue, Kowloon, Hong Kong, China*

Abstract

This paper describes keV ion interactions with bio-molecules and organisms by illustrating the general concepts and discussing emerging applications. We begin with a systematic discussion on the theories and fundamental issues pertaining to this young and promising field, including radiation damage and sputtering of organisms, chemical reactions between incident ions and biological targets, ion penetration and distribution in plant seeds, fragmentation of biological building blocks, disruption of plasmid DNA under ion impact, and gene mutation induced by keV ions in plants and microbes. Recent developments in experimental methodologies which play an important role in driving the technology and the scientific progress are reviewed. Representative applications and achievements in agriculture, fermentation industry and biology are described and finally, outstanding questions and future research directions are presented and discussed.

PACS : 87.50.Gi; 87.65.+y; 82.39.Rt; 87.80.−y

Keywords: Low-energy ions; Biomolecules; Organisms; Agriculture; Fermentation industry

Contents

* Corresponding author. Tel.: +86 551 5592189; fax: +86 551 5591310.
** Corresponding author. Tel.: +852 27887724; fax: +852 27889549.
E-mail addresses: zlyu@ipp.ac.cn (Z. Yu), paul.chu@cityu.edu.hk (P.K. Chu).

0927-796X/$ – see front matter © 2006 Elsevier B.V. All rights reserved.
doi:10.1016/j.mser.2006.11.001

1. Introduction

An ion is an atom or cluster that has acquired a net electrical charge by gaining or losing one or more electrons. Ions were first theorized by Michael Faraday at around 1830 to be the portions of particles that travel either to an anode or cathode under an electric field. An atom or molecule becomes a positive ion when it loses one or more electrons due to ionization, and it becomes a negative ion when it captures one or more electrons. If an ion is stripped of a large number of electrons, it becomes a highly/multiply charged ion.

Ions are essential to life. Among the approximately 100 natural elements, about 30 elements are constituents in life systems, including 11 abundant elements (C, H, O, N, P, S, Cl, K, Na, Ca, Mg), 3 transition elements (Fe, Zn, Cu), and 16 trace elements, of which 6 are nonmetallic elements (F, I, Se, Si, As, B) and 10 are metals (Mn, Mo, Co, Cr, V, Ni, Cf, Sn, Pb, Li). Some of these elements are present in the ionic form in organisms. They help to maintain the normal activities in the living system and influence the cellular functions of living organisms by participating in various complicated biochemical processes such as material transport, energy transformation, information exchange, and control of metabolism [1].

Ions can be produced during certain naturally occurring processes [2,3] or in an ion source of man-made machines [4]. In the laboratory, these ions in an ion source have certain kinetic energies by proper acceleration in a vacuum ambient in which ion collisions are reduced. In most applications, after acceleration and mass selection, energetic ions are transported to a reaction chamber where ion–target interactions occur. The physical and chemical processes

in ion–matter interactions are largely dictated by the attributes of both the projectiles such as kinetic energy, mass, and charge state of the incident ions and the mass density, thickness distribution, and so on of the target [5]. In terms of the interaction energy, there are roughly five regimes: thermal (<1 eV), hyperthermal (1–100 eV), low-energy (0.1–10 keV), medium-energy (10–500 keV) and high-energy (>500 keV) [4,6]. In this review, we focus on keV ion interactions with biomolecules and living organisms. We also discuss ion-induced damage and mutagenic effects that are important to environmental safety and human health, origin and evolution of life, and the application of ion beam modification to life sciences.

1.1. Ion–solid interaction

Stopping of energetic ions in matter has been a subject of extensive theoretical and experimental research for almost 100 years. Soon after the discovery of energetic particle emission from radioactive material, there have been interests in how corpuscles are slowed down while traversing matter [7]. Many physical and chemical phenomena associated with the interactions between energetic ions and matter have been observed. The more important ones include energy loss and deceleration while ions penetrate a solid target, generation of bulk and surface damage due to the dissipation of the ion energy, ejection of charged and neutral atoms and molecules from the surface of the target, and other emission processes [8]. The first unified stopping and range theory is the LSS theory proposed by Lindhard, Schaff and Schiott in 1963 [9,10]. This theory is the culmination of theoretical and experimental work conducted in the prior decades and provides a convenient model to calculate ion stopping and range distribution in solids [7]. Nowadays, the LSS model and the Monte Carlo based SRIM (The Stopping and Range of Ions in Solids) code developed by Ziegler [11] are the most widely used programs.

Energetic ion beams are frequently utilized as an analytical tool and modification/fabrication means in physics, chemistry, and material science. For instance, thin films can be deposited onto substrates, inner structures can be revealed by sputtering, mixed interfaces can be created, materials can be doped with different elements, and a multitude of material characterization techniques such as secondary ion mass spectrometry (SIMS) and Rutherford backscattering spectrometry (RBS) have spawned [6,12,13]. In ion beam processing of solid material, ions with energies ranging from eVs to MeVs can be used to produce different effects [14]. The mechanical, electrical, optical, magnetic, and superconducting properties of the target material can be selectively altered by introducing foreign ions. Low-energy and medium-energy ion irradiation is particularly important to the industry such as microelectronics as many doping, etching, surface cleaning, and deposition techniques employ ion beams [13,15,16].

1.2. Ion interaction with biomedical material

Biomaterial has been widely studied and applied. They also play important roles in the development of more effective drug delivery systems for pharmaceuticals [17,18]. After microelectronic material, biomaterial is the next category of matter to which ion beam processing has been successfully applied [19,20]. One common definition of biomaterial is that they are a type of biocompatible materials used in medical devices and intended to interact with a biological system [21]. Stupp, et al. defines that biomaterial is either naturally occurring material in living organisms or material designed to repair human tissues and organs [22]. Another definition is any material, natural or man-made, that comprises a whole or part of a living structure or a biomedical device that performs, augments, or replaces a natural function [23]. Here, for simplicity, the material is classified as biomaterial when some kind of connection is to be or has been established between the material and living organisms. For example, diamond-like-carbon (DLC) coatings and polymeric, glass- and silicone-oxide-based materials adopted in studies of *in vitro* growth of nerve cells and neurons communication are regarded as biomaterials [24,25], and materials that have the potential to be applied to the development of biological instrumentation [26] can be regarded as biomaterials as well. Based on this definition, all living organisms including cells, bacteria, viruses, plant tissues, organs, and their constitutive elements/molecules/polymers should not be included, but they are the focus of this review paper. Therefore, in the context of this review paper, they are also categorized as biomaterials. In addition, water, the most basic constituent in all known forms of life, is included in our scope of biomaterial.

Various types of biomaterial including metals, alloys, ceramics, glasses, polymers and composites have been produced by various types of ion beam processing technologies such as ion implantation, ion beam assisted deposition (IBAD), ion beam texturing, and ion sculpting. Much effort has been made with respect to the design, synthesis, and

fabrication of biomaterial and devices to ensure that they have the appropriate mechanical properties, compatibility, durability, and functionality that suit specific applications, and these properties are largely governed by the surface of the biomaterial [21,23,27,28]. That is to say, the surface structure is a crucial factor and in many examples, the functionality of material can be modified by ion beams. It should be emphasized here that material surfaces must be properly modified so that surface attributes such as biocompatibility is improved while the desirable bulk properties can be retained in order to bode well for biomedical applications [29,30].

1.3. Ion interaction with biomolecules

A biomolecule is a chemical compound that naturally occurs in living organisms. Biomolecules are necessary for the existence of all known forms of life. Life is actually regulated at the cellular level by the intricate interplay between elements, individual molecules, and molecular complexes. Trace elements in a living system act as the coordination centers for building or stabilizing the structure of enzymes and proteins [31]. DNA, proteins, oligosaccharides, peptides, lipids, hormones, and other small molecules are functional biomolecules which characterize the state of a biological system. For example, the main component of animal skins is keratin, a family of fibrous structural proteins which are themselves polymers built from amino acids. Amino acids are one of the most important building blocks in nature to construct larger molecules. Peptides and proteins are key biomolecules that are responsible for a wide variety of biological functions such as enzymatic activity, transport of reactants, as well as replication and repair of DNA. Another type of building block is the nucleotides which consist of three components: a purine or pyrimidine base, a pentose sugar, and a phosphate group. These nucleotides form the genetic material of organisms, nucleic acids. Besides polymeric biomolecules, numerous small organic molecules, for example, lipids, vitamins, and carbohydrates also exert a significant influence on the maintenance and functions of organisms. Among the various kinds of biomolecules, only the interactions between low-energy ions and DNA as well as proteins and their building blocks (nucleobases, deoxyribose, nucleosides and amino acids) have been studied and those of other types of biomolecules have rarely been investigated. The studies on low-energy ion interactions with biomolecules have evolved along three broad directions, namely ion beam analysis of biomolecules [32,33], ions in environment [34,35] and medicine [36–38], and ions in life origin, astrophysics and astrobiology [39–42].

Ion beams are frequently used in modern analytical techniques to determine elemental compositions, elemental depth profiles, and damage in crystals. Better understanding of the collision dynamics between energetic ion/atom beams with nonvolatile, high molecular weight bio-compounds has advanced analytical techniques such as secondary ion mass spectrometry (SIMS) and fast atom bombardment (FAB) [43,44]. In traditional mass spectrometry, it is relatively difficult to study macromolecules like amino acids, peptides, and nucleotides because the ionization process such as heating and electron impact used to volatilize and ionize the material usually leads to thermal decomposition, but on the other hand, ion or atom bombardment can more effectively produce the desired molecular ions [45–47]. The key research topics include the fundamental processes of ion formation, ion dissociation, mass separation, and detection of macromolecules in order to acquire more accurate structural information and to understand the binding energy relationship in macromolecules [48–50]. There have been several recent breakthroughs pertaining to the use of new imaging mass spectrometric and microscopic approaches to study the spatial distributions of molecules on biological surfaces. As a result, biomolecular mass spectrometric methods are being developed allowing more accurate spatial mapping of biomolecules including proteins, peptides and lipids at subcellular resolution. For example, focused ion beam (FIB) machines with probe beam sizes of $\sim$10 nm can be used both as an analytical tool and *in situ* cutting of tissues and cells [51]. Commercial instruments such as the NanoSIMS 50 offer high mass and lateral resolution as well as improved sensitivity, which have been very difficult for older instrumentation [52,53]. MALDI-TOF (matrix-assisted laser desorption/ionization time-of-flight) MS can detect proteins and peptides with high sensitivity and selectivity over a wide mass range (10^3 to 10^5 Da) in complex mixtures. Recently, microprobe imaging MALDI MS of mammalian tissues has produced specific protein and peptide maps at 30–100 μm resolution. In order to improve the spatial resolution to subcellular length scales (<1 μm), both better instrumentation and sample preparation protocols have to be developed [54].

The interactions between singly and/or highly charged ions and biomolecules play a crucial role in biological radiation damage processes. Ions with keV or lower energies can be produced in the recoil processes of decaying nuclei which emit protons, α-particles, or γ-rays [5]. When ionizing radiation or particles interact with living cells, a complex cascade of events is initiated which can ultimately lead to cell death or mutation if irreparable DNA damage is induced

[55]. Besides direct disruption of DNA by such primary particles, secondary species such as radicals and low-energy electrons and ions can cause considerable damage as well [56–58]. Similarly, DNA damage at the end of the primary ion track, for example, at macroscopic distances inside the target organism, is also of consequences since the remaining primary ion energy (several 100 eV) at track ends is transferred to a confined region to potentially induce cluster DNA damage [36–38,59–63]. Although the possible biological effects of low-energy particles have been investigated since the 1960s, for example, interactions between 0.1 and 100 keV protons and ribonuclease, bacterial phage, and DNA molecules [64–65], extensive experimental investigations on low-energy ion induced excitation, ionization, and fragmentation of DNA constituent molecules and small DNA model systems have only been performed very recently.

Similarly, in outer space beyond the magnetic shield of the earth, high-energy protons from the sun and heavier particles from interstellar sources may possess energies large enough to penetrate the walls of space stations but low enough to stop inside on-board equipment and the astronauts' bodies, thereby posing genetic and carcinogenic risks to astronauts [66,67]. For example, during a three years mission to Mars, it is calculated that there are 400 proton and 40 He ion traversals through the nucleus of each cell of the human body [68]. There are chances for cancer even if only one mutated cell survives the ion traversal. As high-energy particles traverse matter such as spacecraft walls or tissues, atomic and nuclear collision processes alter the composition of the primary particles via both energy loss and nuclear particle production. Secondary nuclear particles produced by high-energy particles include evaporation and cascade particles such as neutrons, hydrogen and helium ions, as well as low-energy heavy ions [69]. In some situations, even a single hit by an α-particle can result in cell death and mutagenesis, as proven by experiments performed on a single-particle irradiation system [34]. There is also recent evidence concerning ''bystander'' responses involving damage to nearby cells that are not results of direct hits [35,70,71]. Therefore, the action of cosmic ray particles, especially those passing through multi layers of objects and thus with kinetic energies in the medium to low range, should be understood more accurately in order to guarantee safer space explorations.

In outer space, icy surfaces are present both in the interstellar medium as mantles on interstellar dusts and in/on many atmosphere-less objects in the solar system [72]. Energetic keV to MeV particles such as low-energy cosmic rays, magnetospheric ions, solar flares, and solar wind particles impinge on them producing some relevant and potentially observable effects such as sputtering as well as chemical and structural modification [73–75]. Reactive ions, for example, H, C, N, O, and S, can induce all of the effects of other ions including the synthesis of molecular species originally not present in the targets. Laboratory simulated keV ion bombardment experiments of water ice support the possibility of a radiation-driven ecosystem on Europa based on the availability of organic molecules and oxidants such as hydrogen peroxide [76,77] on that moon. As a matter of fact, in addition to the on-site observations made by space probes, ion irradiation experiments conducted in the laboratory constitute a very important vehicle to fathom and explain the interactions and reaction processes occurring in the outer solar system and interstellar space [78].

1.4. Discovery of biological effects in organisms induced by keV ions [1,79–82]

Living organisms are generally vulnerable to vacuum stress and therefore not suitable for low-energy ion interaction experiments that are typically conducted in a high-vacuum ambient. In addition, because of the assumed short penetration depth of low-energy ions in water-abundant substances, the macroscopic biological effects caused by low-energy ion interaction have long been neglected. This is also due to the general thinking that the genetic material inside organisms must be directly hit by incoming ions in order to cause any inheritable mutations. Therefore, it is not surprising that past research in this area has been relatively few. For instance, the observed total bio-effects of slow moving ions at the end of the trajectories of primary particles such as high-energy protons and C^{q+} ions used in cancer treatment have only been reported in scattered reports until recently [83–85].

In the mid 1980s, the biological effects of ion implantation were recognized and demonstrated experimentally [80–82]. The ion energies used in these experiments were at least three orders of magnitude lower than the typical energies utilized in conventional heavy ion biology. It was generally assumed that these low-energy ions had a projected range in water that was far too small to reach the inner volume of the samples to induce any appreciable biological effects. In some early work carried out by us, 30 keV nitrogen ions were implanted into rice seeds. When the ion fluence was sufficiently high, yellow stripes were seen on the leaves of rice plants grown from the seeds, similar to the phenomenon found on corn leaves in the Apollo-Soyuz space flight experiments. These traits were subsequently found to be inheritable and transmitted to latter generations.

In order to explore the mutation mechanism in rice seeds induced by ion implantation, a hypothesis which incorporates a combination of energy absorption, mass deposition, and charge transfer of energetic ions in seeds has been proposed [82] and has subsequently spurred research activities in this new direction. In comparison with the established theory of the interactions between energetic ions and metals or semiconductors that are based on an accurate description of the bullet-target system, biological systems are not as clear and straightforward. A biological organism is a complex system composed of solids, fluids, and sometimes gases. Not only is it not as stable as a metal or semiconductor solid, its state is continuously changing. For example, living things grow and develop. Seeds breathe even in its dormancy, albeit lightly. The biological structure is separated spatially into many small rooms (cells), and a cell is further divided into a number of smaller compartments. Temporal and spatial changes in the biological structure greatly complicate studies of the interactions between energetic ions and the living biological targets.

From an atomic collision point of view, energy losses in any targets should be similar. In the case of low-energy ion implantation, an ion transfers some of its energy to a target atom and is scattered. The transferred energy causes the target atom to be displaced. This is generally known as nuclear energy loss. At the same time, the moving ion transfers some of its energy to the electrons of the target atoms causing ionization, excitation or electron capture. This type of energy loss for low-energy ions is relatively small and the ion trajectories are not significantly altered. This is termed electronic energy loss. The complex situation associated with organisms arises from their multiple layers, multiple phases, and multiple channel structure. After an initial collision between the incident ion and a target atom, it is difficult to determine where and with what kind of target atom the next collision will occur. Furthermore, starting from the moment the ions are implanted into organisms to the final state producing biological effects, the time scale may span from 10^{-19} to 10^{9} s. The relevant spatial dimensions range from microbiological damage to macro-property changes. Thus, the establishment of an accurate physical model for such a complex system is very difficult.

Nevertheless, significant progress has been made in the understanding and utilization of the interactions between the implanted ions and living cellular materials in various aspects including small biological molecules, DNA, cells, and tissues of which organisms are composed. Some significant results have been obtained and some ion beam technologies have led to new biotechnologies. Ion beam mutation of crops and microbes, ion beam induced gene transfer, and ion beam induced synthesis of pre-biotic species are examples. Recent advances in mechanistic investigations and applications oriented research have opened new areas in life sciences, including the role of low-energy ions in the chemical origin of life, the formation of interplanetary molecules, risk evaluation of low-energy particle irradiation in the environment, and the application of ion beam to genetic modification.

2. Ion collision with biomolecules

Energetic ion bombardment of materials (organic or inorganic) or organisms (microorganisms, plant or animal cells/tissues) allows researchers to find out the structure and other characteristics of the targets or induces new functions or properties in them. The ionization and disintegration phenomena induced by the impact of energetic ions on biological samples have been utilized in ion beam analysis techniques for a long time and as aforementioned, a variety of imaging and mass spectrometric techniques have been developed. These techniques have found increasing use in molecular analyses of surfaces prepared from carefully prepared cells and tissue sections or of evaporated or atomized bio-molecules and atoms. By static and dynamic secondary ion mass spectrometry (SIMS) [86], it is possible to determine directly the spatial distributions of both endogenous and exogenous species within macromolecules (e.g. chromosomes) as well as plant and animal cells or tissues at a lateral resolution of less than 50 nm using Cs^{+} primary ions [87–89]. As a complement to traditional enzymatic sequencing techniques, mass spectrometry (MS) has been employed to characterize nucleotide constituents and determine the sequence of oligo-(deoxy)-nucleotides and polypeptides for nearly 40 years [90]. MS techniques have also played crucial roles in the identification of modified nucleobases in such as ribosomal and transfer ribonucleic acids as well as oligo-(deoxy)-nucleotides synthesized for special biomedical/pharmacological applications [91,92]. Matrix-assisted laser desorption/ionization mass spectrometry (MALDI-MS) and electrospray (tandem) ionization mass spectrometry (ESI-MS) based on low-energy collision induced dissociation can generate intact molecular ions from polymers of nucleotides and amino acids. These techniques are now widely used in peptide tags, posttranslational modification, mixed-sequence DNA/RNA oligonucleotides and lipopeptides [93]. The ion impact induced biomolecular dissociation/fragmentation and recombination of fragments containing both the incident ions and target atoms/groups are expected to result in certain effects in the cellular material and their surroundings, for instance, destruction of plasma membranes and gene

mutation, if such reactions occur inside bulk organisms. However, researchers have mainly focused on the analytical processes and have essentially ignored the intrinsic effects on the biological specimens.

From the physical–chemical point of view, there are three main processes in ion beam interactions with biomolecules. The first one is the reaction induced by elastic nuclear collision or momentum transfer during deceleration of the incident ions giving products that do not contain the incoming ions (momentum transfer effects). The second one is the reaction induced by the transfer of energy when the ions are electronically stopped yielding products which again do not contain the incident ions. This is an important area in radiation physics and chemistry research. The third one is the reaction between the incoming ions and target molecules and/or fragments giving products which incorporate the primary ions, the so called mass deposition effects. When the penetration depth of the incident (primary) ions is smaller than the thickness of the target, these ions are stopped and implanted inside the sample. Each incoming ion that typically has energies between 10 and 100 keV breaks 10^3 to 10^4 bonds (few eV per bond) and a large number of new molecules can be formed per single incident ion by recombination [73]. When the primary ions slow down to the energy range in which chemical reactions can occur, new chemical species that contain the incident ions can also be formed with a maximum yield of one molecule per incoming ion.

From the biological standpoint, biomolecular damage such as disintegration and fragmentation of amino acids and nucleobases, and raidolysis of water molecules in the surrounding regime of structural molecules give rise to DNA damage [94–96], chromosome aberration [81], and other biological effects. It is generally accepted that molecular damage induced by high-energy ionizing radiation in the range of millions of electron volts (eV) is actually the combined result of a multitude of low-energy (a few to several hundreds eV) events [97]. It has also been reported that one-third of the damage in the genome of a living cell is directly caused by ionizing radiation and two-thirds of the damage are caused indirectly [55]. The direct effects include direct energy deposition and ionizing reactions in the biomolecules, whereas indirect damage is caused by radiation induced reactive species (mainly radicals) in the medium (mainly water) surrounding the biomolecules [98]. In the following sections, radiolysis of water molecules by ion collision is described, followed by a discussion on the damage of DNA and protein building blocks by ions in the hyperthermal to keV energy range.

2.1. Radiolysis of water by low-energy ion collision

2.1.1. Fragmentation and dissociation of gaseous water by low-energy particles

Radiolysis of water molecules, the natural environment of DNA, by electrons, protons, or heavy particles is an important phenomenon since the first stage of formation of our planetary system [99]. For example, energetic S and O particles from the Jovian magnetosphere impinging onto the icy surface of Europa leads to water radiolysis which dominates the surface chemistry of that moon [77,100,101]. In tumor therapy, high energy C ions are used in virtue of their particular volume-selective dose distributions [102]. A large fraction of the energy deposited in tissues by the incident particles is absorbed by water molecules, leading to the formation of radicals and ion fragments [103]. It has been demonstrated that OH radicals can be formed at 77 K in the hydration shell of the DNA composed of more than 14 molecules of H_2O per nucleotide [104]. Radiation damage in biomolecules is the result of not only a single interaction of the primary ionization projectile with the molecules involved, but also the chain reactions that may encompass radicals produced by destruction of the water molecules surrounding the DNA [105].

In their pioneering studies, Curie and Debierne observed that radioactive radium decomposed water into gases containing hydrogen and oxygen [106,107]. In the first half of the 20th century, α-particle emitters such as polonium and curium were used for ion beam irradiation and high-frequency discharge in hydrogen gas was adopted to produce thermal hydrogen atoms [64]. Nowadays, in addition to traditional sources, various kinds of commercial ion accelerators such as cyclotrons or synchrotrons for high-energy ion beams, Van de Graff or single-ended accelerators for medium-energy beams and ion implanters for low-energy beams have been developed to spur ion beam research. Water radiolysis by high-energy particles has thus received a lot of interest both experimentally [108–112] and theoretically [112–117]. A variety of reactive species can be formed along the trajectory of the charged particles [115,118] and their distributions are not homogeneous. The unpaired electrons in free radicals are highly reactive in chemical reactions. The most ubiquitous and biologically important species formed in aqueous solutions by ionizing radiation are $H^{\bullet}$, $OH^{\bullet}$, and e_{aq}^{-}.

Improved instruments equipped with high mass-, time-, and position-sensitive multi-channel detectors have allowed scientists to analyze in details proton and heavy ion impact ionization of water vapor and to measure the cross

sections of partially or totally fragmented channels [119]. Moreover, using a time-of-flight mass spectrometer in an ion beam/multiparticle apparatus, both the state of the incoming ions after collision, for example, the final kinetic energy release (KER) and charge state, and the target molecule can be measured at the same time. Alvarado et al. [120] studied the dissociation of water molecules upon 4–24 keV H^+, He^+, and He^{2+} impact, with particular focus on the kinetic energy release (KER) and identification of the underlying processes at different ion kinetic energies. In addition to an extraordinarily large relative dissociation yields by the He^+ projectile compared to those of the other two incident ions, H^+ fragments with 14.5 eV KER formed by both singly charged projectiles H^+ and He^+ are emitted after collision arising from the two-step dissociation sequence $H_2O^{2+} \rightarrow OH^{2+} + H \rightarrow O^+ + H^+ + H$. Similarly, using fragment ion spectrometry (FIS), Seredyuk et al. measured the energy spectra of ions from the interaction of 4 keV He^{2+} with H_2O molecules and observed dominant peaks in the energy range from 0 to about 30 eV with H^+ at around 15 eV [121] (Fig. 1). Investigation on water molecule fragmentation following interactions with slow, multiply charged neon ions revealed emitted protons with kinetic energies up to 70 eV in the case of Ne^{9+} impact. The total yield of the fragment ions was found to increase strongly with higher initial ion charge states [105]. These results are of particular interest in the context of biological radiation damage, since these protons with energies in the hyperthermal range (0–100 eV) have the potential to induce further damage in DNA molecules. It will be further discussed in latter sections.

Utilizing time-of-flight technologies, the different types of reactions involved in the collision process, for example, electron capture/loss mechanism not present in electron and photon impact, can be measured experimentally [99]. In the ion collision study of water vapor by 2–150 keV protons, H_2O^+, OH^+, O^+, O_2^+, H^+, and negative ions are observed together with H^+ when the projectile remains a proton, neutral H after single electron capture, or H^- if double electron capture occurs during the collision event [122]. A complete set of total and partial cross sections for each product ions such as H_2O^+ and H^+ have been determined. It has been observed that for electron capture, the maximum absolute capture cross section occurs at around 25 keV and drops by almost two orders of magnitude when the primary proton energy goes up to 150 keV. In contrary, the cross section of direct ionization displays an opposite trend. Therefore, it has been deduced that for 20–150 keV proton impact, the electron transfer mechanism contributes with the highest probability to the dissociation of water molecules. Luna et al. measured the absolute cross sections of positive fragments following electron capture, ionization, and electronic loss collisions of C^{3+} and O^{5+} with water molecules with energies corresponding to the range of maximum Bragg peaks and compared the results with collision of water molecules by protons, electrons, and photons. While the main product after proton collision was H_2O^+, the main product in the C^{3+} case was H^+ (Fig. 2) [99]. The large H^+ production compared to OH^+ and O^+ in the C^{3+} case also indicates that a substantial amount of neutral OH is produced via the reaction $H_2O^+ \rightarrow H^+ + OH$. Further analyses

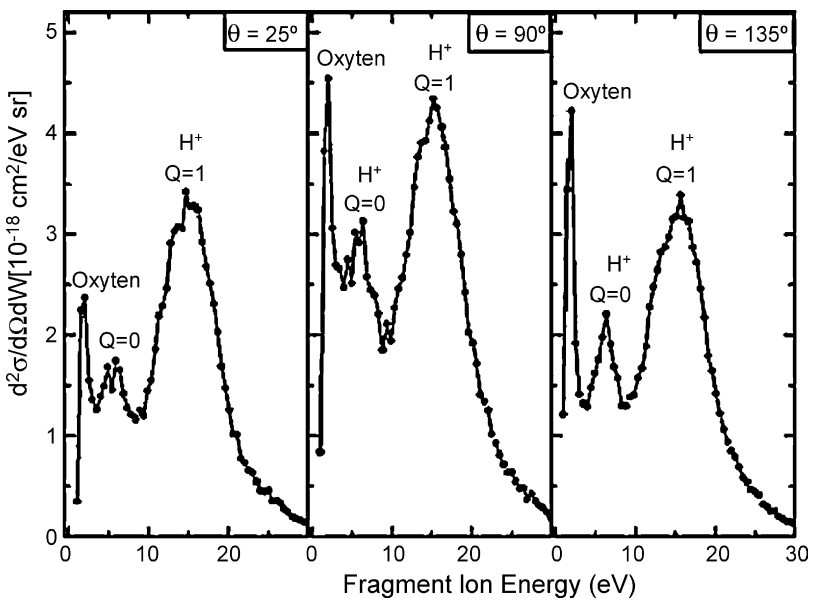

Fig. 1. Energy spectra of fragment ions from the interaction of 4 keV He^{2+} ions with H_2O molecules. The observation angles Q are 25°, 90°, and 135°. Reprinted with permission from [121]. Copyright 2005 by the American Physical Society.

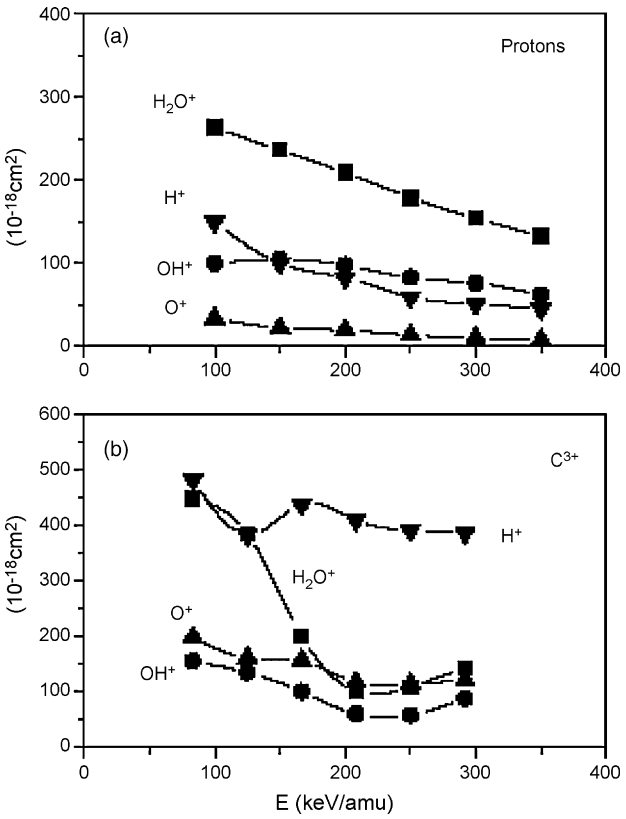

Fig. 2. Total cross sections for water fragmentation by (a) H^+ and (b) C^{3+}. The cross sections by protons follow the sequence $(H_2O^+) > (OH^+) > (O^+)$ associated with a sequential breakup process, while the C^{3+} cross sections show a very different pattern. For C^{3+}, water is more likely to fragment completely, releasing O^+ ions, rather than to stabilize as OH^+. Reprinted with permission from [99]. Copyright 2005 by the American Physical Society.

point out that the general assumption that initial decomposition of water is independent of the particle type in water radiolysis may apply to photons, electrons, and protons, but not heavy ions. Another interesting phenomenon of water radiolysis by C^{3+} is the substantial increase in O^{q+} production. It has been suggested that the large LET (linear energy transfer, the energy *dE* which a charged particle loses at a distance *dl* in the target material) of C ions is significantly consumed in blowing up water molecules, releasing a large number of energetic H^+ and O^+ fragments in comparison to proton, electron, and photon irradiation. These excess energetic electrons together with the formation of a large number of reactive water radicals can explain the different bio-responses observed in C-ion and proton tumor therapies [99,123].

2.1.2. Destruction and sputtering of water ice by keV ion beam

In the previous sections, ion collisions with gaseous water molecules are reviewed with emphasis on the properties of the emitted H^+ and OH^+ as well as the physical processes that result in the dissociation of water molecules. However, in many situations involving ion irradiation of water, water is present as solid ice with thicknesses much larger than the penetration depths of keV and even MeV ions. Therefore, the effects of ion irradiation on water ice including destruction and sputtering of water molecules and chemical reactions induced by ion irradiation are of scientific interest and have been extensively studied in the past decades. There are three general effects pertaining to ion irradiation of ices: (1) sputtering by incident ions, (2) physical and chemical modification of the target and formation of new species, and (3) deposition of ions inside the target and formation of new molecules containing the incoming ions.

The basic apparatus to study ion implantation into water ice comprises an ion source, a low-temperature vacuum system, and analytical and diagnostic tools such as transmission infrared (IR) spectroscopy (Fig. 3) [124–126]. Frozen water films are typically vapor deposited onto an IR-transparent silicon substrate in contact with a cold finger with

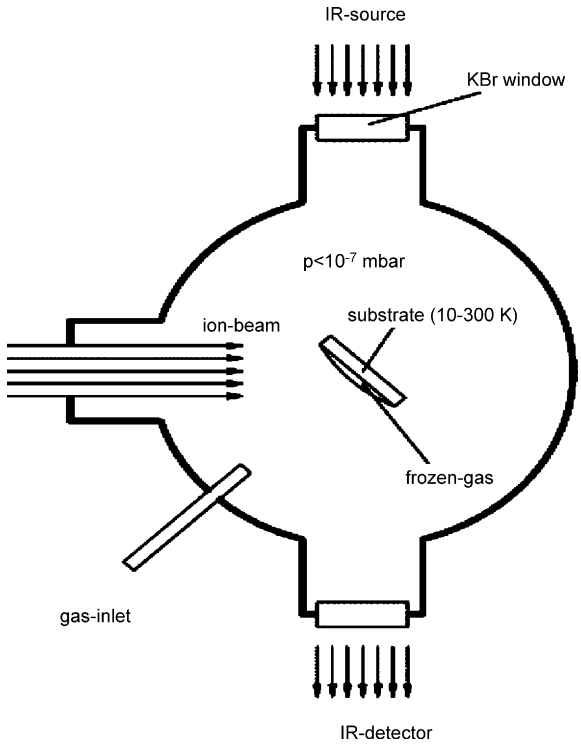

Fig. 3. Schematic diagram of the experimental setup for ion irradiation of ices. Reprinted with permission from [125]. Copyright 2003 by Elsevier.

temperature adjustable from 10 to 300 K. The vacuum chamber is connected to an ion implanter in which ions with terminal voltage of up to 30 keV can be obtained. The beam currents are usually kept below a few $\mu A/cm^2$ to avoid excessive heating and damage to the target. The sample surface is usually positioned at 45° with respect to both the infrared beam and incident ion beam, so that on-line analyses can be performed before, during, and after ion implantation.

One of the effects of ion irradiation is the destruction of molecules in the target. Chemical bonds can be broken and molecules are disintegrated into fragments that may escape from the surface or recombine to form new species. Sputtering is also a common phenomenon that leads to mass loss or redistribution of molecules on the surface. Sputtering is characterized by the sputtering yield, Y_S, which is the number of molecules or atoms ejected per incident ion and has the unit of molecules/ion. A common approach to quantify sputtering yields is by mass loss measurement using a sensitive microbalance. The mass loss is converted to the number of water molecules and divided by the number of incident particles to derive the sputtering yield. The degree of target destruction due to ion irradiation can be described by the destruction yield, Y_D, which can be determined by the column density (molecules/cm^2) of the target species and irradiation fluence (ions/cm^2). The column density can be measured by the integrated area (in cm^{-1}) and integrated absorbance determined by IR spectroscopy [73]. Both sputtering (original molecules, atoms and dissociated fragments, and/or newly-generated species ejected from the target) and species transformation via chemical reactions contribute to the observed loss of the original species. Therefore, the destruction yield is usually higher than the sputtering yield, especially in the case of reactive low-energy, heavy ion implantation into thick samples where the probability of chemical reactions is higher.

Since Brown et al. [127] discovered the high electronic sputtering yields of water ice and discussed its implications in astronomy, sputtering of water ice has been studied for more than two decades in many simulated ion irradiation experiments. Brown's work shows that mega-electron-volt protons sputter the water ice surface much more efficiently than what has been anticipated based on conventional elastic and knock-on mechanisms developed for metals and semiconductors. Sputtering of ice has recently been reviewed by Baragiola et al. [128]. The primary species sputtered from water ice are H_2 and O_2 in addition to H_2O molecules with near intrinsic thermal energies [129]. The total sputtering yield is essentially constant below 60–100 K and increases rapidly at higher temperatures. It has also been

found that OH radicals can be stored in crystalline ice up to temperatures of about 130 K [130]. Hydrogen atoms can diffuse and recombine either with OH forming H_2O or with another H forming H_2, which are then emitted from the surface. With increasing irradiation fluences, the amount of OH radicals increases to a limit imposed by recombination with H and by reactions with other OH yielding H_2O_2 [131].

The destruction losses [73,132] and sputtering [128,133] of water ice by 30 keV C^+, N^+, O^+, and Ar^+ irradiation at 16 and 77 K have been determined experimentally and the data are displayed in Table 1. With the exception of O^+, the amounts of destroyed (i.e. sputtered or chemically modified) water molecules for a fluence of 6×10^{15} ions/cm^2 are similar at these two temperatures. For O^+, more water is destroyed at 77 K than 16 K (122 molecules/ion versus 14.1 molecules/ion). The sputtering yields in the range 20–77 K are almost constant. Comparing the values of destruction and sputtering yields, the Y_D values for N^+, $^{12}C^+$ $^{13}C^+$, and Ar^+ are no more than a factor of two higher than their sputtering yields, whereas the Y_D value for O^+ at 77K (122 ± 5 molecules/ion) is three times the sputtering yield (40 molecules/ion). This means that at 77 K, more water molecules are destroyed by O^+ because the produced fragments may be transformed more easily into other species in lieu of being ejected directly from the substrate [129]. It has also been observed that heavier Ar^+ introduces more damage and reactions, as manifested by its higher Y_D and Y_S compared to C^+ and N^+ (Table 1).

2.1.3. *Formation of H_2O_2 and CO_2 in pure water ice during ion implantation*

By monitoring the infrared spectra of water ice implanted with 30 keV $^{13}C^+$ at 16 K with time, losses of H_2O as well as formation of H_2O_2, $^{13}CO_2$, and ^{13}CO can be determined for different fluences, as shown in Fig. 4 [73]. The diminishing water ice band intensity is due to two different processes, namely sputtering of water molecules and reactions that produce new species as described in the previous section. The second region refers to the hydrogen peroxide molecule spectrum and its intensity increases with ion fluences. The results show unequivocally that even in the simplest molecular substrate, the impinging ions disrupt the original molecular bonds and molecular fragments recombine forming other molecules that are not originally present in the substrate. The third region corresponds to $^{13}CO_2$ that is not in the substrate originally and is produced by implantation of 30 keV ^{13}C. It is again proof that a chemical reaction that involves the incident ions and substrate species has occurred. The production yields of $^{13}CO_2$ at both 16 and 77 K show no significant differences and the average value is $0.42–0.47 \pm 0.03$ molecules/incident C^+ ion. This is different from an earlier report on the irradiation of frozen water ice with 10 keV C^+ ions [134]. According to the intensities and integrated absorbances of both $^{13}CO_2$ and ^{13}CO, it can be inferred that ^{13}CO may not be produced directly by ion implantation of $^{13}C^+$ but from dissociation of $^{13}CO_2$ instead [73].

It has been observed that the quantity of H_2O_2 produced for N^+ and Ar^+ irradiation at 16 and 77 K does not vary much with temperature. However, during C^+, H^+ and O^+ bombardment, more H_2O_2 is produced at 77 than at 16 K. The changes are thought to be related to the implantation parameters such as the ion penetration range and diffusion rate of the radical species in the substrate. Based on the penetration depths calculated by SRIM, the amount of H_2O_2 generated from the sample can be used to study the relationship between H_2O_2 formation and ion fluences for each projectile ion. With the exception of H^+, the amounts of H_2O_2 produced by the other four kinds of incident ions increase quickly at low ion fluences and reach saturation when the fluence exceeds $\sim 7 \times 10^{14}$ ions/cm^2 as

Table 1
Destruction and sputtering yields of water ice upon irradiation with various ions at 16 and 77 K [73,128,132,133]

Ion species	Irradiation temperature (K)	Water ice destruction yield (molecules/ion)	Water ice sputtering yield (molecules/ion)
N^+, 15 keV	16	13.1 ± 2.5	
N^+, 30 keV	16	10.4 ± 1.3	8–10
N^+, 30 keV	77	10.6 ± 2.3	
C^+, 30 keV	16	8.5 ± 1.4	
C^+, 30 keV	77	9 ± 3	
$^{13}C^+$, 30 keV	16	13.1 ± 0.4	
$^{13}C^+$, 30 keV	77	13.7 ± 1.1	
O^+, 30 keV	16	14.1 ± 1.0	40
O^+, 30 keV	77	122 ± 5	
Ar^+, 30 keV	16	43.6 ± 2.3	25
Ar^+, 30 keV	77	36.8 ± 1.9	

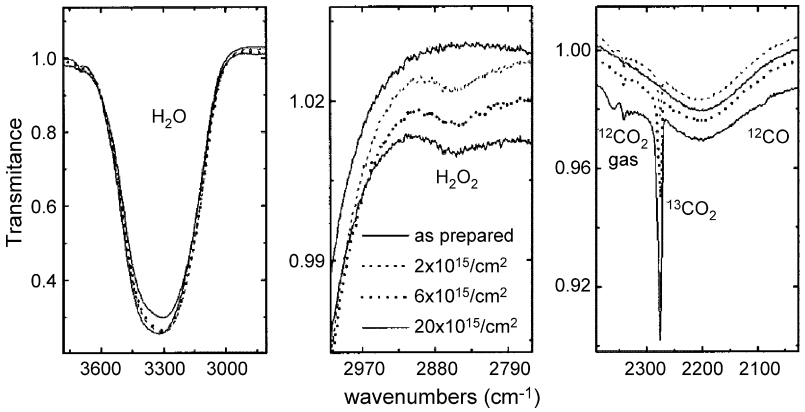

Fig. 4. IR spectra (in three spectral regions) of H_2O (16 K) ice as prepared and after implantation of 30-keV $^{13}C^+$ ions with different fluences (ions/cm^2). The three spectral regions illustrate the destruction of H_2O and formation of H_2O_2, $^{13}CO_2$, and ^{13}CO. Reprinted with permission from [73]. Copyright 2003 by Elsevier.

demonstrated in Fig. 5 [132]. This suggests a dynamic equilibrium between the formation of new H_2O_2 and destruction of existing H_2O_2 by the subsequent incident ions. Loeffler et al. irradiated water ice films with 50–100 keV Ar^+ and 100 keV H^+ at 20–120 K and monitored the synthesis and volume evolution with increasing temperature of H_2O_2 by means of infrared spectroscopy. The amount of hydrogen peroxide produced remains stable while the ice film is warmed after irradiation. The column density of the formed H_2O_2 is constant until the ice film begins to desorb, but the concentration of H_2O_2 increases with time during desorption because water sublimes at a faster rate [135].

Hydrogen peroxide H_2O_2 as well as the hydroxyl $OH^\bullet$ and superoxide $O_2^\bullet$ radicals are highly reactive and strong oxidizing species. They can be generated in biological cells by water radiolysis and many enzymatic and non-enzymatic reactions of dioxygen. Owing to the fast diffusion rate and long lifetime, H_2O_2 has been investigated extensively. For example, it is an important molecule contributing to oxidative damage initiated by a variety of exogenous agents even in common beverages such as coffee and tea [136–137]. Cellular DNA damage by H_2O_2 arises from the highly reactive hydroxyl radicals ($OH^\bullet$) generated in Fenton-like reactions between H_2O_2 and metal ions such as Fe^{2+} [138]. Formation of H_2O_2 has been observed in experiments involving non-ionizing and ionizing radiations including ultraviolet [139], electrons [140], and α-particles [141]. Experimental evidence [140,142–144] described here suggests that low-energy keV ion bombardment can result in the formation of abundant H_2O_2 even in the simplest biologically relevant compound, water, and hence mutagenesity can be initiated by further reactions of radicals with DNA molecules.

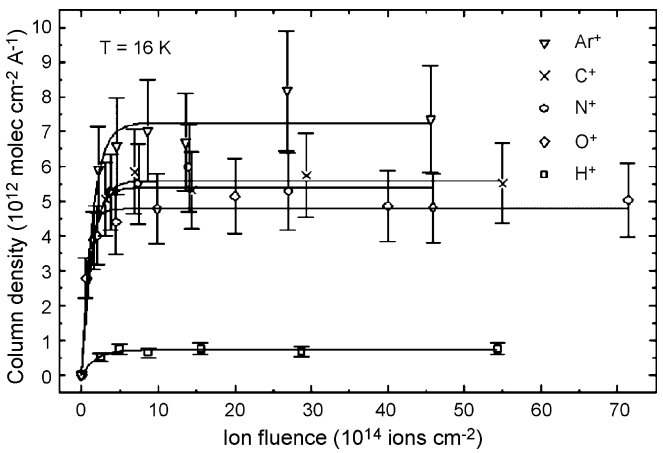

Fig. 5. H_2O_2 column density normalized to the ion range ($\times 10^{12}$ molecules/cm^2 A) as a function of ion fluence at 16 K. Curves represent an exponential best fit. Reprinted with permission from [132]. Copyright 2004 by Elsevier.

In addition to the above examples, formation of CO_2 has been observed under other conditions, including irradiation of H_2O ice on top of carbonaceous materials [145] or amorphous carbon films [146] with 30 keV He^+, 200 keV H^+ and Ar^+, irradiation of CH_3OH with 3–30 keV He^+[147], and 60 keV Ar^{2+} into CH_4:H_2O and CH_4:H_2O:N_2 [125,148,149], but not in the cases of N^+ into pure water and O^+ into CH_4. Since irradiation of water ice results in dissociation of water molecules into H and OH and other products (H_2, O, O_2, H_2O, HO_2, and H_2O_2) [128,133], the processes responsible for the formation of CO_2 have two mechanisms. When there is CO in the substrate, CO_2 can be easily formed by the reaction OH + CO → H + CO_2 [150], or when carbon is implanted into pure water, carbon dioxide can be formed either by direct combination of C with O_2 or via the reaction HO_2 + C → H + CO_2. However, since there is no evidence of CO_2 formation after implantation of O^+ into frozen CH_4, it can be deduced that the presence of C and O is necessary but not sufficient for the production of CO_2 under these conditions.

In addition to water that accounts for 70–95% of cellular mass, carbon-based compounds are vital to life and they form the backbones of cellular structure and function units. In 1953, Stanley Miller set up a facility simulating the chemical conditions on primitive Earth and demonstrated the spontaneous synthesis of organic compounds. Such spontaneous synthesis of organic compounds has been thought to be an early stage in the origin of life. CO_2 is the source of carbon for all organic molecules found in organisms on Earth. It is usually fixed inside organic molecules by the process of photosynthesis. The first living cells on the Earth might function and grow using carbon from carbon monoxide, methane and/or carbon dioxide dissolved in seawater.

2.2. Formation of organic molecules in simple targets by ion implantation

Nitrogen is the most abundant element in the Earth's atmosphere and also a constituent in all amino acids in living matter. Molecular nitrogen is a major constituent of Titan's thick atmosphere and has been detected in interstellar space by the Far Ultraviolet Spectroscopic Explorer [151]. The formation of nitrogen containing compounds after ion implantation of ice mixtures with or without indigenous nitrogen is a topic of extensive research, and the results are quite complex. Consequently, it is difficult to postulate a set of universal rules governing the reactions between the implanted ions and substrate atoms. In pure water ice implanted with 15 keV N^+ at 16 and 77 K, no N_2O, NO, and NO_2 have been detected by IR spectroscopy [73]. However, if N_2 is mixed with H_2O, all three nitrogen oxide species can be produced by 60 keV Ar^{2+} implantation [125]. R (refractory)-OCN and HCN can be formed by implanting non-reactive (noble gases) ions into mixtures containing C, N, and O atoms (e.g., N_2:H_2O:CH_4). Similar products are generated when mixtures containing only C and O atoms (H_2O:CH_4) are irradiated with N ions, implying that molecular species that contain the implanted ions can be produced during energetic ion bombardment [152]. For instance, the CN– functional group is formed by N^+ implantation into mixtures of H_2O:CH_4 (1:1) or H_2O:NH_3:CH_4 (1:1:1), whereas hydrogen cyanide (HCN) and diazomethane (CH_2N_2) are produced by 60 keV Ar^{2+} implantation of CH_4:N_2 mixture ice. HCN (hydrogen cyanide), HNC (hydrogen isocyanide), diazomethane (CH_2N_2), and several radicals are formed in the solid phase of proton-irradiated N_2-rich ices containing CH_4 and CO [150]. NH_3 has been identified in irradiated N_2:CH_4 and N_2:CH_4:CO [153] and X–OCH has been detected after nitrogen implantation into H_2O:CH_4 mixture ice, but not after implantation of oxygen into frozen mixtures of CH_4:N_2. In the ternary mixture of H_2O:CH_4:N_2, 60 keV Ar^{2+} implantation results in the formation CO_2, $^{13}CO_2$, HNCO, N_2O, CO, HCN, CH_2N_2 and even X–C≡N [154]. Based on these results, it can be inferred that ion implantation of simple molecules can result in progressive synthesis reactions in the original ices. The generation of CN– by N^+ implantation into H_2O:CH_4 means that nitrogen containing compounds can be produced by reactions with nitrogen not indigenous to the original substrate, for example, energetic N^+ ions from cosmic rays and in the inner magnetosphere of Saturn. Some of these cyano-containing products such as HCN, HNC, HNCO, NH_3, NH_4OCN, and NH_4CN are involved in the syntheses of biomolecules such as amino acids and polypeptides [153]. These molecules may have been produced by comets striking early Earth and contributed to the development of more complex biogenetic compounds on our planet.

In addition to the formation of nitrogen-containing compounds in mixtures of low-temperature ices as described above, the synthesis of nitrogenous compounds in ion irradiated, dry solid organic sodium salts has been reported as well. In these experiments, samples of solid organic sodium salts, sodium formate, sodium acetate, and sodium benzoate were irradiated by 10–30 keV N^+, H^+, and Ar^+ ions [155]. After irradiation, EPR (electron paramagnetic resonance), FTIR (Fourier transform infrared spectroscopy), UV–vis spectrophotometry, hydroxylamic acid reaction, and ninhydrin test were adopted to analyze the damage of the irradiated samples and existence of new species. In

sodium formate implanted with 20 keV, 1.5×10^{16} ions/cm^2 N^+, H^+ and Ar^+, EPR conducted 15 h after irradiation showed that the COO^- radical ion existed in all the irradiated samples. Under the same irradiation conditions, Ar^+ implantation resulted in more COO^- radicals than the other two implant ions. It was attributed to the higher ionization density of Ar^+ than H^+ and N^+, so that Ar^+ could cause more damage to the target molecules. IR spectra showed that no matter what kind of ions were used, new products including $–CH_2–$ and $–CH_3–$ groups could be produced in the implanted sodium formate. The unpaired electrons of a free radical can pair up with the unpaired electrons of another free radical and thus a free radical–free radical combination reaction occurs. This reaction has very low activation energy, almost zero, and thus the reaction can easily take place. Sometimes this kind of reaction produces a new free radical, and this new free radical can continue to react with the original reactants leading to chain reactions. Due to the high activity of free radicals, they can easily take part in addition, hydrogen-extraction and electron-transfer reactions with biological target molecules, resulting in target molecule damage or formation of new molecules.

In addition to the COO^- radical that has a long life time, $–CH_2–$ and $–CH_3–$ groups as well as amino group ($–NH_2$) have been observed in ion irradiated organic molecular substrates with or without elemental nitrogen. The amino group formed by ion implantation has been qualitatively determined by the ninhydrin reaction and quantitatively measured by UV–vis spectrophotometry. The amino group has been detected in Ar^+ and N^+ irradiated pyrimidine uracil which contains nitrogen but not the amino group [156]. At the same energy and fluence, the amine content after Ar^+ implantation is found to be more than that using N^+ implantation. In nuclear collision, the interactions between the colliding particles depend upon the mass number of the particles. Because argon is heavier than nitrogen, argon ions displace more target atoms via recoil and cascade collisions. Consequently, more rearrangement and recombination occur favoring the formation of more amino groups. In another experiment, three kinds of solid organic sodium salts, sodium acetate, sodium formate, and sodium benzoate prepared as a dry, thin layer on glass substrate are subjected to N^+ implantation in vacuum. Under the same irradiation conditions and when the fluence is below 5×10^{16} ions/cm^2, the amounts of the amino group produced in sodium acetate and sodium formate are much higher than that in sodium benzoate (Fig. 6) [157]. With changing fluences, the production of $–NH_2$ increases up to a fluence of 5×10^{16} ions/cm^2 and then decreases when the fluences are higher. However, at the same fluence of 5×10^{16} ions/cm^2, production of the $–NH_2$ group decreases when the ion energy increases from 15 to 25 keV. That is, low energy N^+ ions produce more amino groups. The formation mechanism of $–NH_2$ is postulated on the basis of the quantum structural characteristics of the three sodium carbroxylics in which the reaction between the incoming N^+ ions and irradiation-induced unstable or open-ring target molecules is a necessary step. Fig. 7 illustrates the postulated reaction process with respect to sodium acetate. In the beginning, ion implantation displaces a hydrogen atom from a carbon site to form hydrogen radical, and then the implanted nitrogen binds to this site. Afterwards, two hydrogen radicals bond to the nitrogen to form an amine [158]. The cyano group (–CN, C≡N) is generated in the N^+ implanted sodium acetate and sodium benzoate as well, as revealed by FTIR and hydroxylamic acid test. Since sodium carboxylate does not containing N, the produced amino and cyano groups must result from the reaction between the implanted N^+ ions and active molecular fragments/groups in the substrate. The process is termed mass deposition.

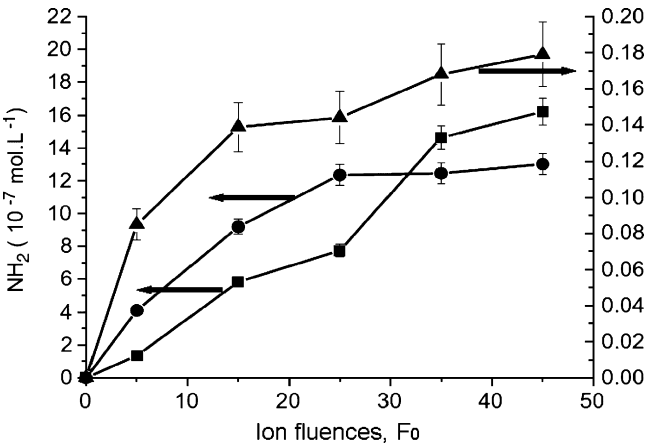

Fig. 6. Fluence-responses of the yield of NH_2-group in the N^+ beam irradiated sodium formate (circle, ●), sodium acetate (square, ■) and sodium benzoate (triangle, ▲) samples ($F_0 = 10^{15}$ ions/cm^2) [157].

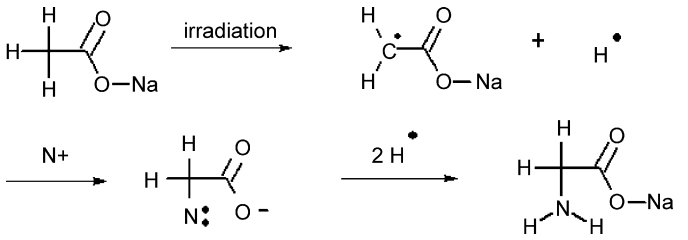

Fig. 7. Postulated chemical reaction for the formation of amino group in sodium acetate induced by keV ion implantation [158].

2.3. Radiological damage of amino acids by low-energy particles

Proteins are involved directly or as DNA binding motifs in various cellular activities such as DNA structuring and packaging, regulation of gene expression, and enzymatic catalysis. Damage of proteins may be fatal to organisms. For example, it has been observed that in a *lac* repressor experimental system in *Escherichia coli*, γ-ray and argon ion irradiation cleave the peptide chain of the *lac* repressor protein and the protein loses its *lac* operator-binding activity, and hence the protein-DNA complex is disrupted [159,160].

Ion irradiation of amino acids causes destruction of amino acid molecules and generation of many volatile products and stable free radicals. The integrated effects can be roughly quantified by the sputtering yield. A high yield of up to 10^3 molecules/ion of H_2, NH_3, CO_2 and hydrocarbon dimmers has been detected during 200 keV helium and argon beam bombardment of alanine (Ala) and glycine (Gly) [161–163]. Huang et al have studied the mass spectra of sputtered products from a thin layer of glycine during 8 keV Ar atom bombardment and peaks in the range of 2–500 amu are detected as shown in Fig. 8. The molecular ion or quasi-molecular ion is not the main peak in the spectrum, but many different ions or radical ions are produced instead during bombardment of glycine. The peak at mass 30 is the most intense and it may be CH_2NH_2 whereas the peak at mass 45 may be COOH. Species with a mass-to-charge ratio higher than 75 are detected implying that molecular fragments as well as molecular clusters that may contain several glycine molecules are sputtered [164]. By using IR, Raman, and XPS (X-ray photoelectron spectroscopy), Compagnini et al. studied the effects of low fluence 250 keV He^+ irradiation on tripeptide glutathione (GSH, γ-L-glutamil-L-cysteinyl-glicine) thin films in their investigation of the protective roles in cells against ionizing radiation. It was observed that the $GS^\bullet$ radical was formed and survived for a long time in the solid state. The chemical yield of the reaction GSH → $GS^\bullet$ was estimated to be about 1000 (reactions) per impinging ion [165]. Normally, mass loss measurement is used to derive the sputtering yield when further details of the mass loss mechanism are not known. For 30 keV N^+ irradiation of the bio-equivalent material, lactamine ($C_3H_7O_2N$), the mass loss is dependent on the ion fluence, and this is in agreement with the trend of the FTIR intensities of aspartic acid (Asp) irradiated with increasing fluences of 30 keV N^+ (upper figure in Fig. 9) [166,167]. It is reasoned that the actual bombarding yield is greater than the mass loss, because some of the sputtered heavier particles may fall back onto the film or sample holder and cannot be measured. As calculated from the experimental data, the emission coefficient r is 290 lactamine molecules/ion or 3.8×10^3 atoms/ion [167]. This is three to four orders of magnitude greater than the sputtering yields of C, H, N and O calculated using classical collision cascade theory and also about 3 orders of magnitude larger than those of metals.

A second point about ion irradiation of amino acids is the structural alteration of the amino acid molecules in the target and formation of new products *via* chemical reactions. Based on the measured UV-, IR-, laser-Raman, and mass spectra in conjunction with quantum theory, Shao et al deduced the reaction pattern of an implanted N^+ ion with tyrosine molecule (Tyr) and suggested a substitution reaction between the decelerated N^+ and the group =C(5)H– of

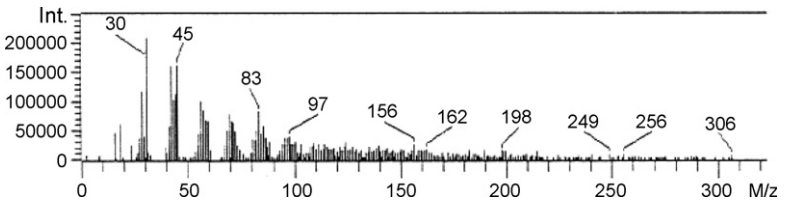

Fig. 8. . Secondary ions emitted from glycine under bombardment of 8 keV Ar atom. The peaks represent the emitted species, the ordinate gives the intensity of the peaks, and the abscissa gives the mass/charge ratio [164].

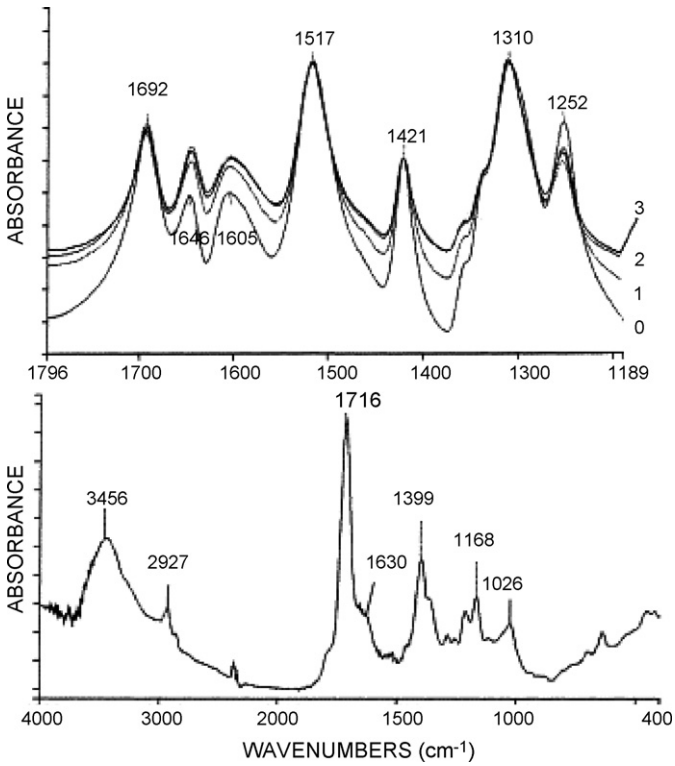

Fig. 9. Upper figure: FTIR spectra of Asp after N^+ irradiation at various fluences: (0) control, (1) 1×10^{16} ions/cm^2, (2) 2×10^{16} ions/cm^2, and (3) 4×10^{16} ions/cm^2. Lower figure: FTIR spectrum of Asp residue after bombardment at fluence of 1×10^{17} ions/cm^2. Reprinted with permission from [166]. Copyright 2000 by Elsevier.

the Tyr benzene ring. Moreover, a new carbonyl group is detected from the irradiated Tyr sample, and thus an N-heterocyclic compound has been formed, furnishing evidence of chemical reactions and mass deposition during keV ion irradiation of amino acid samples [168,169]. In solid Asp (aspartic acid) film irradiated with a high fluence (1×10^{17} ions/cm^2) of 30 keV N^+, the FTIR spectrum of the radiolysis residue displays a totally different pattern from that of Asp without ion implantation or with low fluence ion bombardment implying that Asp suffers considerable structural transformation upon ion bombardment (lower figure in Fig. 9). Moreover, progressive darkening of the irradiated samples from white, to yellow, yellow-brown, and even black with increasing ion fluences has been observed, and this is attributed to carbonization of the target surface [162,166]. In the FTIR absorption patterns, both the carbonyl group of acids and OH stretching vibration appear after ion bombardment, indicating that the main product is a fatty acid. Cui et al have further studied the secondary structure changes of the protein bovine serum albumin (BSA) induced by 30 keV N^+ bombardment [170]. The secondary structures of the BSA molecules are very sensitive to ion irradiation, and FTIR shows that with increasing ion fluences from 0 to 2.5×10^{16} ion/cm^2, the fractions of α-helix and β-turns decrease from 17 to 12% and from 40 to 31%, respectively, while those of the random coil and β-sheet structure increase from 18 to 27% and from 25 to 30%, respectively. These structural alterations in the proteins may be detrimental to the organism. F. Culard et al have shown that upon γ-irradiation, the regular complex between DNA and MCI, a DNA-binding protein extracted from the archaebacterium *Methanosarcina* sp. CHTI55 (used as an *in vitro* model system), disappears while a new complex appears. The protein is found to lose its ability to recognize its preferential binding sequences and DNA circles. After high fluence irradiation, the new complex disappears and the protein becomes totally inactivated [171].

2.4. Formation of amino acids in aqueous solutions by plasma discharge

Amino acids are the building blocks of proteins and probably play a key role in the appearance of life on the Earth. One school of thought is that the earliest organic compounds are synthesized elsewhere in the universe and delivered to

the Earth by asteroids, comets, and smaller fragments such as meteorites and interplanetary dust particles [172]. As some of these amino acids have been found in carbonaceous meteorites, the contribution of extraterrestrial amino acids synthesized in interstellar space and delivered to the Earth in the form of cometary dust offers an attractive alternative to a purely terrestrial origin of life on Earth [173–175]. Another hypothesis on the life origin is that life on Earth arose some four billion years ago as a result of a very specific sequence of chemical events. The environment of early Earth, for example, its surface atmosphere and/or the ocean's hydrothermal systems, may have provided the appropriate conditions for the spontaneous formation of organic molecules such as certain amino acids [176]. Near the surface of early Earth, a large amount of low energy particles generated by thunder, lightning, volcano eruption, and emission of radioactive elements from the crust have been detected. If these particles impact molecules in water or on the ground, there is a high probability that some organic molecules can be created in the targets, followed by the formation of more complicated organic molecules such as amino acids [158]. The abiotic synthesis of amino acids by electric discharge has been studied for many years and a well known synthetic pattern is the Miller–Urey type synthesis in which electric discharge is applied to a gas mixture containing CH_4, CO, N_2, H_2, and H_2O. In the reactions, amino acids are produced from carbon-containing compounds such as CH_4, CO, etc. in a gaseous atmosphere.

To simulate the interaction between low-energy ions and organics in a solution, a simple reaction apparatus for depositing low-energy ions into the solution or solid samples has been developed, as shown in Fig. 10. Gas discharge is triggered at atmospheric pressure to generate plasma ions and the samples in the solid or liquid form constitute the cathode region. The ions are injected into the samples via the plasma sheath at energies several tens to several hundreds eV [177–179].

Two types of experiments involving plasma discharge have been performed and the reaction products are determined by high performance liquid chromatography (HPLC). In the reaction of N^+ with carboxylate solutions (sodium acetate, sodium malomate, and sodium succinate), ammonia is produced. Glycine is produced in both sodium acetate and sodium malonate solutions by N^+ implantation for 10 h, and aspartic acid and glycine are produced in the N^+ irradiated sodium succinate solution. Here, in addition to N^+ which is the major species, the solution is probably implanted with N^{2+} as well as small amounts of N^- and electrons. Several active species can be produced in the solution by N^+ implantation and they include $^\bullet H$, $^\bullet OH$, $^\bullet NH_2$, $^\bullet R–COOH$, e_{aq}^-, etc. Hence, the final products may form by combination of these species. Since there is no nitrogen in the reaction solution and it is introduced into the solution from the plasma discharge, there is proof that the implanted low-energy N^+ can cause deposition and fixation of molecular nitrogen. This constitutes a new type of fixation of molecular nitrogen without the use of catalysts.

In another experiment, the discharge is sustained in an ammonia solution using a graphite rod as the anode and a silver thread as the cathode in an argon gas ambient. HPLC and thin layer chromatography (TLC) discloses the presence of three amino acids in the reaction mixture. As the graphite anode is the only source of carbon in the system, amino acids are probably produced by a synthetic reaction between graphite and the ammonia solution. It can be

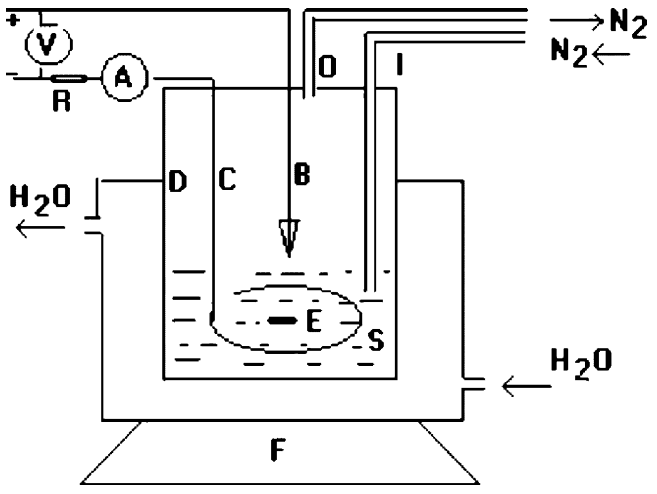

Fig. 10. Apparatus for reaction between elemental ions and solutions by plasma discharge (B: anode; C: cathode; D: glass container; E: magnet; F: magnetic stirrer; I: gas inlet; O: gas outlet; R: resistor; S: solution sample) [177].

envisaged that some interatomic bonds in the graphite are destroyed due to the high temperature in the discharge zone, and some carbon atoms escape from the graphite to create a localized homogeneous gas of excited atoms (C*). Some of these excited atoms can combine with H, O, and N in the solution to form amino acids.

In interstellar space, a lot of energetic particles come from the solar wind and some of these particles can reach the Earth surface and may play a role in the chemical evolution. Moreover, energetic ions containing nitrogen and carbon can be generated during lightning and the interaction between solar winds or cosmic rays with the primitive atmosphere. Therefore, the reactions described here may be partially responsible for the formation of ammonia or nitrogen containing compounds on primitive Earth.

2.5. Damage of DNA/RNA building blocks by low-energy ion collision

All ionizing radiation modalities (protons, heavy ions, electron, χ- and γ-rays) cause severe genotoxic, mutagenic, and carcinogenic lesions in DNA including single- and double-strand breaks, base damage, and clustered damage [63,180]. Double strand breaks of DNA have significant biological consequences being the main underlying mechanisms for cancer as well as controlled cell killing in radiotherapy [181]. Clusters of strand breaks and base damage of DNA occur when radiation interacts with DNA molecules, for instance, in heavy ion therapy involving carbon ions. Traditionally, DNA damage has been linked to thermal or solvated secondary electrons and the formation of reactive radicals. In the past decades, most experimental studies have focused on DNA damage by free radicals and solvated electrons and severe damage to DNA and its components can be induced by electrons with energies as low as 3 eV via the resonant mechanism [58,182]. So far, studies on charged ions with keV or lower energies are scarce, probably because biomolecular tissues such as cells cannot be used as targets but this area is attracting more attention and new results will likely be produced in the near future.

The most basic DNA/RNA components are the nucleobases, thymine (T, m = 126 amu), adenine (A, m = 135 amu), cytosine (C, m = 111amu), and guanine (G, m = 151 amu) together with the sugar ribose or deoxyribose. Adenine and guanine belong to the double-ringed class of molecules called purines, whereas cytosine, thymine, and uracil are pyrimidines that contain only one benzene-like ring structure. In RNA, thymine is replaced by uracil (U). These two bases are identical except that the uracil lacks the 5′ methyl group. A nucleobase bonds covalently with the 1′ carbon of a ribose or deoxyribose to form a nucleoside, and a nucleoside with one or more phosphate groups attached at the 5′ carbon is a nucleotide (Fig. 11).

2.5.1. Fragmentation of nucleobases, deoxyribose, and nucleosides

In most ion collision studies, molecules in the gaseous or solid phase are bombarded by energetic ions in a well-defined experimental apparatus. Gas phase studies are preferred when a detailed molecular mechanism is desired while solid phase studies are preferred when investigating the ionization energies and dissipation of the excitation energy. For a gas-phase interaction, the ion beam intersects the molecular gas of the target sample evaporated from an oven at a temperature that is high enough to introduce sufficient gaseous molecules but low enough to not cause

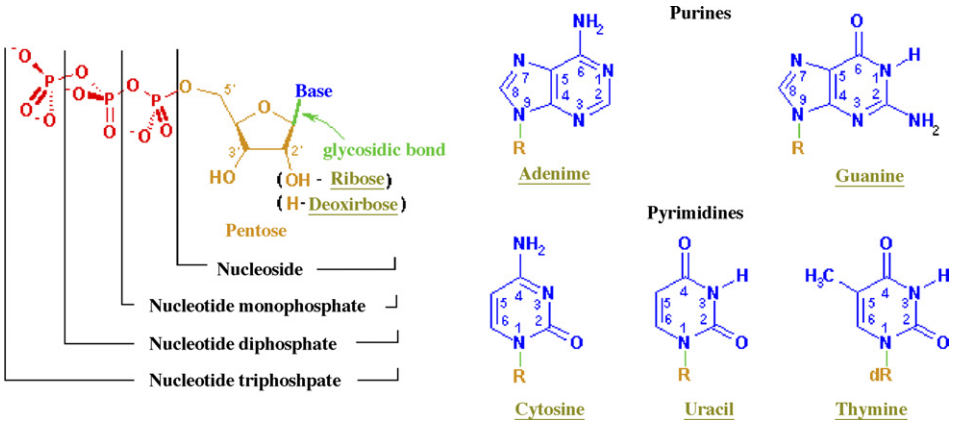

Fig. 11. Molecular structure of nucleotides and nucleobases (from Wikipedia, the free encyclopedia).

thermal dissociation of the molecules, for example, 170 °C for thymine. To study ion–solid collisions, in the early days, a water solution containing the target molecules is spread on a glass slide evenly and then dried in a desiccator or oven for a certain period of time. In recent years, a new *in vacuo* evaporation approach has been developed to prepare thin films of nucleobase or sugar molecules on an atomically clean, electrically isolated polycrystalline Pt substrate [62]. The film mass (ng/cm^2) is determined by the carefully calibrated deposition rate (ng min^{-1} cm^{-2}) and time, and thus it is possible to produce an even film consisting of only several monolayers of the molecules. The target density is normally much higher than that in the gas-phase environment. Presently, only small molecular weight biomolecules are suitable for the evaporation approaches. Larger structures such as DNA oligomers and plasmids cannot be evaporated without substantial thermal fragmentation and hence, the simple solution and drying method is still employed [180]. With regard to biological relevance, a more realistic environment should be clusters consisting of the biomolecules as well as water molecules thereby mimicking the natural environment. By means of mass and electron spectrometric measurements, especially time-of-flight (TOF) mass spectrometry, collision data such as fragmentation cross sections, fragment ion kinetic energies, and distributions of fragmented ion pairs can be obtained providing us with more understanding of the collisional events. A few groups have compared the interaction responses of nucleobases with various singly and multiply charged ions, with particular emphases on the fragment species and energies produced in each collision energy regime as well as the chemical and structural changes of the projectile and target molecules [183,184].

The mass spectra produced in these experiments show many fragmented cations and anions such as heavy atoms/clusters (C, O, N, C_3H_3, for instance) modified by the addition or loss of one or more hydrogen atoms (see Fig. 12 for a typical case). Comparing the spectra obtained by bombarding gaseous uracil with 1 keV/amu He^{2+}, C^{2+}, N^{2+}, and O^{2+}, the peaks obtained by He^{2+} bombardment are the most numerous but a large fraction of the spectra for the four projectiles are quite similar. In addition to small atomic species (H^+, C^+, etc.), heavier fragments and multiply-charged species of the target material are observed. For example, in the collision between 200 keV Xe^{10+} and solid nucleoside thymidine, fragments corresponding to the basic part (thymine) and osidic part (sugar) of the thymidine molecule are detected (upper figure in Fig. 13) [184]. It can be inferred that the C–N bond is broken by the interaction that separates the molecule into two large fragments. A similar two-body breakup in thymine [185] and uracil when bombarded with 6 keV/amu C^{6+} in the gas phase [183] has been identified. Here, the two molecular cation fragments, $HCNO^+(\pm H)$ and $C_3H_3NO^+(\pm H)$ (i.e., $[uracil\text{-}HCNO]^+$) are formed. Moreover, sputtering is observed in the 3 mm thick solid thymidine film bombarded by 400 keV Xe^{20+}, as shown in the lower figure in Fig. 13 [184]. In this spectrum, heavier ions and

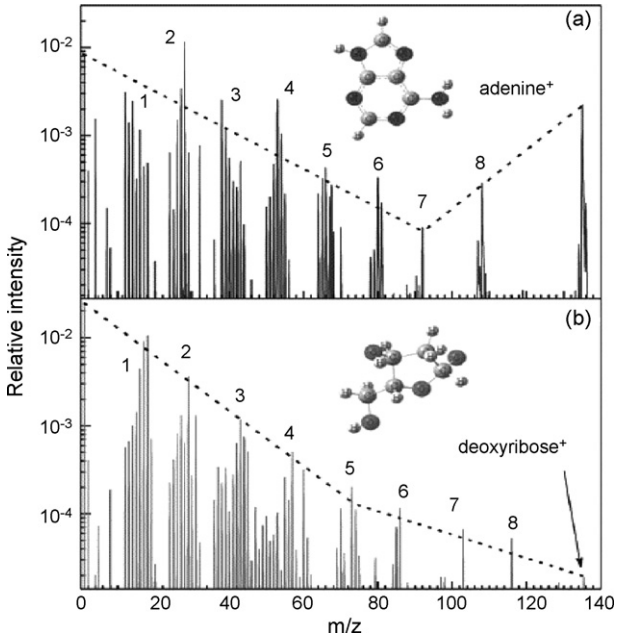

Fig. 12. Mass spectra of adenine (a) and deoxyribose (b) fragments after collisions with 5 keV/amu He^+ ions. As an inset in each graphthe structure of the correspondent molecule is shown. Reprinted with permission from [188]. Copyright 2006 by the PCCP Owner Societies.

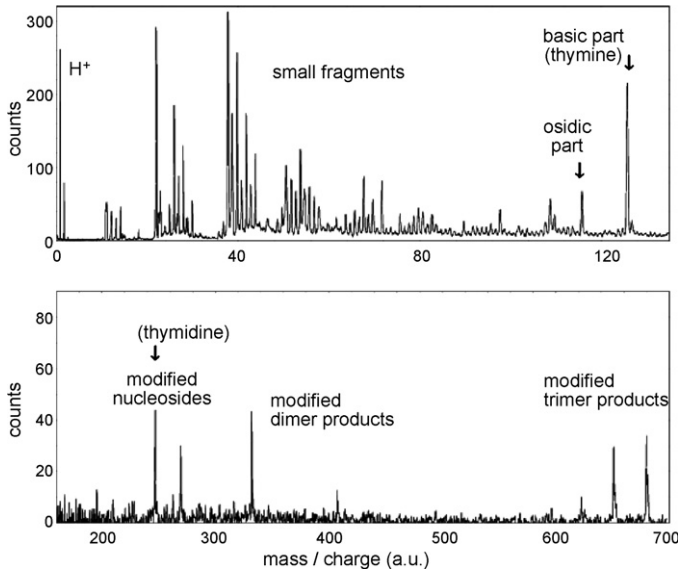

Fig. 13. Upper figure: mass spectra of thymidine, obtained in collisions with Xe^{10+} ions at 200 keV and a grazing angle of 5°. Lower figure: Xe^{20+} ions at 400 keV and a grazing angle of 20°. The count rates in both spectra are not to be compared. Reprinted with permission from [184]. Copyright 2003 by Elsevier.

clustered molecular groups are evident probably due to modification of the nucleoside thymidine and aggregated dimmers and trimers. It is reasoned that for a solid target, the large energy deposited into the surface leads to extensive fragmentation. The results suggest that ions with high charge states and high energies can more readily produce larger or parent molecular ions as well as dimmer and trimer cluster ions.

Since the chemical structures of uracil and thymine (replacement of one H atom in uracil by a methyl group) are similar, comparison of the spectra of these two nucleobases may impart information about the interactions between the projectile and target. It has been shown that after collision with 2 keV/amu C^+, the relative fragmentation yields are moderately different (74% for uracil versus 82% for thymine) and the spectra in the higher mass region are quite different. The spectrum of thymine [186] is more complex than that of uracil [187]. In 5 keV/amu He^+ collision with gaseous adenine $C_5H_5N_5$ and deoxyribose $C_5H_{10}O_4$, big differences have been observed (Fig. 12) [188]. The most obvious one is the strong parent molecular (adenine$^+$) peak in the spectrum. Both spectra show clearly defined groups of peaks (groups 1–8 in Fig. 12) representing fragments composed of different numbers of ''heavy'' atoms (C and N for adenine) and a variable number of hydrogen atoms. The patterns acquired from adenine and other nucleobases [186,187] exhibit a bimodal distribution with decreasing intensities reaching a minimum around group 7 for adenine and increasing intensities afterwards up to the parent molecule. In contrast to the nucleobases, deoxyribose shows a very small parent ion peak, and the overall peak intensities decrease monotonically with m/z. The larger fraction of small fragments of deoxyribose, or in other words, the higher stability of adenine, is thought to be related to the differential appearance energies (AE) of different fragments. For example, for group 8 in Fig. 12, in addition to the 8.2 eV ionization energy, only 0.3 eV of extra energy is needed to form the fragment at $m/z = 116$ for deoxyribose [189], which is much lower than the 3.34 eV required for the fragment at $m/z = 108$ in adenine [190]. Therefore, although some primary processes are understood, it is necessary to perform more thorough investigations on various DNA building blocks in order to fully fathom the ion-DNA interaction mechanism.

In terms of biomolecular radiation damage, the energies of the ion-induced fragment ions and emitted electrons and whether these energies are sufficiently high to induce further damage to surrounding molecules are of particular interest. In the case of 4 keV/amu C^{q+} ($q = 1$–6) collision with gaseous thymine, a charge dependent increase in the fragment kinetic energies of the ion pairs C^+–O^+, H^+–C^+, and C^+–N^+, up to 25 eV for C^{6+}, is observed and the details are displayed in Fig. 14 [183]. The damaging effects on condensed thymine (T), thymidine (dT) and deoxyribose (dR) impacted by hyperthermal (10–200 eV) Ar^+ ions have been further investigated by Michael A Huels and coworkers [62,63,182]. Similar to keV ion collision, different types of dissociation are observed. Many positive and negative ion fragments are formed by endocyclic and exocyclic bond cleavage (see legends in Fig. 15) [62,63]. Measurement of the

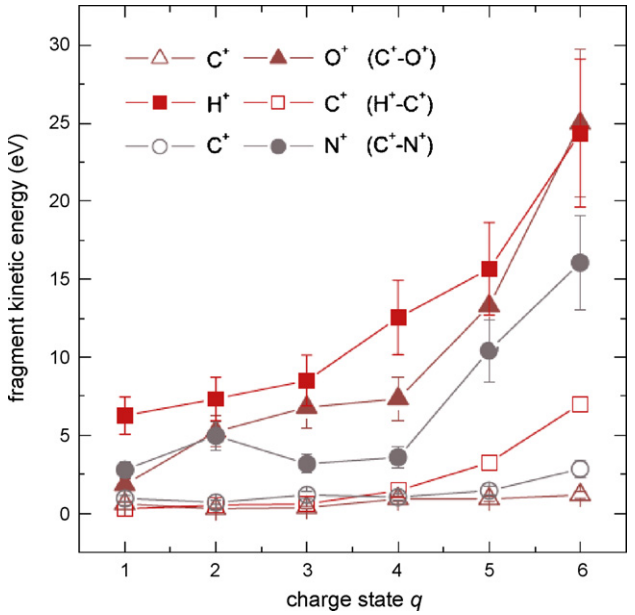

Fig. 14. Kinetic energies of atomic fragment ions from 4 keV/amu (C^+: 2 keV/amu) C^{q+}-induced fragmentation of thymine. The data has been obtained for three typical ion-pairs, as indicated in the legend. Reprinted with permission from [183]. Copyright 2005 by Elsevier.

dependence of fragment desorption yields with the primary ion energy shows that cation fragment desorption occurs at much lower threshold energy (15–20 eV) compared to anion fragment desorption, as illustrated in Fig. 15 [63]. The time-dependent fragmentation yields for 100 eV Ar^+ suggest a dissociation efficiency of about six thymine molecules per incident ion. According to the abundant fragmentation species originating from the sugar moiety, their high

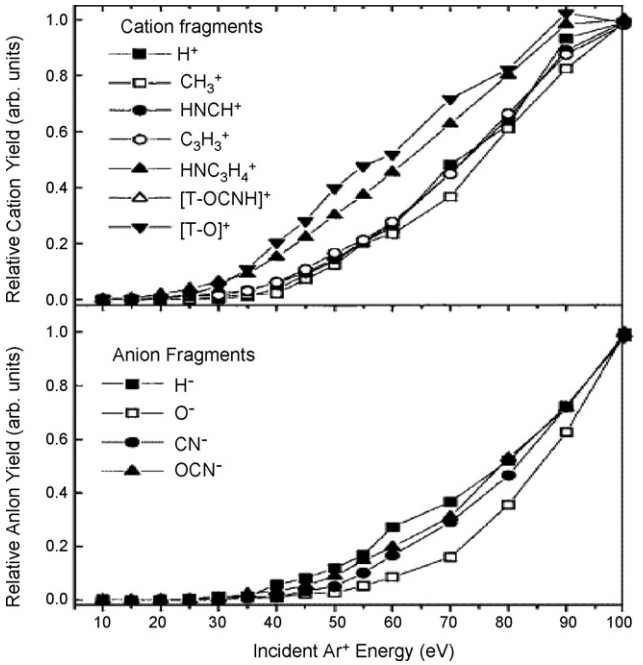

Fig. 15. Desorption energy thresholds of typical positive-ion (top panel) and negative-ion (bottom panel) fragments produced by 10–100 eV Ar^+ irradiation of thymine films. The relative fragment ion yields are normalized to 100-eV incident Ar^+ energy for ease of comparison. The cation fragments are measured from 200 ng/cm^2 films and the anion fragments from 100 ng/cm^2 films. Reprinted with permission from [63]. Copyright 2005 by the American Institute of Physics.

desorption yields and low desorption energy threshold, destruction of sugar appears to occur more readily. That is, the sugar backbone may be more fragile upon ion irradiation than the bases. This is in agreement with the cases of 5 keV/amu He^+ collision with gaseous deoxyribose (Fig. 12) [188] and also soft X-ray irradiation below 1 keV of deoxyribose, thymine, and guanine thin films [191]. This can be partially explained by the structural characteristics of the furanose ring that is in the puckered state rather than the planar state. Because of the twisted structure, the molecule has relatively high internal energy causing instability. In addition, the furanose ring does not contain unsaturated bonds which can help stabilize molecules against external electrical disturbance [191].

In summary, bombardment of main DNA building blocks by light and heavy ions at energies ranging from hyperthermal to keV has been investigated. Virtually complete disintegration of the molecule is invariably observed, but large molecular fragments and even parent molecular ions are frequently observed. The energies of these secondary species can be as high as a few tens eVs that are sufficient to cause subsequent dissociation of nucleobases and sugar moiety. Heavy ion impact even below 1 eV/amu can cause severe damage to nucleoside thymidine, including the release of the whole base, sugar moiety, and desorption of abundant low mass ring fragments from both. By comparing the fragmentation patterns of different DNA building blocks, deoxyribose is more sensitive than nucleobases to hyperthermal Ar^+ and keV He^+ impact. The results provide direct evidence that most secondary ions produced along the heavy ion tracks as well as those particles at track ends, for example, argon or nitrogen ions traversing through the seed coat, are able to cause severe damage to DNA constituents. It may lead to complex lesions of cellular genome.

2.5.2. *Ion irradiation of (deoxy)nucleotides*

A nucleotide is a chemical compound that consists of a heterocyclic base, a sugar, and one or more phosphate groups (Fig. 11). Ion induced damage can happen to the corresponding nucleotides. Phosphate ester cleavage and release of inorganic phosphate are important consequences of ionizing radiation of nucleotides and DNA leading to breaking of the strands [192]. Shao and Yu have investigated the damage of solid nucleotides (e.g., 5′-dTMP, 5′-AMP, 5′-CMP) after irradiation by 20–30 keV N^+ and release of both inorganic phosphate and free bases has been observed [193–195]. The yield of inorganic phosphate release exhibits a non-linear dependence on the irradiation fluence and is also affected by post-irradiation treatments. Heat and alkali treatments increase the yield of inorganic phosphate but an acid treatment decreases it.

More information about fragmentation of ion-impacted biomolecules can be obtained from fast atom bombardment mass spectra (FABMS) [196] and secondary ion mass spectra (SIMS) [197] because keV atoms and ions are quite efficient in causing ionization, secondary electron formation, ionizing fragmentation, and electronic excitation of molecules in the solid target. The two major collision-induced dissociation events of polynucleotide are base loss and backbone fragmentation [198]. The initial step of fragmentation is loss of the mucelobase either as an anion or neutral species, and the overall anionic base loss follows the trend: $A- \gg G- \approx T- \gg C-$ [199].

2.6. *Plasmid DNA damage upon low-energy ion irradiation*

The analysis of ion impact with small, defined DNA molecules in solution or solid reveals the effects of low or extremely low energy heavy particles at an atomic level. However, for better understanding of the damage effects induced by particle irradiation of genetic material, the target material has been extended from simple building blocks to small plasmid molecules up to genomic DNA of bacteria or even eukaryotes. Plasmids are typically circular double-stranded DNA molecules existing separately from the bacteria chromosomal DNA. Plasmid DNA in its native configuration has a compact, supercoiled conformation after extraction from host cells. One single strand break (SSB) allows relaxation and one double strand break (DBS) produces a linear molecule. The three conformations can be directly monitored by SEM or atomic force microscopy (AFM) [200–203], as illustrated in Fig. 16. It is clear from the AFM photo that most of the natural plasmids are in a double-strand closed state forming a twisting angle between two neighboring nucleotides. The tension caused by the negative supercoil brings the entire molecule to a supercoiling structure. If one of the strands is broken and the hydrogen bonds between the two strands are also broken, the tension is released *via* rotation of the strand, and the DNA configuration becomes an open circle. Radiation also gives rise to some open-circle DNA molecules from double strand breakage. If there are multiple breaking sites, linear plasmid or DNA segments can be produced. The linear plasmid and fragmented and damaged DNA may be cross-linked. Hence, the ion implantation induced effects on the plasmid configuration intrinsically reflect the laws of induced DNA atomic displacement, rearrangement, and polymerization. By using AFM, S. Brons et al compared the fragmentation pattern of $\varphi\chi174$ plasmids upon irradiation

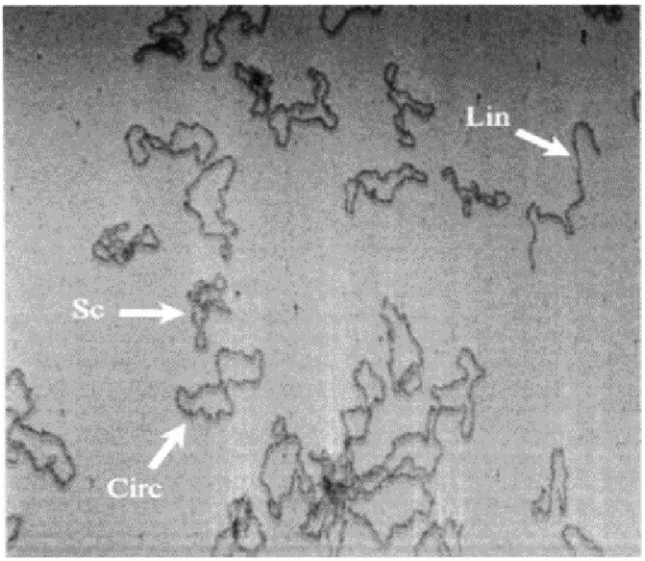

Fig. 16. AFM photographs of DNA in different conformations. Sc: supercoiled plasmid molecules. Circ: open circular plasmid, formed by a single SSB. Lin, linearized plasmid molecules, formed by severe DNA damage, perhaps one or more DSBs. Reprinted with permission from [200]. Copyright 2004 by Elsevier.

with heavy ions and X-rays. The fragment distributions resulting from low ion fluence bombardment of ^{59}Ni beams shift to smaller fragment sizes compared to those obtained after similar dose X-ray irradiation. Even with single ion traversals, the resulting average fragment length is significantly smaller than the full plasmid length [200]. The exact fraction of the three main conformations of plasmid DNA can be distinguished on the basis of their different electrophoretic mobilities on agarose gels. According to the relative amounts of each form after ion irradiation, the fluence or energy effects can be established and cross sections for SSB or DSB induction can be calculated.

2.6.1. Naked plasmid irradiated by low-energy ions

Low-energy ion irradiation induced SSB and DSB in plasmid DNA molecules have been studied using pUC18 and pGEM3zf plasmid DNA [95,204,205]. A plasmid DNA solution with a concentration of 50–500 ng/μl is normally deposited on a defined area on an ultrasonically cleaned gold or aluminum foil. The volume of DNA influences the experimental results significantly. A larger DNA volume on a fixed area leads to a thicker DNA layer, and because of the limited penetration depth of low-energy ions, a thick layer prevents irradiation of the molecules underneath. In 20–100 keV, 1×10^{15} ions/cm^2 N^+ irradiated pGEM3zf(+) DNA, the production of DNA with single-strand and double-strand breaks increases initially and then diminishes with increasing ion energy. The maximum ratio between the yields of DSB and SSB (Y_{DSB}/Y_{SSB}) is 1/2.48 at 60 keV ion energy, which is the highest Y_{DSB} at this point. The underlying mechanism is deduced in accordance with the nuclear stopping and ion deposition effects. Basically, the physical mechanism of low-energy ion irradiation is different from that of conventional ionizing radiation such as γ-ray and high-energy ion irradiation. Nuclear stopping is more important to DNA strand breaks compared to electronic stopping. DNA strand breaks depend on not only the deposited energy but also the spatial distribution of the incident ions.

Similarly, with even lower ion energy, for example, 1 keV Ar^+, 14.5%, and 16.8% circular relaxed DNA (SSB) are present in the pUC18 plasmid molecules after irradiation with a total of 1.2×10^{14} and 2.4×10^{14} ions, respectively. The fraction is more than twice that of the vacuum control sample (∼7%). In this case, the DSB/SSB ratios after 1 keV Ar^+ irradiation of pUC18 plasmid are much lower than the aforementioned 60 keV N^+, with values of 1.3%/14.5%, 0.7%/13%, 1.5%/16.8%, 1%/17%, and 1.4%/20% for irradiation with 1.2, 1.8, 2.4, 3.6, and 7.2×10^{14} ions. In order to analyze the properties (size, volume, number of molecules) of plasmid DNA on the gold substrate, ion scattering SRIM simulation making use of the composition and density of DNA is performed. The penetration depths of 1 and 5 keV Ar^+ are on the order of 6 and 25 nm, respectively. When the ten layers of pUC 18 molecules distributed in the 40 nm pattern is taken into account, it is noticed that only part of the DNA can be penetrated by the Ar^+ ions. The numbers of vacancies or atomic displacements produced directly and indirectly by recoils due to 1 and 5 keV argon ions are about

12 and 60 per incident ion. Hence, it can be deduced that multiple damage extending over a region of several tens of base pairs can occur. In other words, in the regime of low keV ion irradiation of naked plasmid DNA molecules, significant localized damage can occur by elastic energy transfer and recoils. A single strand break can occur by for example, knocking a phosphorus atom out of the backbone [193,194], whereas a DSB can occur by successive collisions between the incoming ion and atoms in the two strands or alternatively, the second strand can be broken by recoiled atoms.

When pGEM3zf(+) DNA is irradiated by 30 keV N^+ of fluences ranging from 2×10^{10} to 8.2×10^{13} ions/cm^2, the production of single and double strand breaks (SSB, DSB) as well as multiple DSB can be quantified by neutral electrophoresis and image analysis software. Both the SSB and DSB are induced by N^+ irradiation, as demonstrated by the increased amount of relaxed and full-length linear plasmid for low fluences shown in Fig. 17. It is also evident in the figure that these two forms of plasmid do not continue to accumulate as the fluence increases. On the contrary, the amount of supercoiled plasmid DNA decreases to a certain level and then remains more or less unchanged at higher fluences, but this reduction is not balanced by an increase in the relaxed and full-length linear plasmid, the amount of which decreases further as illustrated in Fig. 17b. However, when a higher agarose gel concentration is adopted, for the ion fluence 1.6×10^{11} ions/cm^2, this part of ''missing DNA'' appears as smears which are the characteristic electrophoresis patterns for short DNA fragments. The smears indicate a higher migration rate and they eventually disappear when the fluence is further increased. This phenomenon shows that fragmentation of plasmid DNA occurs during ion irradiation and the fragments become smaller at high fluences. That is, the damage becomes more severe when higher ion fluences are applied. Further experiments involving irradiation of supercoiled and linear plasmid DNA reveal that the maximum amount of plasmid DNA that can be converted to fragments by nitrogen ions is the same for both conformations. However, the ratio of efficiencies of DSB and SSB production is about 6:1 indicating that production of DSB is much higher than that of SSB, and DNA fragments are the major form of damage produced by nitrogen ion irradiation. In Fig. 17, for a fluence of 1.6×10^{11} ions/cm^2, the sample loses about half of the full-length plasmid, which is equivalent to 5.7×10^{10} molecules as calculated from the volume and covering area ($\sim$0.5 cm^2) of the sample. In this area, the number of irradiating ions is 8×10^{10}, and so each plasmid receives less than two incident

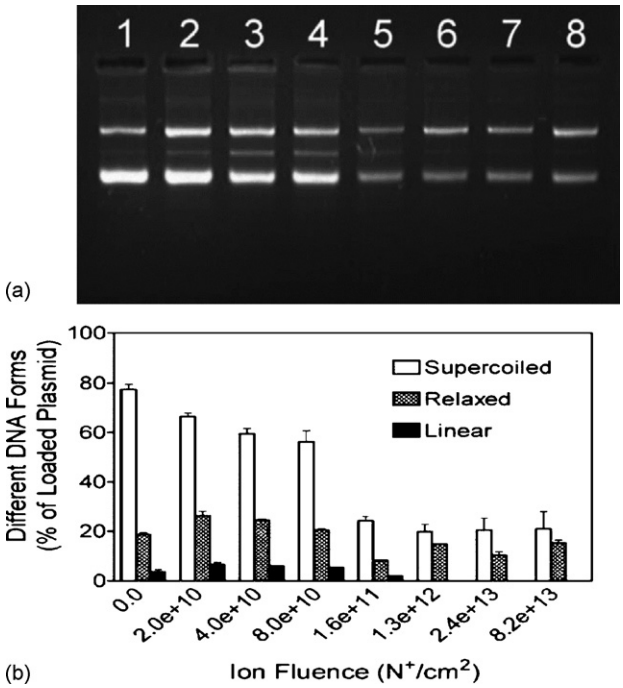

Fig. 17. (a) Effect of N^+ irradiation on plasmid DNA. Supercoiled circular plasmid DNA are irradiated with 30 keV N^+ with fluences of (1) 0; (2) 2×10^{10}; (3) 4×10^{10}; (4) 8×10^{10}; (5) 1.6×10^{11}; (6) 1.28×10^{12}; (7) 2.4×10^{13}; (8) 8.2×10^{13} N^+/cm^2, respectively, separated on 1.4% agarose gel and visualized by ethidium bromide staining. (b) Quantification of the various forms of plasmid DNA after N^+ irradiation. Samples are irradiated and processed as in (a). DNA bands are quantified and data are the average of two independent experiments. Reprinted with permission from [204].

ions on the average. Since one plasmid has to experience at least two DSBs to be fragmented, it is concluded that each nitrogen ion produces more than one DSB. The surprisingly high fraction of DSB compared to SSB contrasts the results discussed previously. It suggests a complex process for the strand breaks induced by keV ion irradiation, and thus more elaborate investigations are necessary. Nevertheless, some general points can still be drawn: (1) keV ions are able to induce both DSB and SSB and even fragments in naked dry plasmid DNA. (2) Due to the short range of low-energy ions, the sample attributes, e.g. the thickness and uniformity of the DNA layer on top of the substrate, affect the irradiation dynamics and greatly influence the observed results. (3) There is a shielding effect again originating from the limited penetration depth of low-energy ions. Reduction of the full-length plasmid reaches a certain level beyond which irradiation does little additional damage to the shielded DNA. (4) Nuclear stopping plays a more important role than electronic stopping causing displacement of target atoms and subsequent collision cascades which lead to multiple damage including bond breaking, molecular dissociation, and fragmentation. (5) A number of factors can affect the interactions between the incident ions and DNA molecules. They include the thickness of the plasmid DNA on the substrate, ion energy, accumulated surface charge, ion fluence rate, total fluence, conformation of dry DNA in vacuum, and presence of salt and water molecules in the inner salvation shell of DNA in vacuum [206].

2.6.2. Irradiation of plasmid in E. coli

The cellular response to ionizing radiation is mainly determined by damage to DNA. DSBs constitute critical lesions which can lead to mutation and transformation or cell death if not correctly repaired. A good way to elucidate the mechanism is to irradiate the DNA *in vitro* and then transfer the DNA to host cells where the induced DNA lesions may be partially repaired or inherited *via* enzymatic reactions and post-irradiation replication. The mutation rate and mutagenic spectrum of the DNA bases in the plasmid can be determined by sequence analysis. Plasmids M13mp18 with *LacZ*$^-$ gene implanted by N^+ and $^{12}C^+$ *in vitro* are transferred into the host bacteria JM103 *E. coli* and cultured overnight on selective agar plates. *LacZ* mutants are then selected, and for each mutant, the DNA fragment containing the *lacZα* gene is amplified by polymerase chain reactions with primers designed according to the *lacZ* sequences available at Genebank [207,208]. In 30 keV N^+ irradiated plasmid, ten mutants are selected and subjected to sequencing [208]. Seven of these mutants contain base changes and 5 of them even have 5–6 mutation sites in the 250 bp region examined. That is, there is one mutation per 40 bases on average. This dense distribution of base changes in multiple sites has seldom been observed in X-ray-, γ-ray- and UV-induced DNA mutation. The dominant kind of ion-beam-induced *LacZ*$^-$ mutation is replacement (95%) whereas base deletion constitutes only 5%. Insertion or replication of bases is not detected. In base replacement, transition and transversion constitute half and half. All four forms of bases that compose DNA can be mutated by ion implantation, but cytosine is the most sensitive accounting for about 60% of the total mutation.

For 30 keV $^{12}C^+$ irradiated plasmid M13mp18 DNA, at 49–33% survival fraction, the induced mutation frequency exceeds the spontaneous level by approximately 3.7–5.6-fold [207]. In all of the 94 induced mutations, the majority are base substitutions (56.4%) and most of them involve G:C base pairs (90.6%, 53/94), mainly G:C → T:A transversion, and G:C → A:T transition. There are also considerable frameshift mutations (43.6%, 41/94) and most of them are one-base deletion (36/41) (Table 2). This phenomenon is rarely observed in experiments using conventional ionizing radiation and non-ionizing radiation for direct mutation of DNA.

Changes of base sequences described above are based on plasmids irradiated *in vitro* followed by cellular processing. However, the cellular DNA molecules interact with many other molecules and chemicals such as DNA binding proteins, and so the *in vivo* environment of the DNA molecule is more complex than that of naked DNA. To directly identify the specificity of low-energy ion induced base substitutions in living organisms, a novel experimental system has been established based on rifampicin resistant (Rif^r) mutant screening and sequencing of the defined region of the *rpoB* gene in *E. coli*. Mutational spectra of base substitutions induced in living *E. coli* cells by either 10 keV N^+ or ^{60}Co-γ ray have been compared.

At the same cell killing rate (50% survival fraction), the Rif^r mutation frequency for ion implantation is 9.5×10^{-7}, which is about ten times higher than that of ^{60}Co-γ ray (9.3×10^{-8}). Fifty independent Rif^r mutants for each mutagen are selected and sequenced to scrutinize their mutation sites in *rpoB* gene. The N^+-irradiation-induced mutation sites in the *rpoB* gene reaches 89, while that induced by ^{60}Co-γ ray is only 51. The transitions prominently account for 75.28% and 84.31% of base substitutions induced by N^+ beam and ^{60}Co-γ rays, respectively. The preferential base substitutions induced by nitrogen ion implantation are CG → TA transitions, AT → GC transitions, and AT → TA transversions, which account for 92.13% (82/89) of the total mutation [96]. On the other hand, the types of base substitutions are different for the two mutagens. Two types of base substitutions (GC → CG transversions, AT → GC transitions) are

Table 2
Examples of all types of lacZα mutations in the $^{12}C^{+}$ ion induced and spontaneous mutation spectra [207]

Mutational type	$^{12}C^{+}$ ion induced (%)	Spontaneous (%)
Substitution	53 (56.4)	10 (71.4)
G:C → A:T	21 (22.3)	3 (214)
A:T → G:C	3 (3.2)	2 (14.3)
G:C → T:A	26 (27.7)	4 (28.6)
G:C → C:G	1 (1.1)	0
A:T → C:G	2 (2.1)	1 (7.1)
Deletion	39 (41.5)	2 (14.2)
−A	17 (18.1)	0
−T	3 (3.2)	0
−C	8 (8.5)	0
−G	8 (8.5)	1 (7.1)
−GT	1 (1.1)	0
−GA	1 (1.1)	0
−GCG	0	1 (7.1)
−7 bp	1 (1.1)	0
Insertion	2 (2.1)	2 (14.3)
+T	1 (1.1)	0
+C	1 (1.1)	1 (7.1)
+11 bp	0	1 (7.1)
Total	94 (100)	14 (100)

induced by the nitrogen ion beam, but are not found in cells treated with ^{60}Co-γ ray. The AT → CG transversions are not found in nitrogen ion implantation but occur in cells treated with ^{60}Co-γ ray. The most significant trait in the frequency of specific kinds of mutations induced by N^{+} beam is that the CG → TA transitions increases substantially from 32 to 46, and the AT → TA transversions double from 7 to 15 in 50 mutants, as compared to the frequencies of γ ray-induced mutations. In most cases, the gene mutation rate and mutation efficiency of ion implantation in naked plasmid DNA or bacteria are greater than those due to γ-ray radiation. The more pronounced characteristics of ion-beam-induced gene mutations are high density, multi-point base mutations as well as some tropism.

3. Low-energy ion interaction with organisms

As discussed in Section 1.4, the primary interactions between implanted ions and biological organisms are quite complicated due to the complexity of the organisms. Ion implantation is characterized by not only energy absorption but also mass deposition and charge transfer. These three factors act on the biological organisms and induce damage in concert. The effects may be described in terms of formation, reaction processes, and final products. The established theory on the interactions between energetic ions and non-porous solid material is based on the bullet-target system. In this system, derivation of the incident ion energy loss is based on the assumption of a continuous, homogeneous distribution of the target atoms much larger than the ion range. However, no material is ideal in reality and there are always impurities, defects, and crystalline channels. Fortunately, for metals and semiconductors, these defects are of the atomic scale and can be described quantitatively. Hence, the ion implantation theory based on atomic collisions and solid state physics is usually quite accurate and agrees with experiments. However, there are seldom homogeneous and continuous distributions of atoms in organisms and they also change with time. These characteristics result in different collision processes that will be discussed in this section. Here, calculations by classical theories on ion implantation into organisms with simulated structural frame are presented first, followed by experimental results pertaining to ion-bombardment-induced damage in plant tissues and profiles of incident ions in botanic samples.

3.1. Monte-Carlo description of the collision process [1]

Biomolecules and elements of which organisms are made do not exist uniformly inside the organisms but rather are distributed in different units and macromolecules. For example, the basic unit of proteins is amino acid and the unit of

nucleic acid is nucleotide. Each structure is characterized by the types of chemical bonds. A primary structure consists of a linear series of units held together by covalent bonds. Secondary structures are formed by poly-chain series held together by non-covalent bonds such as polar or hydrogen bonds. Tertiary structures are the results of folding of ordered polymers. Quaternary structures are formed by interactions among the folded polymer molecules and other aggregates. For instance, nucleic acid exists only inside the nucleus, mitochondrion and chlorophyll, and these subcellular structures occupy only a very small part of the total cell volume.

Calculating the energy loss of the implanted ions in such a complex target is much more difficult than that in a non-porous, homogeneous solid material. A Monte-Carlo approach is often used to simulate the collision process between projectile and target atoms. The basic idea of the simulation is to trace the development of the collision cascade for each incident ion traversing the target. The SRIM program assumes the target to be a homogeneous medium where target atoms are distributed. At each atom location, the program calculates the energy loss due to each collision as well as the angular distribution, defect distribution, collision cascade process, atomic displacement, vacancy production, ionization, and excitation so as to determine the trajectories of all atoms in the collision system.

Suppose that there is a micro-volume in living cellular material in which the four main elements, N, H, O, and C (with atomic ratios 1:5:2:2), are *homogeneously* distributed with a density of $\rho = 1.6$ g/cm^3. The critical displacement energy of the four elements is $E_d = 20$ eV and the binding energy of the lattice is 1 eV. N^+ is implanted normally into the target at 30 keV and a Monte-Carlo approach is used to simulate the ion–target interactions. Successive calculation on a large number of implanted ions yields a statistical average of the implanted ion action and a physical picture of the collision cascade is displayed in Fig. 18. It can be seen from Fig. 18a that the implanted ion trajectories are quite complicated. The target contains atomic species that are the same as the incident ion species (i.e., N) and their stopping powers and subsequently the energy loss profiles are different. Based on the SRIM2003 calculation of 1000 incident ions, the mean range of the incident ions is 90.3 nm and the transverse distance is 20.2 nm. Each incident ion produces 250 vacancies. The energy loss is distributed as follows:

- energy gained by ionized molecules that are directly produced by the incident ion: 42.6%;
- energy gained by ionized molecules that are produced by recoiled atoms: 22.4%;
- energy loss by the incident ion in producing vacancies: 0.2%;
- energy loss by recoiled atoms in producing vacancies: 0.6%;
- energy gained by phonons produced by the incident ion: 2.8%;
- energy gained by phonons produced by recoil atoms: 31.7%.

Fig. 18b shows the depth distribution of the implanted species. It can be observed that the concentration distribution has a peak resembling a Gaussian distribution. Although the mean implantation range is 90.3 nm, the 50 nm thick region from 70 to 120 nm contains 69.6% of the total number of implanted atoms. For an implantation fluence of 1×10^{16} ions/cm^2, the total number of implanted ions in this 50 nm range is 6.96×10^{15} ions/cm^2. If the target molecule is assumed to have a molecular weight of 75, one can calculate that the areal number of target molecules in this range is 6.42×10^{16} molecules/cm^2. Hence, the ratio of the number of implanted ions to target molecules is 0.696/6.42 = 10.8%. If the implanted ions combine with the target molecules, the properties of the target can be altered significantly, even if the energy deposition effects (damage) are not taken into account.

Each incident ion can lead to displacement of each of the four target atoms, C, N, O, and H. Fig. 18c shows the distribution of displacement collisions for these four atoms. Statistical results (including cascade effects) show that each 30 keV N^+ ion can displace 72.12 carbon atoms, 99.64 hydrogen atoms, 74.02 oxygen atoms, and 37.02 nitrogen atoms. That is to say, each incident ion can displace a total of 282.8 target atoms. Since the ratio of the four elements is C:H:O:N = 2:5:2:1, the relative probabilities of displacements of the elements are 72.12/2: 99.64/5: 74.02/2: 37.02/1 = 36.06: 19.93: 37.01: 37.02. This indicates that the displacement probabilities follows the order of $N > O > C > H$.

In the case of implantation of a large number of ions, the damage to the target molecules by displaced atoms is many times greater than that due to implanted ions alone. According to the above calculation, the total number of displaced atoms is 2.828×10^{18} cm^{-2} when the implantation fluence is 1×10^{16} ions/cm^2. The calculation yields a maximum depth of the displaced atom distribution of 160 nm, and the number of target molecules in this depth is about 1.93×10^{17} cm^{-2}. If each molecule possesses 10 atoms, the number of target atoms at this depth is 1.93×10^{18} cm^{-2}. Thus, each target atom moves on the average about $2.828 \times 10^{18}/1.93 \times 10^{18} \approx 1.46$ times through a distance of

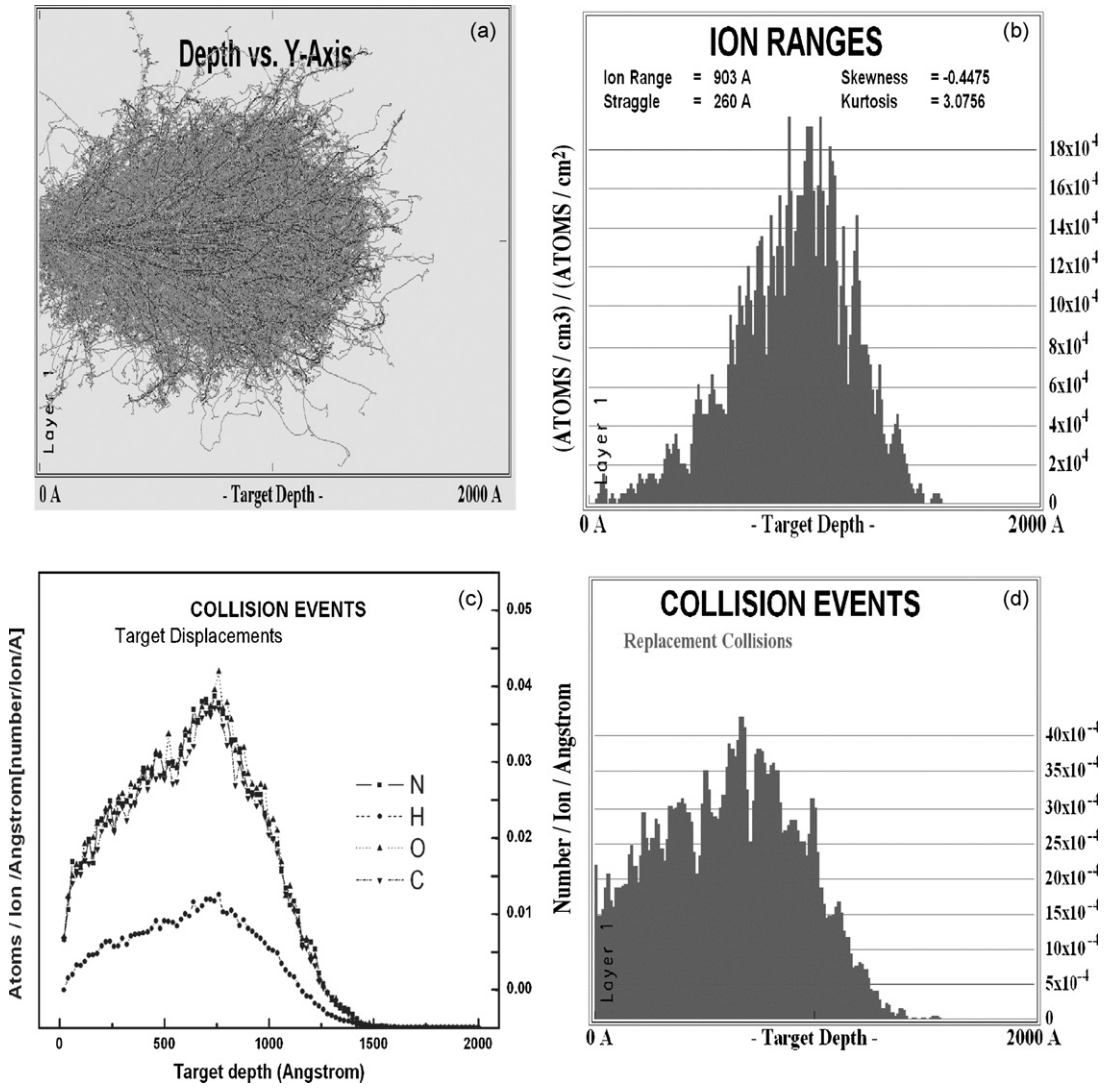

Fig. 18. SRIM calculations of ion implantation into a target consisting of N, H, O, and C at atomic ratio of 1:5:2:2. (a) Ion trajectories; (b) ion range and depth distribution; (c) target replacement collision distribution; (d) projectile displacement collision distribution.

160 nm. The depth distribution of displacement collisions shows a peak (Fig. 18c) where the target molecules are rearranged to form new molecular structures.

After coming to rest, the implanted ions may continue to undergo replacement reactions with the target atoms (Fig. 18d). The replacement collision distribution also shows a peak with depth. Comparing Fig. 18b and d, it can be seen that not all of the implanted ions result in replacement. The replacement reactions mostly take place near the target surface. Because the replacement reaction needs energy and the implanted ions have a thermal energy that is lower than the replacement reaction energy, the implanted ions are deposited further from the surface while the replacement reactions occur near the surface.

In accordance with the above calculation, all the elements in this micro-volume are displaced from their original sites and a large number of implanted nitrogen ions, which accounts for 10.8% (when implantation fluence reaches 1×10^{16} ions/cm^2) of the total number of target molecules, have been transported into the volume. Although scientists do not exactly know what kinds of reactions happen in the volume, it can be inferred that rearrangement and combination of displaced atoms, stopped ions, and target atoms cause significant change and damage to the target molecules.

3.2. Instrumentation and methodology

3.2.1. keV ion beam instrumentation and survival of organisms in vacuum

Although Monte-Carlo calculations give us a general concept for specific ion–target combinations, experiments must be performed to accurately investigate ion implantation into complex organisms. Experimental methods and facilities pertinent to ion bombardment of living organisms have been developed. The basic components of an ion implanter include an ion source, ion acceleration collimation transport system, and target chamber. This apparatus can be either a part of a larger ion beam facility or a stand alone unit. A major difference between ion beam processing of organisms and metals or semiconductors is that the biological objects being bombarded are live. Since ion implantation is typically conducted in a vacuum environment to increase the ion mean free path and reduce gas-phase collisions, it is imperative that the organisms are able to survive such an environment. Hence, there are added constraints on the ion beam facility and experimental procedures that are usually not of concern in traditional ion implantation experiments involving non-living material. In addition to a proper design, especially the vacuum system, the effects of vacuum stress on the living objects must be taken into account when the biological effects of ion bombardment are evaluated.

One viable means is to generate the ion beam separately in vacuum and then introduce it to a sample chamber in which the samples are bombarded at atmospheric pressure [209]. Such facilities are now feasible by virtue of applying polymeric nuclear plastics such as Mylar polyester and kapton polyimide films (Tomy-Dupon Co. Ltd.) at the beam exit vacuum window [210]. These materials have micrometer thickness, good resistance to pressure, very low degree of beam widening, and outstanding resistance to decomposition or other changes due to exposure to ionizing radiation. These characteristics make them good candidates in radiation research such as nuclear track detectors, vacuum seals, and even substrates for cell cultures.

In ion implantation experiments dedicated to genetic modification, a large number of samples are usually treated and the ion beam must penetrate a sufficient depth, for example, the embryo of crop seed. This is not a problem for high-penetration mutation sources such as γ-rays, but may present a problem with ion beams because of the more limited ion ranges. At the same time, since the ion beam size tends to be small, mechanical scanning must be used in order to implant a large area uniformly. However, such a maneuver may perturb the sample alignment and orientation. Beam scanning employing electrical or magnetic means is impractical for large area implantation either. Therefore, the ion beam used for mutation breeding purposes is usually as large and homogeneous as possible.

In order to study the mechanism of heavy-ion-induced damage in organisms, the ions should be implanted accurately and quantitatively into specific parts of the organisms, so that biological responses such as *in vivo* observations of single/double DNA strand breaks (SSB/DSB) and cellular repair dynamics after DNA damage can be evaluated with high temporal and spatial resolution [211,212]. Mass spectra derived from fast ion desorption or photon and electron emission induced by ion impact can be used to measure the cellular fine structures at the atomic and molecular levels. Some particular kinds of ion beams may even be used for cell surgery or crafting. All of these applications require a beam line with good spatial and current resolution. Therefore, ion beams used in life sciences usually fall into two categories: high-current broad beams and micro beams equipped with high-performance detectors.

3.2.1.1. Beam facilities for ion implantation of organisms inside or outside vacuum. Although processing of bio-samples requires a special ion beam facility, the basic structure does not differ very much from that of an industrial ion implanter. For example, the facility installed at Chiang Mai University, Thailand for ion beam processing of plant tissues and bacteria consists of 30 keV ion source, beam sweeper, and profile monitor. There is a sample load-lock with an AFM (atomic force microscope) [213] for *in situ* surface measurements and a TOF-SIMS (time-of-flight secondary ion mass spectrometer) for diagnostics and surface sputtering studies [214].

An irradiation system named Irradiation Apparatus for Cell (IAC) installed on a 3 MV tandem electrostatic accelerator at JAERI (Japan Atomic Energy Research Institute, Takasaki) can provide He^{2+} and C^{5+} beams outside the vacuum for controlled irradiation of biological samples. In this system (Fig. 19), the 1.5 MeV/amu ion beam passing through the beam window reaches the biological sample under atmospheric pressure positioned on the hexagonal sample holder column [209]. The column is movable from 5 to 48 mm from the window with 1 mm steps. Uniform irradiation is accomplished by scanning the ion beam and rastering the sample holder column at a speed of 3.5 cm/s. Because the beam intensity attenuates severely outside the vacuum, detailed calculation and experimental

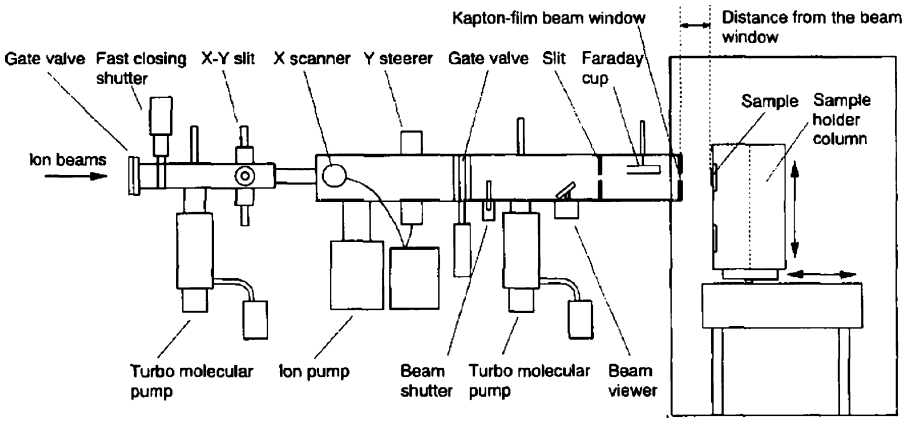

Fig. 19. Schematic diagram of irradiation apparatus for cell (IAC) connected to a beam line of 3 MV tandem accelerator. Reprinted with permission from [209]. Copyright 1997 by Elsevier.

measurements of beam parameters such as energies, stopping powers, and changes of fluences with distances have been compared and ascertained by both theoretic estimation using air and simulated biological composition as targets and measurements via nuclear detectors and bacterial cells of *Deinococcus radiodurans*. It has been demonstrated that the range of an ion beam in biological material can be controlled linearly by changing the distance between the beam window and target in air, although the fluence decreases at the end of the beam range. In the very low-energy range around the end of the penetration range, ion beam causes the most evident physical lesion in the pollen envelop of tobacco [215]. The combined effects of electron and nuclear stopping result in the observed damage.

If ion implantation is carried out in vacuum, several points should be taken into account. Firstly, in the case of dry seeds, a large implantation area is desired for subsequent mutation breeding, and thus a beam with a large diameter and good spatial uniformity is required. Secondly, in order to accommodate a large number of dry seeds in vacuum (normally 1500–9000 grains of seeds in one experiment), a pump with a high pumping speed is required. Thirdly, for materials other than dry seeds, for example, cells, plant calluses and fish embryos that contain more water than dry seeds, their survival in the vacuum chamber must be addressed. Usually, it is inadvisable to load biological samples that have a large quantity of intrinsic water into the chamber in advance for prepumping for 30 min or even longer.

A differential pumping vacuum system incorporated in a vertical beam line has been successfully used to implant both dry crop seeds and water-abundant objects. The schematic diagram of its vacuum chamber is displayed in Fig. 20. The main chamber is 90 cm in diameter and 1.0 m in height. A rotating plate 80 cm in diameter is located on the bottom of the chamber. There are six 20 cm diameter concave holes on the plate but only one of them is open all the way through. Six 20 cm diameter sample dishes can be put onto the concave holes and there are holes of different diameters in the sample dishes to hold the crop seeds. Samples of the same type, for example, rice seeds, are placed in the sample dishes and then affixed onto the large rotating plate. The angle of the plate is adjusted to align one of the dishes with respect to the incident ion beam. After the first dish has been implanted, the other dishes are automatically aligned sequentially with respect to the ion beam by a computer which also controls the implantation parameters. In this way, six different groups of samples can be implanted using different conditions in a single cycle. The small chamber located under the main chamber has a volume of about 1.2 litre, and the volume ratio of this chamber to the main chamber is about 1:600. The two chambers are separated by an isolating valve and constitute a differentially pumped system. It is able to create a vacuum rapidly in the small chamber and thus shortens the pump down time for water-rich samples.

3.2.1.2. Survival of mammalian cells and Caenorhabditis elegans in vacuum [1,216,217]. In spite of differential pumping, living cells will undergo changes when loaded into the vacuum chamber. Cells and calluses contain a large quantity of water, and thus their state in vacuum is completely different from that of crop seeds. For simplicity, a cell can be considered to be a water droplet. When a group of cells is under vacuum, evaporation of water causes the temperature in the cells to drop precipitously, and the lower the pressure in the chamber, the lower the cell temperature. When the liquid–vapor equilibrium is reached, the temperature at the interface of the two phases is a constant. For example, if the pressure in the chamber is 10^{-2} Pa, at which point the ion source can be operated normally, the

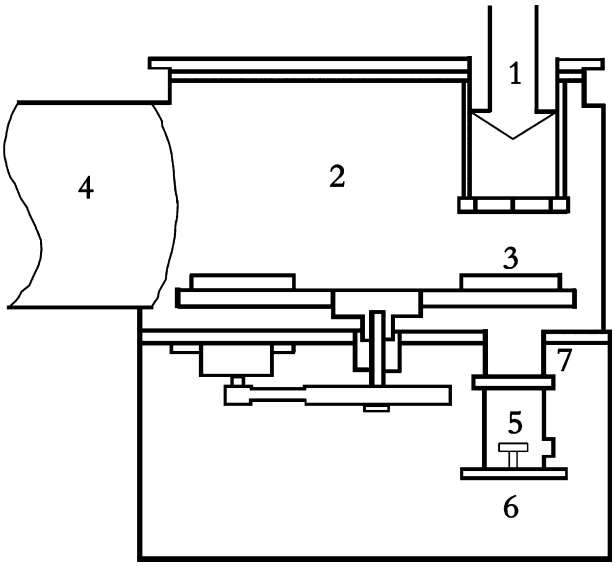

Fig. 20. Schematic diagram of the facility for ion bombardment of organisms at the Institute of Plasma Physics, Chinese Academy of Sciences: (1) ion beam; (2) main chamber; (3) small chamber; (4) rotating wheel for loading crop seeds; (5) main vacuum system; (6) pre-pump for small chamber; (7) isolating valve. Reprinted with permission from [216]. Copyright 2004 by Elsevier.

temperature at the cell surface will be less than −100 °C according to the phase diagram of water. Thus, cells begin to freeze from the surface upon evacuation and an ice shell is formed. Although the ice shell surface can in theory prevent more water from evaporation, it has been observed in experiments that after cells have been pumped for 20 min, the entire cell pellet is transformed into icy dusts. It is also reasonable that all the ice in the cells will be evaporated eventually.

The temperature profile has been investigated by monitoring the cell temperature with time. As shown in Fig. 21, the cell temperature decreases gradually from room temperature to near 0 °C when the pressure goes down from 1 atm to 1000 Pa (pre-pumping in the small chamber for ∼12 s). After the isolation valve is opened, the cell temperature drops to −28 °C in about 100 s as the pressure diminishes from 1000 to 100 Pa. When the pressure continues to decrease, the temperature fall becomes slower implying either complete dehydration or a frozen ice solid. This rapid cooling rate and low temperature deactivate the cells.

The poor vacuum tolerance of living cells and animals indeed presents a big obstacle to ion beam biologists. It is thus important to find means to mitigate the effects. Some preliminary investigations have been conducted to study the vacuum compatibility of mammalian A_L cells and the nematode *C. elegans*. The survival fractions of A_L cells that have been protected by different means have been measured after 120–150 s exposure in a $(2–5) \times 10^{-2}$ Pa vacuum chamber using a flow cytometry assay. A set of ''glycerol and freezing, then vacuum'' protocols have been tested, and it is found that the higher glycerol concentrations (15% and 20%) have better cell protection effects against vacuum stress, and pretreatment with 20% glycerol dramatically increases the cell survival rate from less than 1% to ∼12.7%.

C. elegans is a small soil nematode which feeds on bacteria and is found worldwide. They are easy to maintain and handle in the laboratory and have a reproductive cycle of about 3 days at room temperature. They exist in two sexual states, hermaphrodite and male. As a result, many genetic manipulations that are difficult in mice or even fruit flies can be easily implemented in *C. elegans*. As an ideal model animal with a well understood anatomy and fully sequenced genome, research on *C. elegans* has been quite prevalent. To study *C. elegans* by ion beams and also to learn about its vacuum resistance, glycerol is again used as a protector against vacuum and the results are shown in Fig. 22. A survival rate of 40.4 ± 15.35% (Bar B3) has been obtained by a two-step glycerol protocol, proving that the worm is a promising animal for ion beam biological study.

3.2.1.3. Dehydration and survival of plant tissues in vacuum. Dehydration occurring when water-rich plant tissues are placed in vacuum, as a function of exposure time, has been quantified by mass loss measurements, SEM, and AFM. The response of single-layer onion skin peels, *Curcuma* embryos, and many other plant species to vacuum stress have been

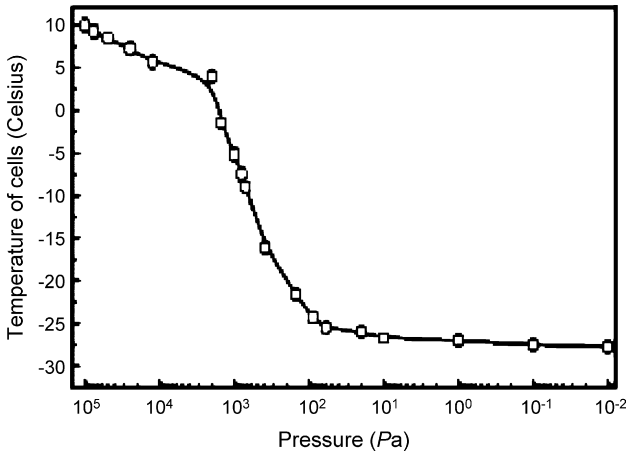

Fig. 21. Temperature profile of cells during evacuation with the temperatures measured inside the cell pellet recorded during pumpdown. Reprinted with permission from [216]. Copyright 2004 by Elsevier.

studied and other issues such as morphological characteristics and growth potentials have also been investigated. Although there is a certain level of errors in mass loss measurements due to the rapid re-hydration during evacuation, it has been found that the mass loss due to water evaporation in vacuum is substantial indeed. Even for a short time like 15 min or less, the mass loss in vacuum is approximately 85%, and no more loss can be detected after further baking at 80 °C for 5 h. This value does not increase appreciably even for additional pumping time up to several hours. Thus, thin plant tissues are fully dehydrated under vacuum conditions when ion bombardment experiments are performed [218].

The morphological changes on onion skin cell walls after subjecting to vacuum for different periods of time have been monitored by AFM and typical micrographs are depicted in Fig. 23. The development of grooves is clearly observed and the measured surface roughness increases markedly with vacuum exposure time [219]. Fig. 24 shows the SEM micrographs of fresh and vacuum-treated *Curcuma* embryo cells. The fresh embryo cells are compact and full of inner cellular contents that can support the skeleton structure and the magnified image shows a surface morphology

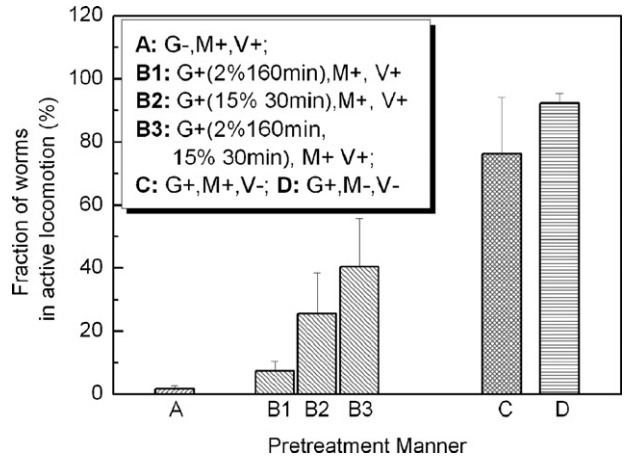

Fig. 22. Survival fractions of *C. elegans* after vacuum exposure. Three glycerol pretreatment protocols (B1, B2 and B3) were compared for their protective abilities against vacuum stress on worms. (A) Negative control worms showing poor vacuum survivability without protective treatment. (B) Vacuum survival fractions of worms with three kinds of pretreatments: 2% glycerol for 160 min alone (B1), 15% glycerol for 30 min alone (B2), and 2% glycerol for 160 min, then changed to 15% glycerol for another 30 min (B3). After glycerol incubation, worms were spread onto Millipore membrane for the subsequent vacuum exposure. (C) Worms treated with glycerol (same steps with B3) and spread onto the membrane (same as in group B), but without vacuum exposure. (D) Worms treated with glycerol (same as B3) alone, without membrane spreading and vacuum exposure. G±, M±, V± stand for with/without glycerol pretreatment, membrane spreading, and vacuum exposure, respectively. The bars represent the means of more than five independent experiments in groups A, C and D. In group B, the data are averaged from 20 to 30 independent experiments. Error bars represent the standard deviations [217].

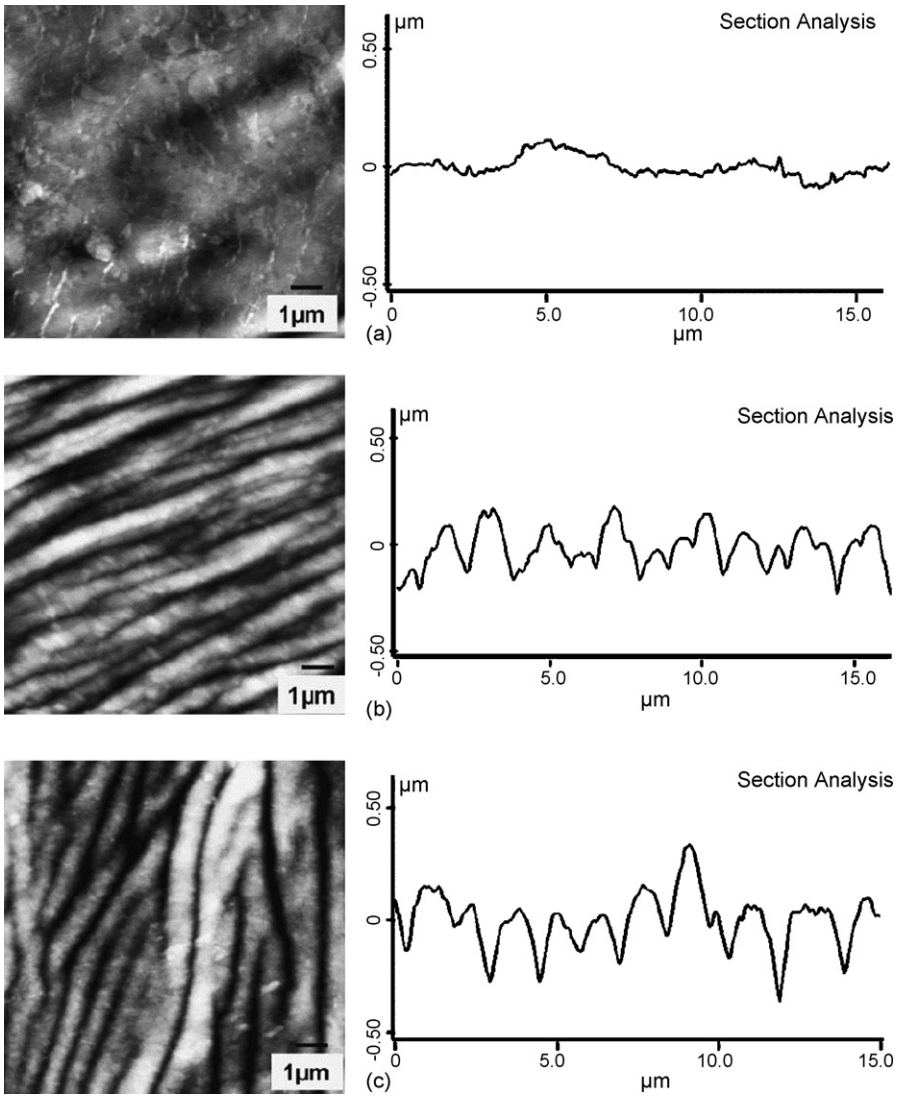

Fig. 23. AFM images of onion skin surface, and section analysis showing surface roughness: (a) after 1 min exposure to vacuum, (b) after 1 h exposure to vacuum and (c) after 12 h exposure to vacuum. Reprinted with permission from [219]. Copyright 2005 by Elsevier.

with uniform grooves. After vacuum exposure, although the structure remains intact, significant shrinkage due to release of inside gas and evaporation of moisture can be observed [220]. Nevertheless, it has also been noted that after post-hydration for 30 min, the vacuum-stressed embryos as well as some other plant species can recover to restore growth, even though subsequent growth is slower in terms of the average seedling heights (Fig. 25) [221].

3.2.2. Single particle beam [1]

Since the late 1980s, there have been renewed interests in developing and applying single-ion microbeam (SIM) techniques [222] to study problems in radiation biology [34,223–226]. One such study is on cell and tissue damage caused by ionizing radiation. In this section, SIM instrumentation germane to this area is described.

A SIM instrument consists of an electrostatic accelerator, deflection magnets, beam regulators, quadrupoles, electrostatic deflectors, diaphragms, collimators, and so on. The IPP (Institute of Plasma Physics) SIM at the Key Laboratory of Ion Beam Bioengineering, Chinese Academy of Sciences is depicted in Fig. 26. It consists of a CN-5.5 Van de Graff accelerator that is able to accelerate singly- or doubly-charged particles produced by a radio-frequency ion source to a maximum voltage of 5.5 MV. The accelerated particles with the desired mass and energy are selected

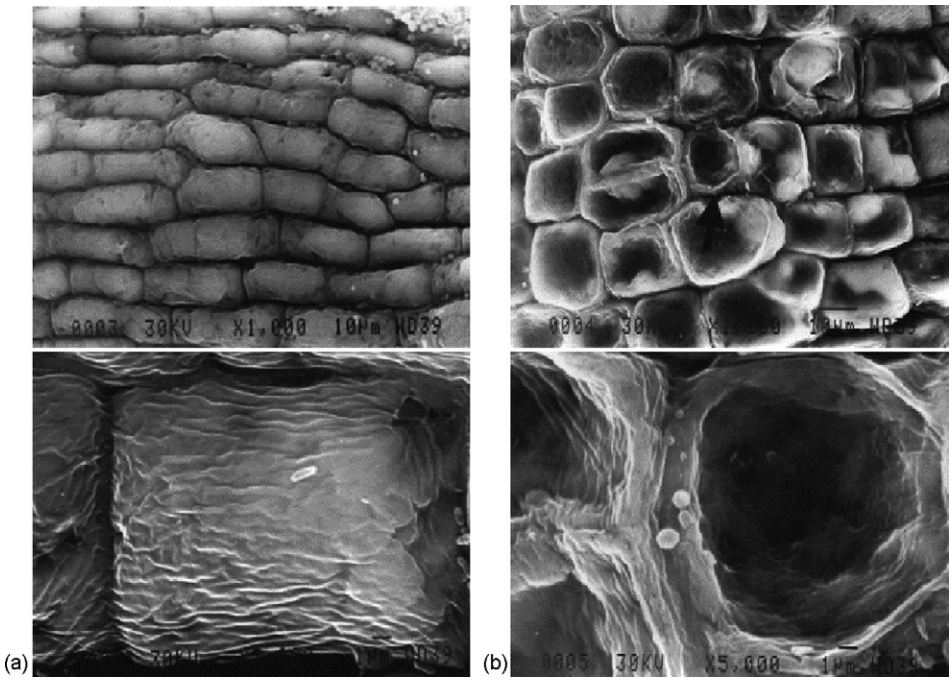

Fig. 24. SEM photographs of an example of the vacuum effect of water loss from *Curcuma* embryo cells: (a) fresh control and (b) vacuum treated (10^{-3} Pa, 2 h), in different magnifications. Scale: width of each photograph in the upper row is 110 μm, and that in the lower row is 22 μm. Reprinted with permission from [220]. Copyright 2003 by the Science Society of Thailand under Royal Patronage.

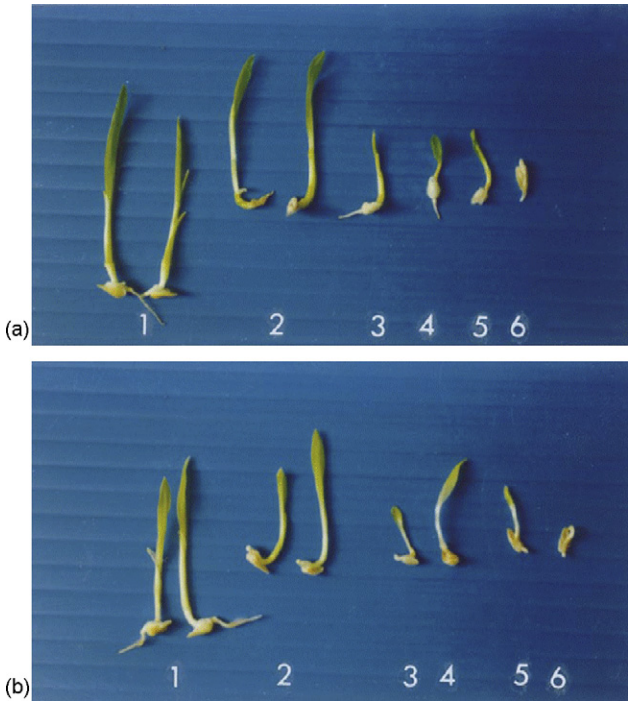

Fig. 25. Naked corn embryos grown in tissue culture after ion implantation. (a) 15 keV N^+ implanted; (b) 30 keV N^+ implanted. (1) Fresh control; (2) vacuum-treated control; (3) 5×10^{14} ions/cm^2; (4) 1×10^{15} ions/cm^2; (5) 2×10^{15} ions/cm^2; (6) 1×10^{16} ions/cm^2. The height of the fresh control is approximately 7 cm. Reprinted with permission from [221]. Copyright 2000 by Elsevier.

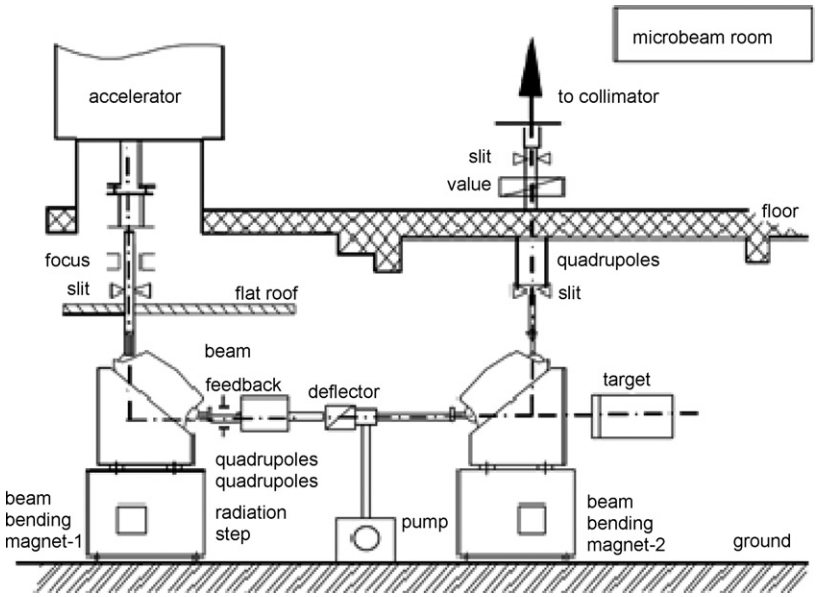

Fig. 26. Schematic diagram of the ASIPP microbeam line [243].

using a magnet which also bends the vertical particle beam to a horizontal beam line. The beam profile and trajectory are further adjusted with slits, beam feedback, quadrupole magnets, and electrostatic collimators along the acceleration column. The horizontal beam line transports the particles into the second magnet which bends the beam vertically to the sample chamber through slits.

SIM, as a new mutation source, is uniquely capable of delivering precisely a predefined number of charged particles (precise doses of radiation) to individual cells or subcelluar targets *in situ* covering an area with a diameter of a few micrometers or smaller. In order to reduce the beam size to the micrometer scale, two methods can be adopted, namely magnetic focusing and collimation. Both have advantages and disadvantages. The former technique can offer a finer beam and better defined linear energy transfer (LET) because no particles are scattered inside a collimator [222,227,228]. In addition, there is more space to install a detector before the target and a higher throughput can be achieved since the beam can be deflected to the cells instead of moving the cells to the beam exit. However, this configuration poses more technological challenge because the focused beam will have to pass through a vacuum window and the cost of installation is considerably higher than that of installing a collimator. The collimator approach has several other advantages. There is greater flexibility with regard to the overall configuration of the beam line. This is important for it is desirable to operate a wet-cell irradiation system vertically. Furthermore, collimation offers a straightforward method to reduce the dose rates to radiobiological levels. Regardless of the methods, the three important criteria are high accuracy of targeting, precise control of the number of charged particles delivered, and high sample throughput.

A glass capillary collimator is adopted in the IPP microbeam instrument to produce a fine beam. A 1 mm long capillary with an internal diameter as small as 1 μm is fitted inside a hole that is machined by spark erosion of a 2.1 mm thick stainless steel disk. A 3 μm thick Mylar film is used as a vacuum window. A 7 μm thick aluminum foil and an 18 μm thick scintillator are sandwiched by another 3 μm thick Mylar film. The number of emitted photons and energy consumption depend on the type and energy of the traversing particle as well as the total thickness of the thin films used. The number of near-monoenergetic photons emitted is 10^4/s when a 2–3 MeV proton beam passes through the collimator in this configuration. A typical energy spectrum acquired from the aligned SIM is shown in Fig. 27. In practice, the particle number depends on the geometry and coupling arrangement of the detector, quantum efficiency of the detector, as well as other factors such as losses due to scattering.

In order to achieve high precision and high accuracy with respect to the number of particles delivered to the targets, the conditions must be well defined. In addition, iterative control of the instrumental parameters and feedback is necessary during the experiments. The integrated control system can be divided into three modules: image acquisition and processing, microscope stage control, and particle counter and beam shutter. The cells to be irradiated are first

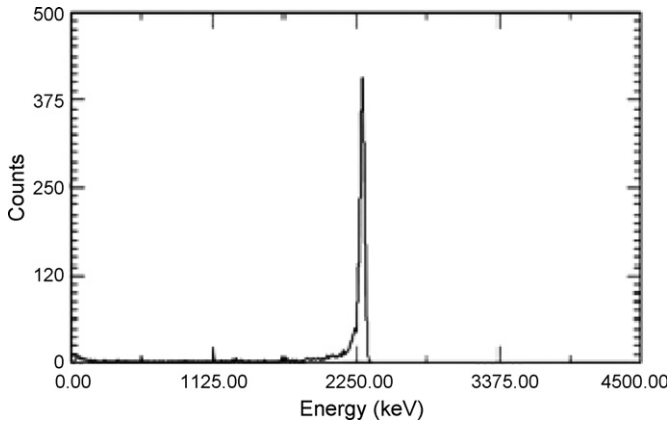

Fig. 27. Spectrum of 2.2 MeV monoenergetic protons (after passage through the vacuum window and scintillator collimated by a glass capillary collimator with 1.0 μm diameter and 0.98 mm length [243].

stained and attached to a Mylar-film-bottomed dish. The light spot produced when emitted particles excite the scintillator can be used as an optical reference to localize the position of the exit aperture. The nucleus of each cell is identified and located by a computer/microscope-based image analysis system which detects the fluorescent pattern of the cells by UV light. Afterwards, the dish is moved by computer control under the beam where the first cell nucleus is positioned. The ability to deliver a single or preset number of particles to each cell depends critically on the detector and beam shutter. During irradiation, the charged particles are detected after passing through the cell. The beam shutter is a fast electrostatic deflection system allowing each irradiated nucleus to be quickly removed from the beam when enough particles have been detected. The beam shutter is opened until the required number of particles has passed though the nucleus. Afterwards, the shutter is closed and then the next cell is positioned under the beam.

There are currently more than 14 SIMs worldwide [229–245] and there is a growing number of laboratories installing SIMs or with plans to do so. Several SIMs are used routinely in radiobiology and their specifications are summarized in Table 3, but it should be noted that their capabilities change constantly. Research on SIMs has recently focused on the low-dose effects, cell signaling, genomic instability, bystander effects and adaptive responses. The list of possible applications of SIM in radiobiology continues to grow and diversify. Scientists are no longer only interested in targeting nucleus or cytoplasm, and cell organelles and tissues are becoming the next targets. The hardware in SIMs is undergoing constant development and much progress has in fact been made in the past few years. For example, a laser ion source (LIS) enables the use of ions from hydrogen to iron to provide a wider range of LET [245,246]. Other aspects of SIM that has received attention include larger cell throughput, improved target accuracy, enhanced penetration of the irradiation, and application of non-UV methods for target visualization. The throughput of the SIM needs to be further improved because a large number of samples must be processed in order to obtain meaningful statistics. For instance, the expression of genes must be derived from a large population involving millions of cells. Moreover, combination of pre-cell detection and post-cell detection may be the only way to eliminate the possibility of over-counting or under-counting.

Although SIM is a powerful tool in radiobiology, some new technologies are needed. Since visual observation of cells and particle detection occur simultaneously, the lucite light guide technique provides an elegant solution. Many optical screening technologies are also useful. High throughput screening (HTS) is a considerable challenge to both instrumental design and automated data handling and evaluation, especially miniaturized HTS and ultra-HTS (uHTS) at ambient temperature. It is important to be able to conduct *in situ* physiologically monitoring of cells or tissues in a noninvasive way [247]. In this way, scientists can investigate the original process of the interaction between low-energy ions and organisms rather than the endpoints in order to gain more insights. Fortunately, biologists and biophysicists are now joining forces to bring major advances in the art of SIM and significant progress is anticipated in the near future.

3.3. Charge exchange between incident ions and organism surfaces [1]

The surface of a biological sample such as a cell contains negative ion groups that move to the anode during electrophoresis in a neutral electrolyte. During ion radiation, the damage changes the number of these negative ion

Table 3
SIMs worldwide in routine use and their current main specifications [1]

Institution	SIM	Accelerator	Particles	Energy/LET	Mode of detection	Targeting accuracy	Through-put
RARAF, Columbia University, USA	RARAF micro-beam	4.2 MeV Van de Graff accelerator	From hydrogen to iron	10–4500 keV/μm	Gas-filled ionization chamber and a SSD detector	∼±2 μm	∼11,000 cells/h
CRC Gray Laboratory, Northwood, UK	GCI micro-beam	4 MeV Van de Graaff accelerator	Protons, helium ions	5.7 MeV He^3	Scintillator + PMT	<±2 μm	∼36,000 cells/h
JAERI-Takasaki, Japan	TIARA micro-beam	AVF-cyclotron accelerator	From C ions to Fe ions	8–1800 keV/μm	a CaF2 (Eu) scintillator + PMT	∼±1 μm	>60,000 cells/h
CENBG, Bordeaux, France	CENBG micro-beam	4MeV Van de Graaff accelerator	Protons, helium ions	3.5 MeV alpha or proton	a thin scintillating foil + gas transmission detector	±2 μm	>2000 cells/h
PTB, Braunsch-weig, Germany	PTB micro-beam	3.75 MeV Van de Graaff and 20–35 MeV cyclotron accelerators	Protons, helium ions	3–200 keV/μm	Scintillator + PMT	±1.5 μm	15,000 cells/day
NIRS, Chiba, Japan	SPICE micro-beam	HVEE Tandem accelerator	Protons, helium ions	3.4 MeV H^+, 5.1 MeV He^{2+}	Scintillator + PMT	<±2 μm	2000 cells/h
University of Melbourne, Parkville, Australia	MARC Micro-beam	5U NEC Pelletron accelerator	Protons, helium ions, C, N, O	4.6–7.7 MeV alpha particles	Boron doped thin diamond film + SSD + CEM detector	≤±300 nm	>3000 cells/h
IPP, CAS, Hefei, China	CAS-LIBB micro-beam	5.5 MV Van de Graaff accelerator	$^1H^+$, $^2H^+$	3.5 MeV H^+, 3.5 MeV $^2H^+$	Scintillator + PMT	∼±1 μm	–
MIT LABA, Boston, USA	MIT LABA micro-beam	1.5 MV single stage electrostatic accelerator	He^{2+}, H^+, He^+	15–30 keV/μm	Light guide + plastic scintillator + PMTs	∼±3 μm	–
GSI, Darmstadt, Germany	SIHF micro-beam	GSI linear accelerator (UNILAC)	From carbon to uranium	1.4 MeV/μm to 11.4 MeV/μm	Si_3N_4 foil + channeltron	<±1 μm	–
Technische Universität München, Germany	SNAKE micro-beam	14 MV Munich Tandem accelerator	From protons to uranium	2 keV/μm to several MeV/μm	Position-sensitive detector (PSD)	∼±700 nm	–
University of Leipzig, Leipzig, Germany	LIPSION micro-beam	3.5 MV Singletron™ accelerator	Protons, helium ions	10–20 keV/μm	Multi-dectector	∼±130 nm	–
WERC, Japan	W-MAST micro-beam	5 MV tandem accelerator	Protons	10 MeV proton	Si surface-barrier detector (SSD)	∼±10 μm	–
INFN-LNL, Padova, Italy	INFN micro-beam	7MeV Van de Graaff CN accelerator	$^1H^+$, $^2H^+$, $^3He^{2+}$, $^4He^{2+}$	7–150 keV/μm	Silicon detector	–	–

groups via dissociation and topographical rearrangement on the surface. In addition to energy deposition that damage the ion groups, charge exchange between the implanted ions and surface molecules also changes the electrical characteristics of the sample.

As the incident ion loses energy traversing the target material, every collision with target atoms has a certain probability of losing or adding electrons. This phenomenon is termed the charge exchange effect [248,249]. If the ion has a charge state i before the collision and f after the collision, the reaction cross section for loss or capture of electrons is σ_{if} which is strongly dependent on the incident ion velocity and charge number, but almost independent of the charge number of the target material [250,251]. When the incident ion has a velocity much greater than the electron orbital velocity, a collision between the ion and target atoms will rapidly strip electrons exposing the nucleus. In this case, the probability of the ion capturing another electron is much smaller, and even if it does happen, the new electron will be lost easily during the next collision. After many collisions, the ion loses its kinetic energy, and when its velocity is close to the orbital velocity of the electron that is to be captured, the capture probability increases while the electron loss probability decreases. The orbital velocities of the electrons of an ion decrease from the inner shells to the outer shells. When the ion velocity gradually diminishes to velocities corresponding to those of the electrons in each shell, the ion continuously captures electrons in succession. Finally, when the ion velocity decreases to less than the velocity of the electrons in the outermost shell, the incident ion is neutralized. At this point, it loses energy mainly by collisions with target nuclei (i.e. nuclear stopping dominant), and very little energy is transferred to the target electrons. When the neutralized particle slows to thermal velocity, it either combines with the target atoms to form a compound or becomes embedded in the target as an interstitial. For a hydrogen ion (proton), the charge exchange reaction can be expressed as

$$H^+ + e^- \Leftrightarrow H^0. \tag{1}$$

The cross section of a single electron capture is maximized at an incident proton energy of 25 keV and falls off as the primary H^+ energy increases [122].

Taking σ_{10} as the cross section of electron capture by a H^+ ion, σ_{01} the cross section of electron loss by the fast hydrogen atom, π the target thickness, F_0 the neutralized fraction of the H^+ beam, and F_1 is the part of the fast hydrogen atom beam that loses electrons to become hydrogen ions, we have

$$\frac{dF0}{d\pi} = F_1\sigma_{10} - F_0\sigma_{01} \tag{2}$$

and

$$F_1 = 1 - F_0. \tag{3}$$

Combining Eqs. (2) and (3) gives:

$$\frac{dF_0}{d\pi} = \sigma_{10} - F_0(\sigma_{10} + \sigma_{01}), \tag{4}$$

and the solution is

$$F_0 = \frac{\sigma_{10}}{\sigma_{10} + \sigma_{01}}\{1 - \exp[-\pi(\sigma_{10} + \sigma_{01})]\}. \tag{5}$$

When $\pi \to \infty$, we have

$$F_{0\infty} = \frac{\sigma_{10}}{\sigma_{10} + \sigma_{01}} \tag{6}$$

and

$$F_{1\infty} = \frac{\sigma_{01}}{\sigma_{10} + \sigma_{01}} \tag{7}$$

For a 25 keV hydrogen ion, the maximum neutralization efficiency is 80%. The target thickness is the area density of the target. When the target thickness is 1×10^{16} atoms/cm^2, the neutralization efficiency is 95% of the maximum efficiency. This indicates that after a 25 keV H^+ ion penetrates just 1–2 atomic layers, it can already reach a balance in neutralization efficiency.

When positive ions are implanted into biological organisms, molecular groups in the top 1–2 single atomic layers of the target surface lose electrons due to the charge exchange effects and become neutral or positive ion groups. If the ions are singly charged, the implantation fluence is D, and the neutralization efficiency is F_0, the accumulated charge per unit area on the surface is

$$q = \frac{D \cdot F_o}{(6.25 \times 10^{18})} (\text{Coulomb/cm}^2). \tag{8}$$

For example, for an H^+ implantation fluence of $D = 5 \times 10^{14}$ ions/cm^2 and neutralization efficiency $F_0 = 80\%$, $q = 6.4 \times 10^{-5}$ C/cm^2.

Since biological organisms are typically not good electrical conductors, the accumulated charges cannot be dissipated easily. Hence, the charges may be maintained for a long enough time to change the electrical characteristics of the sample that can be monitored by a capillary-electrophoresis method. Fig. 28 shows the electrophoresis behavior in the capillaries of tyrosine (Tyr) crystals after ion implantation [252]. The natural Tyr molecular crystal is electronegative and moves to the anode during electrophoresis, but after implantation of positive ions, the rate of the movement decreases. When the ion fluence reaches a critical value, the mobility is close to zero and when the fluence increases further, Tyr moves to the cathode.

Common cells are electrically negative, and when positive ions are implanted into them, their electrical characteristics change with the fluence. Interactions between energetic ions and a solid surface can cause surface secondary electron emission, which can accelerate changes in the electrical characteristics of the organism surfaces. Charge accumulation on the cellular surface perturbs the electrostatic field across the membrane. It is well known that the totality of a biosystem can be broken down conceptually into individual biological cells. The cell itself is partitioned internally by membranes that limit material diffusion between smaller compartments inside the cell. Inside a living cell, water, ions, neutral solutes, metabolites, and dissolved gas continuously exchange across the membranes in different ways. Some diffuse inward in the cells in the direction of decreasing potential gradient. This is the biological equivalent of the thermodynamic transport of heat from a warmer body to a cooler body. Other substances, however, can be accumulated in the cell in a direction opposite to the potential gradient. Their motion into the cell interior, being against the potential gradient, must consume energy. If a potential difference is established across the membrane, this may form an uphill driving force for these ions. The production and maintenance of the potential difference across the membrane is closely related to the concentrations of positive and negative ions within the cells. Once the field across the membrane is altered by charge exchange, the normal activities of the living cells such as material transport, energy transformation, information exchange, and control of metabolism may not be maintained. It has recently been suggested that charge exchange can generate damage in DNA molecules by changing the stability of DNA building molecules and charge homeostasis [253,254].

3.4. Sputtering and surface damage of plant cell wall material

Surface etching is a complicated physicochemical phenomenon caused by energetic incident ions. Sputtering, a subset of etching, is caused by momentum transfer from the impinging ions to the target atoms causing ejection of the target atoms from the surface. The sputtered species can be neutrals, atomic ions, and molecular ions [255]. Etching and sputtering are widely used in the industry, especially coatings and semiconductors, to physically or chemically

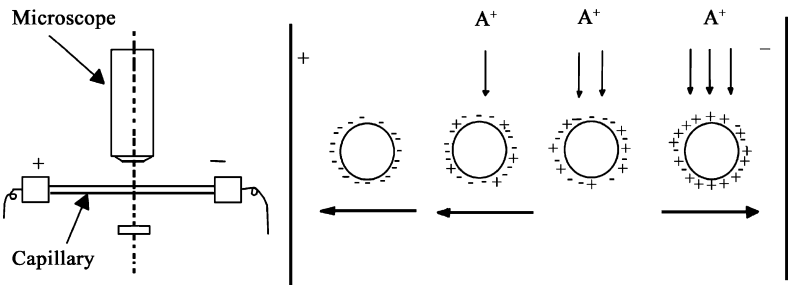

Fig. 28. Schematic of electrophoresis (left) and mode of change in electric characteristic of Tyr (right).

remove materials or for surface cleaning purposes. Sputtering is fairly well understood for metals and simple semiconductors, but not as well understood for complicated molecules and insulators such as organic and biological molecules. Here, we focus our attention on etching and sputtering of biological materials and the differences with those of metals and semiconductors.

Surface etching of plant material plays an important role since the discovery of biological effects in crop seeds induced by ion implantation [80]. The etching effects by 20–30 keV argon or nitrogen ions with a fluence of 3×10^{16} ions/cm^2 on bean cotyledon have been studied. The following observations are made:

(1) All of the cell walls that face the ion beam are thinned and a few cells are even cut in half leaving an ordered traumatic surface.
(2) Cell erosion is substantial as manifested by deep holes and grooves.
(3) The sputtered species consist of not only single atoms or molecules but also biological macromolecules and cell debris.
(4) The sputtered thickness is 100–200 nm which is much larger than the value of 6 nm calculated by classical simulation program for cell wall material [256].

Therefore, although accurate simulation models and programs are available for metals and semiconductors, theoretic calculation of the sputtering yields of cell walls is much more difficult partly due to the lack of a broad database for complex organic molecules and organisms.

Considering that a plant cell wall structure comprises microfibril bunches of cellulose with a chemical structure $C_6H_{12}O_6$, the cell wall can be modeled using partial mass densities and surface binding energies. These values can be entered into the simulation program to derive the sputtering yield. The calculated value which is 9.7 atoms/ion is five times higher than that of 1.97 atoms/ion predicted by simple simulation. For bombardment with 30 keV Ar^+ with a fluence of 2×10^{15} ions/cm^2, the estimated sputtering loss based on the calculated sputtering yield is approximately 55 nm that differs significantly from the value of 11 nm generated by the simple PROFILE simulation program [218].

The calculated results are corroborated by transmission electron microscopy (TEM) measurements of the cross section of *Curcuma* embryo cell walls after bombardment by 30 keV Ar^+ [220]. In comparison with the smooth surface of the unsputtered control cell surface, large areas of bombardment-induced damage are observed on the external surface of the cell walls and the damage becomes more severe at higher ion fluences (Fig. 29). In these damaged areas, the sputtered thickness ranges from a few tens of nanometers to approximately 100 nm. The consequence of severe sputtering is that the cell envelop can be significantly thinned by the ion beam. If the ion flunece and energy are carefully controlled, the ion beam can be used for precise sputtering and thinning of cell walls to expose the inner

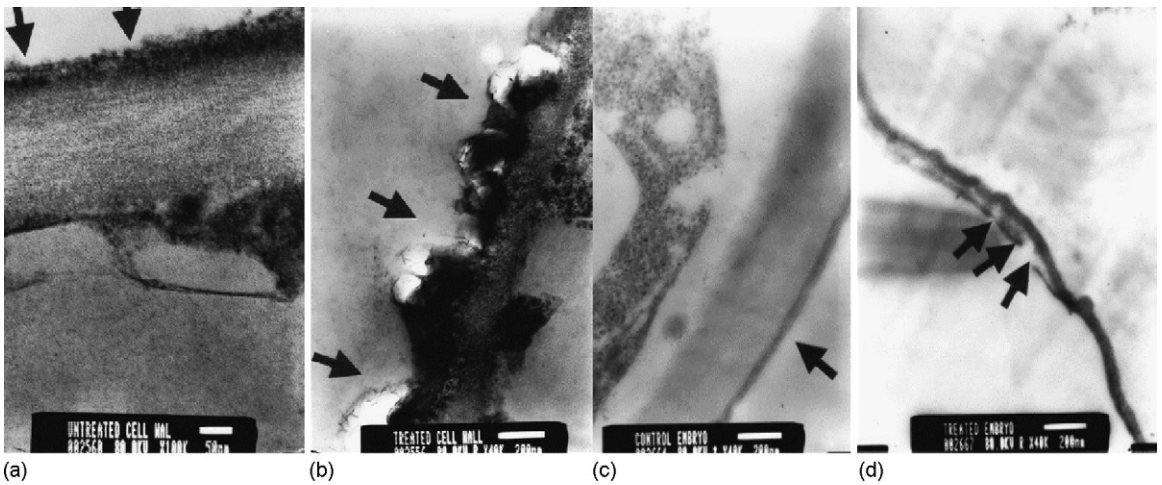

Fig. 29. TEM micrographs of the *Curcuma* embryo cell envelopes of (a) the vacuum-treated control, (b) the Ar^+-bombarded (30 keV, 2×10^{15} ions/cm^2) cell, (c) the vacuum-treated control, and (d) the Ar^+-bombarded (30 keV, 1×10^{15} ions/cm^2) cell. The arrows indicate the outside of the cell envelope. The scales are as indicated by the bars in the photographs. Reprinted with permission from [220]. Copyright 2003 by the Science Society of Thailand under Royal Patronage.

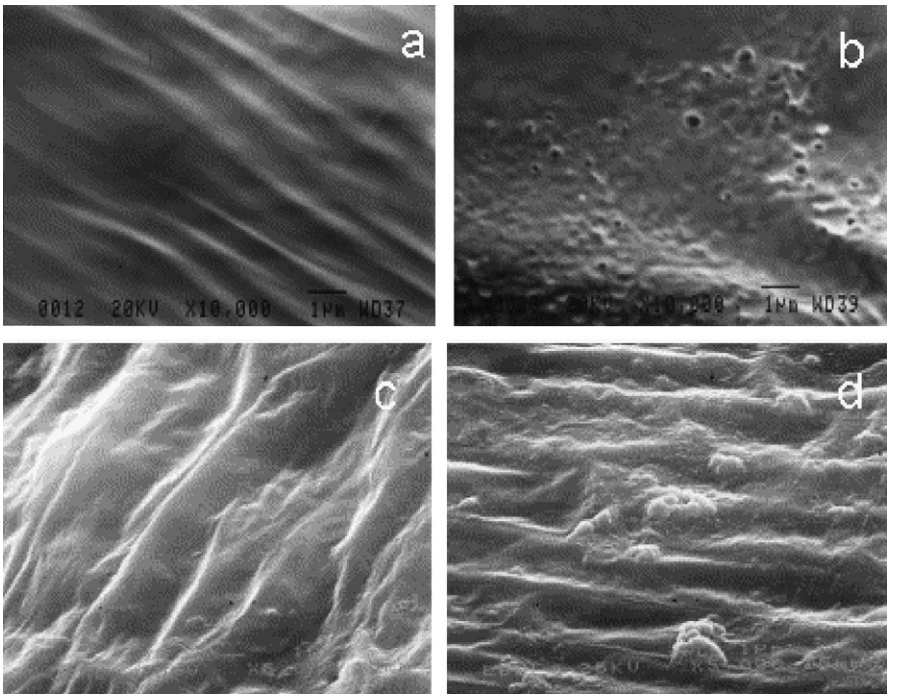

Fig. 30. SEM micrographs of the plant cell surfaces. Ion bombardment conditions: 30 keV Ar^+ at a fluence of 1×10^{15} ion/cm^2. (a) Onion cell surfaces (unbombarded control); (b) ion-bombarded onion cell surfaces; (c) onion cell surfaces at high resolution (unbombarded control); (d) ion-bombarded onion cell surfaces at high resolution, at glancing angle. Scales: the length of the photographs of (a) and (b) is 12 μm, (c) and (d) 20 μm. Reprinted with permission from [218]. Copyright 2002 by Elsevier.

cellular structures for subsequent analysis [257]. Other studies that can be performed on the thinned cells include ion beam assisted macromolecule transfer and DNA packaging mechanism inside virus [258].

An important phenomenon observed in ion beam bombardment of plant cell wall surface is that etching and sputtering are not homogeneous, as shown in Fig. 29 and the micro-craters depicted in Fig. 30 [218]. These micro-craters are not distributed uniformly and emerge after bombardment by a variety of gaseous and metal ions such as Mg, Xe, Ar, and Cl. They also depend on the ion fluences in the range of (1–2.5) $\times 10^{15}$ ions/cm^2 [219,259]. AFM reveals that the size of the corroded pits or holes on the surface of living cellular material is of the cellular scale with diameters of 50–100 nm and the thickness of the sputtered layer is about several hundred nanometers for 20 keV, 10^{15} to 10^{16} Ar^+/cm^2. Similar damage has been reported in ion implanted wheat (*Triticum aestiíum* L.) embryo cells and severe cell wall damage and even cytoplasm bulging are evident after high fluence irradiation. In contrast, this degree of damage is not found on evacuated (Fig. 30a) or electron-beam-irradiated plant cell envelops, nor on the ion bombarded equivalent material, cellulose, that has a similar chemical composition as plant cell wall material [259,260]. These results rule out the possibility that the formation of these micro-craters is a simple consequence of rapid water evaporation during ion bombardment or power or energy deposition into the cell wall, since electron bombardment also dumps a lot of energy into the material similar to ion beam. In general, the etching rate in cells is 10^3 to 10^4 times greater than those in metals or semiconductors and the sputtering yields in cells are two to four orders of magnitude higher than those of conventional materials.

3.5. Ion penetration profile in botanic samples

SRIM calculation that simulates the penetration profile of 30 keV N^+ into organisms with homogeneous structures has been presented in Section 3.1. Based on the simulation results, the range of 30 keV ions is less than 1 μm in biological material (Fig. 19b), whereas the average thickness of rice embryo coat is 40–60 μm. This huge discrepancy fails to explain the observed mutagenic effects when ion implantation is conducted in crop seeds, and therefore, more thorough investigations are needed.

The assumption of a continuous, homogeneous distribution of the atomic volume density that is much larger than the ion range is practically not applicable here as biological material is not ideal. Unlike metals and semiconductors in which defects are describable to the atomic scale thereby enabling accurate theoretical derivation of ion trajectories, living cellular material is much more complicated. First of all, biological samples contain many elements, including essential minerals. Since the stopping power of the target atoms depends on the atomic number of the target atom, the stopping power of a biological specimen containing multiple elements is the concentration average of all the elements. Secondly, the elements in organisms are distributed heterogeneously (please refer Section 3.1). Thirdly, similar to crystalline solids, channels or holes exist in biological specimens as shown in Fig. 31 [261] and traversing ions can penetrate these channels readily. For low-energy ion implantation, the dimensions of these holes or channels can be even greater than the ion range. Hence, it is natural to expect that the ion penetration is much larger in biological specimens.

Exact knowledge of the range distribution of keV heavy ions in plant material is necessary to carry out ion beam mutation and breeding of crops. The range distribution of ions entering the medium is determined by the statistical nature of energy deposition and angular scattering. For ion–solid collisions, the range distributions are normally calculated based on the framework of transport theory. Experimental measurements of ion ranges typically include two parts, implantation of ions into the stopping medium and determination of the position of the implanted ions. Direct measurements of the implanted ion distributions can be performed by Rutherford backscattering spectrometry (RBS), nuclear reaction analysis, particle induced X-rays emission (PIXE), energy dispersive analysis of X-ray (EDAX), positron annihilation technique (PAT), mass spectrometry, and chemical etching. Indirect approaches are available also, and examples are investigation of the transmission geometry in which ions that penetrate thin layers of matter are recorded by a detector system [5,13]. In order to elucidate the mechanism of ion beam induced mutation, the depth profile of low-energy ions in botanic samples must be known and various measurement approaches with different sensitivities have been attempted.

3.5.1. Structural characteristics of botanic material by transmission spectrum measurements

Transmission spectrum measurements can disclose the abnormally deep penetration of keV ions in botanic samples. A series of transmission energy spectra acquired by MeV proton, He^+, F^+ and α particle (from ^{241}Am at 5.484 MeV) irradiation of tomato and onion skin cell walls and 50–100 μm thick bean slices before and after keV ion implantation can provide useful information about ion penetration and thinning/radiation damage effects of low energy ion sputtering of the organism. Fig. 32 shows the α-particle transmission energy spectra obtained from a piece of 50 μm thick tomato skin before and after 30 keV, 1×10^{17} N^+/cm^2 bombardment. Before ion bombardment, the

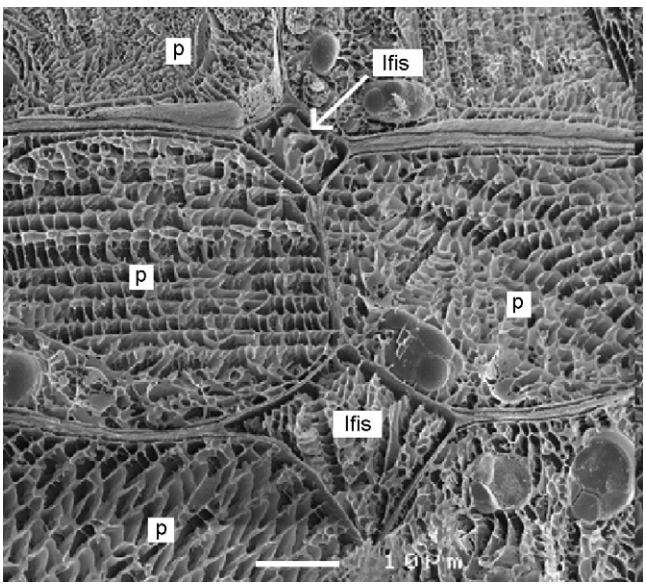

Fig. 31. Cryo-SEM micrograph showing pea seed coat parenchyma cells (p) with liquid-filled intercellular spaces (lfis). The cavity structures in micrometer scales are visible. The bar represents 10 μm. Reprinted with permission from [261]. Copyright 2003 by Oxford University Press.

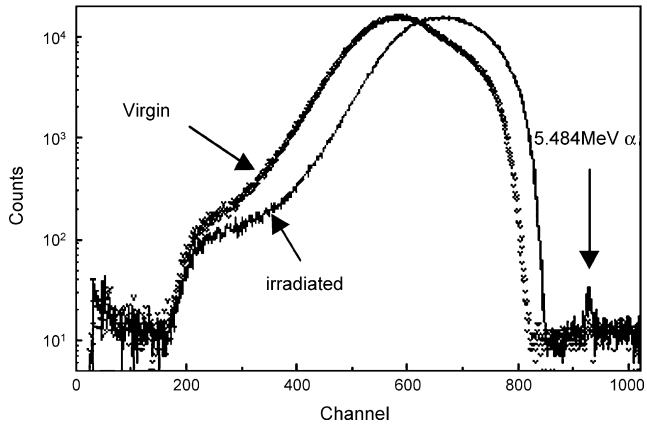

Fig. 32. Alpha particle transmission energy spectrum of tomato fruit skin after N^+ irradiation to a fluence of 1×10^{17} ions/cm^2 [1,262].

energy spectrum has a very broad pattern, indicating a heterogeneous distribution of the spatial structures in the tomato skin. This broad spectrum is equivalent to the superposition of the energy spectra of a Mylar film (a bio-equivalent material with chemical formula $C_{10}H_8O_4$) with an α-particle transmission thickness of 11–20 μm. In irradiation terms, tomato skins are not as thick as they appear visually due to pores and voids through which α particles can pass without losing much energy. After ion irradiation, the energy spectrum shifts to the high energy side. The spectral distribution is equivalent to that of a Mylar film with a thickness of 9–17 μm. This indicates that ion beam etching thins the tomato skin by an equivalent of 2–3 μm Mylar film thickness or a tomato skin thickness of 7.5–9.1 μm. Compared to ion beam etching of metal samples, the same parameters will only lead to removal of 10 to several tens of atomic layers. The difference is three orders of magnitude. A completely free α-particle peak can also be observed in the spectrum after ion irradiation with 1×10^{17} ions/cm^2. The free passing α particles constitute approximately 4×10^{-5} of the total transmitted particles. This means that the ion beam can etch away the coat and dig paths that can connect the voids (in a natural situation, they are isolated from each other) in the direction of ion incidence. Thus, later incident ions can penetrate deeper until finally entering the embryo cells. Based on these results, at least two points are clear. Firstly, the mass-thickness is small in living cellular material and secondly, there are open channels in the material allowing deep penetration of the ions without much energy loss [262]. These phenomena are supported by positron annihilation lifetime (PAL) data acquired from peanut samples implanted with 100 keV N^+ and 200 keV V^+ ions [263].

In addition to α-particle transmission measurement of tomato skins, the transmission spectra of many other botanic samples have been recorded and analyzed. Examples include 0.5–1 MeV He^+ bombardment of 50–100 μm thick corn seed coat, grape skin, and tomato skin [264], low-current 2.5 MeV proton and 2.2 MeV H^+ bombardment of single, double, and triple layers of onion endocuticle samples together with 38 μm thick Mylar film and 76 μm thick nylon filter film that has a porous structure [265,266], as well as low current 1–6 MeV F ion implantation into kidney beam coat and onion skin [267]. The average energy losses in the onion endocuticle samples are much smaller than those in polymer films, but the widths of the spectra are quite broad and asymmetric. In other words, some incident ions lose only a very small part of their energy in the endocuticles. The spectrum of the single-layer onion skin can be deconvoluted into two energy loss parts indicating that the sample contains two different mass thicknesses. In contrast to the spectrum of the nylon filter film, the broad energy spectrum of onion endocuticle sample probably results from an inhomogeneous mass density distribution.

The influence of radiation damage on the penetration of energetic ions in botanic samples has been investigated by measuring the dynamic changes in the transmission energy spectra of 100 μm thick kidney bean slice bombarded by 1.5 MeV F^+ [266] and kidney bean coat bombarded by 3 MeV F^{2+} [267]. In the initial phase of ion bombardment, none of the incident ions can penetrate through the sample. After about 500 s of irradiation, more and more transmitted ions are recorded and with increasing ion flux, the energy peak gradually shifts to higher values. This dynamic penetration process is unique for heavy ion bombardment of botanic samples and differs from that in other materials. In fact, when the beam current density is sufficiently high, the irradiation damage in plant coats can be very severe. Obviously, the penetration of energetic heavy ions is deeper with more radiation damage. High-precision weight loss measurements have also shown that the total mass of botanic sample decreases with increasing ion fluence [268].

In summary, transmission spectra measurements provide direct experimental evidence on the characteristic structures of plant samples and the complex interactions between ions and plant material. Energetic ion beams made of several hundred keV He^+ and proton and 1–6 MeV F^+ are able to pass through the thick seed coat and embryo slice that are tens of micrometers thick. Some of the incident ions only lose a small fraction of their initial energy after passing through the samples and the number of transmitted ions/atoms decreases exponentially with higher emerging energy. Botanic samples have very complicated structures, being inhomogeneous in mass distribution and having multi-phases and open paths as seen by the penetrating ions. Radiation damage is apparent and can greatly change the sample structure and reduce the mass thickness. Hence, the actual depth profile of energetic ions in botanic samples cannot be accurately simulated by the conventional LSS theory that utilizes a homogeneous mass density distribution.

3.5.2. STM-HOPG transmission measurement

Based on experimental proof, botanic samples have an inhomogeneous mass density that allows incident ions to penetrate with only slight energy loss. Moreover, radiation damage reduces the mass thickness due to decomposition or sputtering, which subsequent helps ions to traverse an even longer distance. However, it is still very difficult to predict whether keV ions employed in ion beam mutation breeding can actually reach the interior of plant cells. Since the energy of primary incident ions is only tens of keV, the transmitted ions may have very low energy or may be neutralized on the way. Therefore, accurate measurements of the signals using solid barrier detectors, Faraday cup, and normal solid state nuclear track detectors (SSNTDs) such as CR39 may be difficult. To overcome this problem, a highly oriented pyrolytic graphite (HOPG) detector that has atomic scale resolution is often utilized. The isolated damage induced by the bombardment of an energetic ion on the HOPG is observed by STM (scanning tunneling microscopy) and the statistical data are then analyzed. Fig. 33 shows the surface feature of the HOPG covered by 30 μm thick kidney bean slices that are irradiated with 40 keV nitrogen ions with fluences of 3×10^{16} and 3×10^{17} [269]. The density of the slice is about 1.18 g/cm^3. It can be inferred from the STM photo that the damage (protrusions) on the surface of HOPG is related to the fluences. For 30 and 50 μm thick slices, the densities of the protrusions are about $1.0–5.0 \times 10^{11}$ and $0.6–2 \times 10^{10}$ cm^{-2}, respectively, and they are much larger than the number of 2×10^9 protrusions/cm^2 observed on the unimplanted control HOPG sample. In comparison, the number densities measured on the 100 μm bean slice and 8 and 72 μm PET films are about the same as that on the control. Hence, 40 keV N^+ bombardment causes evident damage to a depth of 50 μm in the dry kidney bean seed slices, and the higher the fluence, the more severe is the damage. Similar experiments disclose a ion penetration depth of larger than 60 μm in kidney bean in the case of 100 keV, 5×10^{16} ions/cm^2 Ar^+ implantation, further indicating that the structure of dry crop seeds is inhomogeneous and there exist very thin regions in the botanic slices (from the standpoint of ion penetration). It has been discussed in Section 2 that ions with extremely low energies can lead to fragmentation of biomolecules and even strand breaks (SSB/DSB) in solid plasmid DNA. Therefore it is reasonable that even with

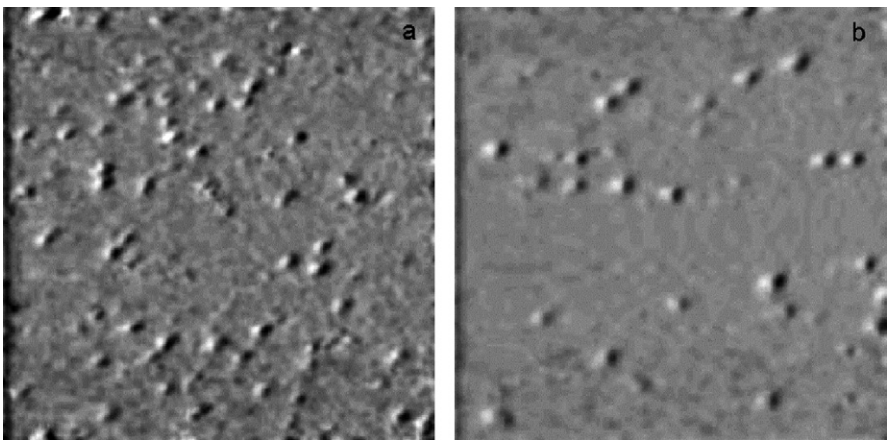

Fig. 33. The typical unit image (100 nm × 100 nm) of HOPG samples irradiated with 40 keV N^+ ions. (a) 30 μm slice irradiated with the fluence of 3.0×10^{17} ions/cm^2 and (b) 30 μm slice irradiated with the fluence of 3.0×10^{16} ions/cm^2. Reprinted with permission from [269]. Copyright 2001 by Elsevier.

attenuated energy after traversing a long distance, the ion beam can still produce damage in DNA molecules in the embryos of dry seeds. This paves the way for mutation breeding of crops by means by ion implantation.

3.5.3. Ion range by ion concentration measurements

In investigations of ion ranges in botanic samples, analytical techniques commonly used for conventional solid materials have been employed to provide direct evidence of the deep penetration of implanted ions. For example, 3.4×10^{17} Ar^+ are implanted at 110 keV into wheat embryos with the coats stripped off. The Rutherford backscattering (RBS) spectrum shows that the nominal ion range is 257 nm but about 6% of the ions are detected to a depth of 692 nm [270]. Similarly, in peanut slices implanted with 200 keV, 9×10^{16} ions/cm V^+, the values determined by RBS are 460 nm and 985 nm, respectively [271]. These data agree with TEM measurements conducted later on onion skin cell walls and thin sections of *Curcuma* embryos [272]. In these cases, the damage range determined by TEM analysis of 30 keV, 2×10^{15} ions/cm^2 Ar^+ implanted onion skin cell walls is 200 nm and that of the *Curcuma* embryo is 450 nm. Although these data are larger than those calculated from the simulation code (40 nm for onion skin and 55 nm for *Curcuma* embryo), they are still much less than the typical thickness of several tens of micrometers of most crop seed coats, and so ion penetration into botanic seeds is doubtful. Based on these data as well as previous calculations and measurements [270], it was once concluded that the range of keV energy ions is too small to pass through the thick seed coat to reach the genetic relevant parts such as the SAM (short apical meristem) that is located about 100 μm below the seed coat in most crop seeds.

As the sensitivities of analytical instruments and methods advance, in contrary to the above RBS results, Fig. 34 shows the vanadium (V) in-depth distribution in peanut seed slices implanted with 200 keV V^+ measured by proton induced x-ray spectrometry (PIXE) and SEM [273]. In these experiments, a dry peanut seed is fixed in a specially made module and put onto a slicer to cut off a part of the seed. The slice is placed in the target chamber with the cut side facing the ion beam and then implantation is conducted. After ion implantation, the sample is packed with paraffin and put onto the slicer again to be cut into 15 μm thick pieces. Each piece is analyzed by PIXE and scanning electron microprobe to determine the V^+ concentration distribution. As shown in Fig. 34, the V peak in the first 0–15 μm is very high and about 98% of vanadium is implanted into this region. In the second slice (16–30 μm), the V concentration is smaller and continues to decrease in subsequent slices. In the region of 121–135 μm, the V concentration is close to the PIXE detecting limit.

Therefore, the damaged areas in living cellular material bombarded by an ion beam can be much deeper than what is predicted by classical theories. Fig. 35 shows the fluorescence image from a 200 keV V^+ implanted peanut seed and the converted concentration-depth distribution. The mass density of the dry peanut seed is 1.01 g/cm^3 that is close to that of water. Before ion implantation, the peanut seed is cut into pieces with dimensions of 4 mm × 8 mm × 12 mm. Only a half of one side of each piece is exposed to the ion beam while the other half is covered by a 100 μm thick aluminum foil. After ion implantation, the seed is cut along the ion incident direction and the freshly cut cross section is analyzed by a two photon laser scanning microscope (TPLSM) [274]. An incident laser with a wavelength of 850 nm scans a surface area of 1.3 mm × 1.3 mm that crosses the boundary between the implanted and unimplanted areas in order to compare the fluorescence intensities in these two regions. The fluorescence image is acquired using a 460–600-nm optical band filter.

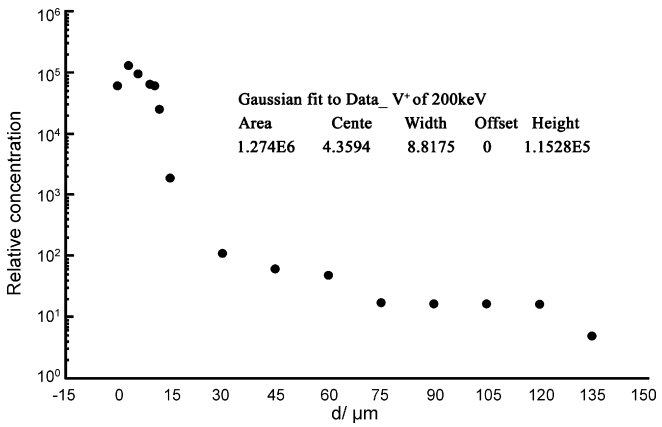

Fig. 34. The relative concentration-depth distribution of 200 keV vanadium ions implanted into peanut seed measured by PIXE [273].

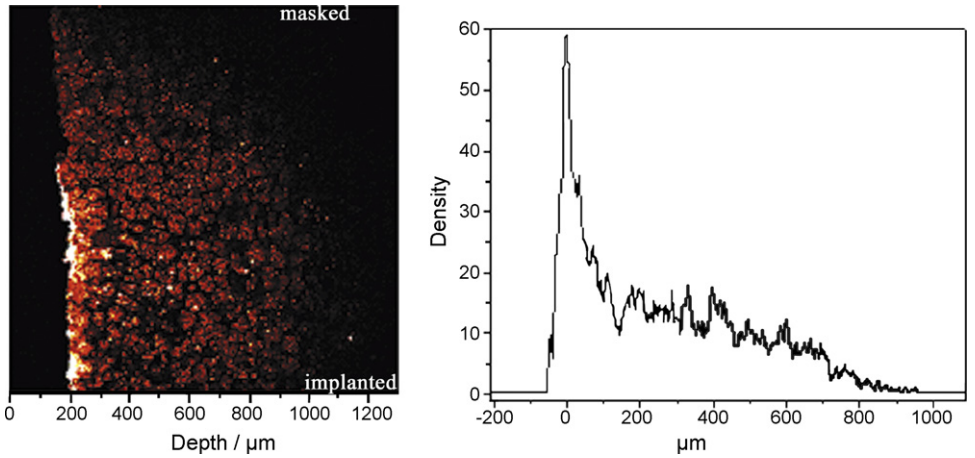

Fig. 35. Results on V-ion depth distribution in peanut seed implanted with 200 keV vanadium ions. TPLSM scanning fluorescence image (left), and converted ion concentration-depth distribution curve (right) [274].

The image reveals that ion implantation leads to an increase in the fluorescence intensity in the peanut seed and the peak is at about 50 μm. The fluorescence intensity gradually decreases afterwards and becomes almost the same as the background level at 800 μm. This indicates that the volume damage to the peanut seed caused by 200 keV V^+ implantation is at least to a depth of 800 μm. In comparison, the fluorescence signal from the masked area is relatively weak and the signal becomes progressively weaker away from the implanted area. According to the experimental findings, the range of 200 keV V ions in the peanut seed is about three orders of magnitude greater than that in water which has almost the same mass thickness as that of a peanut seed.

In recapitulation, experimental results acquired by various detection methods indicate that about 10^{-4} to 10^{-7} of the total ion flux of 10^{16} to 10^{17} ions/cm^2 with original incident energy of 30–80 keV can penetrate a distance of 30–100 μm or longer. It is because living cellular material contains free spaces with very small mass thicknesses such as gas holes, channels, and voids. Some of these features (such as gas holes) propagate all the way to the surface and some do not. When grooves and holes are gradually formed on the biological surface due to ion etching, subsequent ions can penetrate to deeper layers beneath the surface and further repeat the etching process. With increasing fluences, these free spaces that are originally not connected to the surface can be linked so that the incident ions can continuously etch the organism deep below the surface and damage several cell mono-layers near the surface. These deep incident ions that have lost a portion of their kinetic energy can interact with the biological molecules inducing physical and chemical molecular damage. If the damaged molecules are genetic substances, mutation may result.

4. Applications in life sciences

In the above sections, the physical and chemical processes pertaining to the interaction between low-energy ions and organisms are reviewed. These studies and results have laid the foundation for the application of ion beam to life sciences. For example, the reactions between low-energy ions and simple molecules are used to simulate the original processes in the evolution of life and syntheses of interplanetary molecules. Sputtering intrinsic to ion beam bombardment is used to analyze molecular structures of biological targets. In this section, we will discuss typical applications of low-energy ion beam interaction with organisms, including structural analyses of viruses, gene delivery assisted by ion beams, and mutation breeding of crops and industrial microbes with particular attention to the more recent developments. The general features and technical issues pertaining to sample preparation, ion implantation, and screening of mutants from ion beam mutation can be found in a number of related publications cited in the subsequent sections.

4.1. Analyses of organism structures by ion beam etching

Ion beam etching can be used to remove layers of a biological target. Both focused ion beams (FIB) and broad ion beams (BIB) are used to characterize biological specimens. They are particularly useful in microscopic techniques and

much knowledge has been gained [257,275–277]. Ion beam microprobe which offers unique advantages in imaging is similar to SEM, but instead of using electrons, the technique employs relatively low energy ions as the source [278]. The ion beam, usually made of argon, oxygen, nitrogen or cesium ions, ejects secondary ions from the specimens and they are subsequently analyzed by a mass spectrometer. Spatial resolution of better than 500 Angstroms is not difficult using a micro-focused ion beam and 100 Angstrom resolution (close to the theoretical limit) seems achievable. While this method can only analyze the surface of the specimen, the ''surface'' can be eroded away by sputtering thus allowing progressive access to deeper layers.

Argon sputtering is usually adopted to progressively expose inner cell structures without apparent damage. Coca-2 human colon carcinoma cells have been desiccated and subjected to 3 kV argon sputtering in vacuum for 0–15 min depending on the desired cell structure to be exposed. With different sputtering time, the structure of cell cytoskeleton, vesicles, mitochondria, nuclear membrane, and nucleoli can be imaged. The sputtered cells are compared by using a variety of imaging methods including confocal fluorescence microscopy, TEM, SEM, and X-PEEM (X-ray photoelectron emission spectromicroscopy). Similarity of several reference intracellular structures, including cytoskeleton fibres, cell–cell and cell-substrate adhesion structures, and secretory vesicles, suggests that ion sputtering is a valuable tool for surface sensitive microscopy [257].

Etching using keV ions has been utilized in viral studies [258,279–283]. Nitrogen (2–7.5 keV) and argon ion beams (1 keV) are employed to erode the surfaces of various virus particles, including the rod-like tobacco mosaic virus (TMV), icosohedral bacteriophage T4 and λ, and human adenovirus 2. Ion etching of TMV that contains the ^{35}S-labled protein or nucleic acid incorporating ^{3}H-thymidine suggests that the protein subunits are more susceptible to ion etching and the residual materials are predominantly the nucleic acid of the virus. The preferential effects on proteins and nucleic acids play a crucial role in the subsequent elucidation of the arrangement of nucleic acids in the mature head of bacteriophage T4 and λ.

With performing ion etching at lower energy (1 keV 1.95×10^{15} cm^{-2} s^{-1} Ar^{+}), the apparent virion diameter of the human adenovirus 2 is found to decrease linearly in the initial 30–45 s of etching and more gradually afterwards. Etching that is sufficiently long to reduce the viral diameter by 20–30 nm reveals distinct substructural elements in the virion core. The cores are found to consist of a cluster of 12 large, uniformly sized spheres, ''adenosomes'', having a diameter of 23.0 ± 2.3 nm, and they are related to each other by two-, three-, and fivefold axes of rotational symmetry. The results confirm the hypothesis that the adenovirus 2 core is composed of 12 large spheres packed tightly together in such a way that each is directed toward the vertex of an icosahedron (Fig. 36a). The adenosomes contain the viral DNA combined with the virion protein VII and perhaps also with protein V. The Ar^{+} ions erode the adenovirus capsid in a gradual way that permits the core structures to be determined in the native state. Hence, the virions do not need to

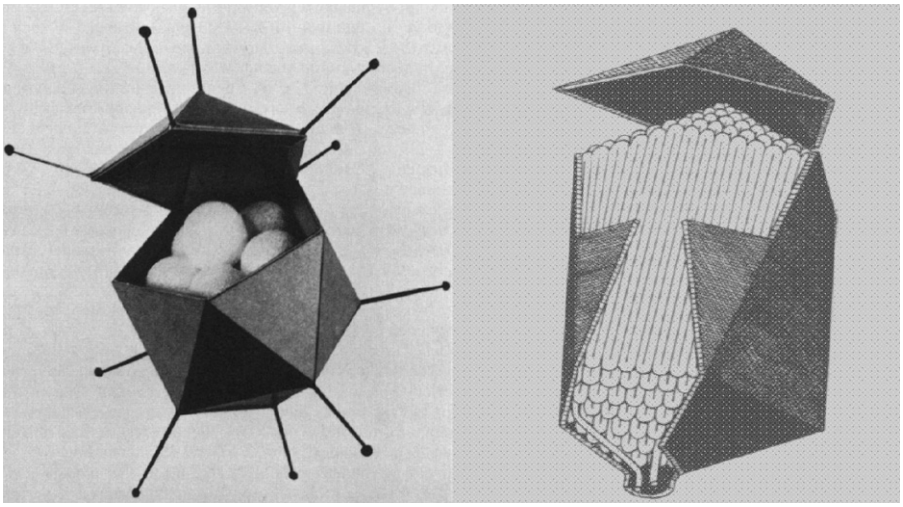

Fig. 36. Model showing the proposed arrangement of large spheres (adenosomes) inside the adenovirus 2 capsid. A portion of the capsid has been raised to expose the core and to illustrate the orientation of adenosomes immediately beneath the capsid vertices (left). Reprinted with permission from [283]. Copyright 1984 the American Society for Microbiology. Spiral-fold model for the arrangement of DNA inside the head of phage T4 (right). Reprinted with permission from [258]. Copyright 1985 by the National Academy of Sciences.

be chemically dissembled before the core structures can be visualized. The etching rate depends critically on the total current which is typically varied over a wide range (e.g. from 1 to 25 mA). Erosion of the virus by Ar^+ is nonspecific in that it does not depend on the particular biochemical properties of the virion surface components.

For T4 and λ phages, after ion etching, the DNA from the etched phages and substrate are collected to determine the radioactivity of the selectively labeled DNA or protein. Agarose gel electrophoresis is used to separate the DNA fragments and Sourthern hybridization is employed to correlate the fragments to genomic positions. While the overall structure of the virus particles is preserved, the radiolabeled terminal portion of the T4 DNA molecule and the right end of the λ DNA are found to be eroded more rapidly than the remainder of the DNA, suggesting that the first DNA (e.g. left end for λ DNA) to enter the prohead is condensed in the center of the capsid and therefore shielded from the ion beam by the surrounding packaged DNA. A ''spiral-fold'' model has thus been proposed to explain the arrangement of DNA within the icosahedral bacteriophage head. It consists of phage T4 and λ DNA strands running parallel to the long axis of the phage, making sharp (180°) bends at the top and bottom of the capsid, and the folds themselves are arranged radially about the long axis of the head in spirally organized shells (Fig. 36b). All in all, ion etching is crucial to the studies of virus structure. It should be noted that virus erosion by low-energy ions is nonspecific and it is quite possible that ion beams can be employed to analyze many other organisms as well.

4.2. Gene delivery assisted by ion beam

4.2.1. Mechanism of gene delivery assisted by ion beam

Genetic transfer or gene transfer or transformation is the genetic alteration of a cell resulting from the introduction, uptake, and expression of foreign genetic material (DNA or RNA). Because of the natural physical and biological defending mechanisms of organisms, foreign molecules cannot get into the cells of most organisms in the natural state, although some bacteria species may get into a state called natural competence under specific conditions such as nutritional stress. Therefore, a number of simple and effective means are sought to realize gene transfer into cells, and a myriad of physical (electroporation, microprojectile bombardment, spatially indexed nanofiber arrays) [284–286], chemical ($CaCl_2$, polyethyleneglycol) [287], and biological (Agrobacterium, microinjection) [288,289] methods have been developed to implement bacteria, plant, and animal transformation. The common technique in most of these methods is to perforate the cell wall without severely injuring the cell and to provide exogenous genes with a passage to enter the receptor cell.

In the study of the interaction between low energy ion beams and cell surfaces, researchers have discovered the thinning effect of the ion beam on cell walls and proposed ion beam induced gene transfer. The principle of ion beam assisted gene transfer is similar to that in other physical approaches in that the pathway formation is a prerequisite and basis for gene transfer into walled cells and mature embryos. Ion beam mediated transformation also has its own specialties. As described in the previous sections, low energy ion beams can etch and perforate the surface resulting in the formation of microcrater-like pathways on the cell envelop. A simple measurement of the permeability (denoted by electro-conductivity in experiments) of the sample before and after ion implantation can post evidence of the 'perforating' effect in mature crop embryos that are often used as receptors in gene transfer. For example, if ion etching makes micro-holes in the surface of mature rice embryos, the cellular inner substance will permeate into a solution through micro-holes and a balance will be reached finally. Table 4 shows the changes in electro-conductivity of non-shelled rice seeds of Indica Guanglu-short No. 4 after ion beam etching using 3×10^{16} and 6×10^{16} N^+/cm^2 [290].

The mean permeability of four groups of samples that are not ion-beam-etched is 4.3 ppm, and the mean permeability values of the samples etched with 3×10^{16} and 6×10^{16} N^+/cm^2 are 17.3 ppm and 29.0 ppm,

Table 4
Effect of ion etching on the permeability (ppm) of naked rice seeds in solution

Treatment	Control without N^+ implantation	3×10^{16} N^+/cm^2	6×10^{16} N^+/cm^2
I	3.0	15.0	29.0
II	4.5	20.5	32.0
III	3.0	23.0	32.0
IV	6.0	10.5	23.0
Average	4.3	17.3	29.0

respectively that are more than four and six times of that of the control. This indicates that ion etching increases the out permeation of the cellular substance, which is probably due to the surface damage by ion etching. If the solution contains exogenous DNA molecules, the probability of exogenous DNA entering the cell also increases.

It is interesting to study how exogenous genes enter the cell actively or passively. In Section 3.3, charge exchange between charged particles and the organism surfaces is shown to change the electrical polarity of the biological molecules (e.g, positive charge replacing negative one). For a cell, the change in the electrical polarity cannot be macroscopically measured as the cell is a very poor conductor, but local electrical polarity may change at the hemispherical cap irradiated by positive ions. Thus it is possible that due to the accumulated positive charge, the ion etched pathway walls may become electrically positive. This causes an electrostatic attractive force to the electrically negative exogenous DNA and facilitates transfer into the cell, so that the associated DNA can be admitted. Even if local polarity does not change at the gene transferring pathways, a decrease in the short-distance electrostatic repulsion between two electronegative points can be beneficial to the entrance of new genes due to decrease in the receptor negativity. On the other hand, ion etching takes place in vacuum, and water in the mature embryos must be exhausted first. When dry embryos are put into a DNA-containing solution, the probability of exogenous DNA entering the cells via newly formed channels is enhanced due to the increasing effect of absorption and expansion. Moreover, ion implantation induces some long-living free radicals in the biological organisms and at the same time causes damage to the chromosome in the plant cell, inducing and stimulating repair and reconnection of DNA in receptor cells. All of these factors favor inserting and integrating exogenous DNA into the host chromosomes and increase the efficiency of transfer [1,291,292].

The physical evidence of foreign molecules getting into plant cells has been obtained in trypan blue (TB) and neutral red (NR, 300 Da) dye molecule transferring experiments using argon and nitrogen ion bombarding at energies of 15–30 keV with fluences ranging from 5×10^{14} to 3×10^{16} ions/cm^2. The tissue survival after ion bombardment, degree of damage to the cell wall, and penetration of dye molecules into the cells depend on the ion species, energy, and fluence. Dye molecule transfer occurs in accordance with the degree of damage to the cell wall. Normally, intact or uninjured plant cells can prevent the vital dye from entering the cells while the dye molecules accumulate in the vacuoles of the damaged but still alive cells and these exogenous molecules are then exhausted from the cells *via* the process of exocytosis. Trypan blue dye molecules (molecular weight of 1000 Da) cannot enter the cells of the unbombarded embryo, but they can enter the cell wall and accumulate in the apoplast of the cells that have been bombarded by 30 keV, 1×10^{15} ions/cm^2 Ar^+ ions (Fig. 37d). When the fluence is increased to 2×10^{15} ions/cm^2, the dye can enter the cells where they circulate in the cytoplasm (Fig. 37e), implying that the cells are functional and alive. At a higher fluence of 4×10^{15} ions/cm^2, the cell envelope surface is severely damaged and the dye accumulates in the nucleus areas (Fig. 37f), indicating that the cells are inactivated. Ion bombardment using different ion species and dyes such as nitrogen ion and neutral red dye is found to have the same effects. That is, penetration of the exogenous molecules is closely related to the ion parameters.

4.2.2. Ion beam assisted gene transfer into plant cells and bacteria

Since Yu et al reported the successful *GUS* and *CAT* gene transfer into suspension cells and mature rice embryos following the 20–30 keV argon ion bombardment [256], a number of reports have emerged on ion bombardment induced foreign molecule transfer into plant tissues and bacteria cells [293–296]. The chitinase gene (*RCH8*) in plasmid vector pCAMBIA1308 has been reported to be delivered into three wheat cultivars (Yangmai 158, Wan 9210, Wanmai 32) by a low energy Ar^+ beam-mediated method, and molecular blotting assays confirm stable integration of alien DNA fragments into wheat genome [296]. The plant transformation frequencies which depend on the plant species and ion fluence range from 0.5 to 3.8%. Leaf extracts from the second-generation of the transformed plants can inhibit the growth of wheat scab. Similarly, using a carbon beam extracted out of vacuum, Hase et al. have developed the methodology of tobacco pollen gene transfer in which the *pCH* gene is transferred into dry pollen of *Nicotiana tabacum* L. [297].

In addition to rice and wheat, genetic transformation induced by keV ion beams has been applied to other plants. For instance, after 20 keV N^+ irradiated tobacco seeds are immersed in a buffer solution of pBI121 (carrying *nptII*^{r} and *gus* genes) and screened by 100 mg/L Kanamycin, three NPTII^R plants are obtained. Leaves from these transformants are differentiated and regenerated into resistant plants. Both the PCR amplification and Southern blot prove that the *gus* gene has been inserted into the tobacco genome [298]. Similarly, the recombinant plasmid pBWI (containing *gus*, *nptII*^{r} and *Cecrropin B* genes) has been transformed into cotton cells with walls [299].

On the heels of successful gene transfer in plant cells, gene transfer into bacteria has also been performed. Argon and nitrogen ion beams are used to bombard the bacteria *E. coli* in vacuum (26 keV, 0.5–4 $\times 10^{15}$ ions/cm^2). Three

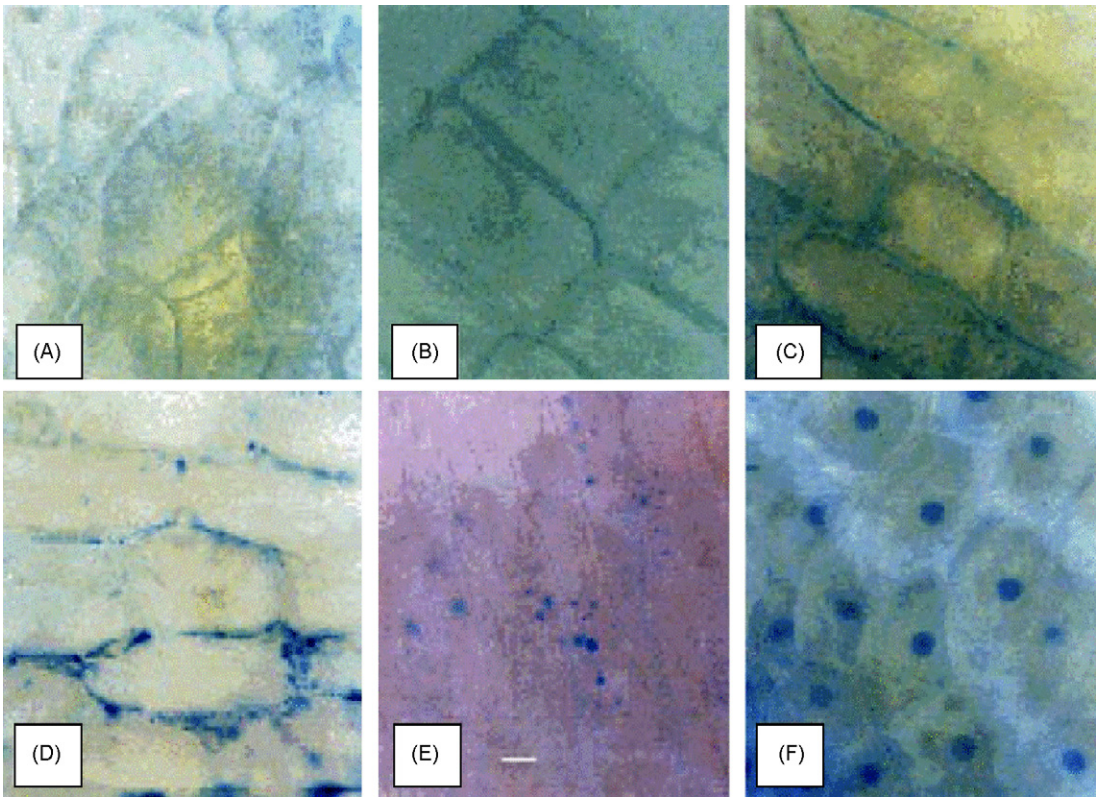

Fig. 37. Optical micrographs of trypan blue stained 30 keV Ar^+-bombarded and unbombarded corn embryo cells: (A) fresh control, (B) vacuum control, (C) fluence of 5 × 1014 ions/cm^2, (D) fluence of 1 × 1015 ions/cm^2, (E) fluence of 2 × 1015 ions/cm^2, and (F) fluence of 4 × 1015 ions/cm^2. The bar in the photo indicates 5 μm. Reprinted with permission from [291]. Copyright 2004 by Elsevier.

kinds of plasmid DNA, pGEM2, pGEM-T easy, and pGFP carrying different marker genes, are subsequently transferred separately into the ion bombarded bacteria and successfully expressed [300]. It indicates that energetic ions with an ion range approximately equal to the cell envelope thickness and implanted with the appropriate fluence are able to facilitate the transfer of foreign molecules through the cell envelope without irreversible damage.

4.2.3. Ion beam assisted transfer of gene clusters

Nowadays, transferring a single function gene cloned in a vector like the above examples is feasible in most cases as long as the sequence and functional information of the target gene is available. In the genetic transformation process, the gene is normally separated and extracted or artificially synthesized. After being cut outside the cell and combined with a vector (such as a plasmid), the recombinant is transferred by various ways into a receptor cell and integrated into the genome of heterologous cells to be expressed. However, as it is known, the regulatory expression of genome is a complex network. The behavior of certain phenotypes or functions may involve the cooperation of multiple genes distributed consecutively or far away from each other on different chromosomes. Due to restrictions of the vector system, the contained meaningful genetic fragment is normally only a few kilo bases long. This volume is often too small for plant gene groups, which can be as long as tens of mega bases or even larger. On the other hand, even though the transferred gene can be expressed in the regenerated plants, it may be lost in the next generation. Though genetic engineering has made great progress, we are still confronted with such problems as lack of beneficial genes, especially the genes dominating some significant crop characteristics. Moreover, most characteristics are dominated by multiple genes. It is very difficult to clone them and sometimes what needs to be done is to only change the expression level of the corresponding genes. However, very little is known about the mechanism of gene regulation at the present time. Therefore, transferring of large DNA fragments, or gene groups, or even the whole genome is a direction for future research.

In plant genetic engineering, it has been attempted to transfer the total DNA of one kind of crop into other plants by molecular hybrid approaches making it possible for genetic crossing (heterosis) among distant relative species. For

example, red hemp DNA can be delivered from cotton and maize DNA to rice. Some preliminary investigations have been performed [292,301]. The genomic DNA of a variety of maize with purple seed skin has been transferred to mature embryo of rice using ion bombardment, and the results show that some traits of purple corn (stronger root system, more vascular bundles, purple color in shoot, spike tip and stigma, high efficiency of photosynthesis) are continuously expressed in the transgenic rice (Fig. 38) [301–303]. The RAPD analysis shows that some new bands which have the same molecular weights as some bands in the purple maize appear in the transformed rice lines. This work indicates the feasibility of transferring DNA from C4 plant maize into C3 rice using ion beams [304].

Water melon has been playing an important role in agricultural development and pumpkin is naturally immune to the watermelon pathogen, *Fusarium wilt*. Ion beam technology has been applied to introduce pumpkin genome DNA into the mature embryo cells of watermelon in order to obtain new disease-resistant material or germplasm. Among the 120 watermelon seeds treated with ion bombardment and pumpkin DNA transformation, one of the first-generation plants (44.2% survival rate, i.e. ∼52 surviving plants from 120 seeds) shows leaves with a unique shape. In the second-generation plants grown from 360 seeds of this single-fruit, 28 plants (7.8%) survive the natural resistant screening in disease-infected soil and fruits from two plants display different color from the receptor but similar to that of the donor [305].

Ginkgolides are biologically active terpenic lactones present in *Ginkgo biloba* L. It has significant effects on various neurodegenerative diseases, but its supply by natural resources is quite limited probably because of the slow growth rate of Ginkgo trees. Gingko genomic DNA has been used to transform watermelon dry seeds with the aim to obtain watermelon species that can express abundant ginkgolides or ginkgo ketone. Three main elements of ginkgolides, GA, GB, and GC, have been detected in leaves of the transgenic watermelon. The stability and inheritability of the ginkgolides expression is being investigated based on the offsprings of the positive transgenic watermelon plants [306].

The genome DNA from *Ephedra glauca* has been transferred to yeasts *Saccharomyces cerevisiae* and *Hansenula anomal* by argon and nitrogen ion bombardment, respectively. Twelve yeast strains that are capable of producing L-ephedrine and D-pseudoephedrine using glucose as the carbon source and $NaNO_3$ as the nitrogen source have been obtained. After 72 h culturing in liquid medium, the extracellular contents of L-ephedrine and D-pseudoephedrine produced by the recombination strains reach 18.85 and 4.11 mg/L, respectively, and the cellular contents of these two

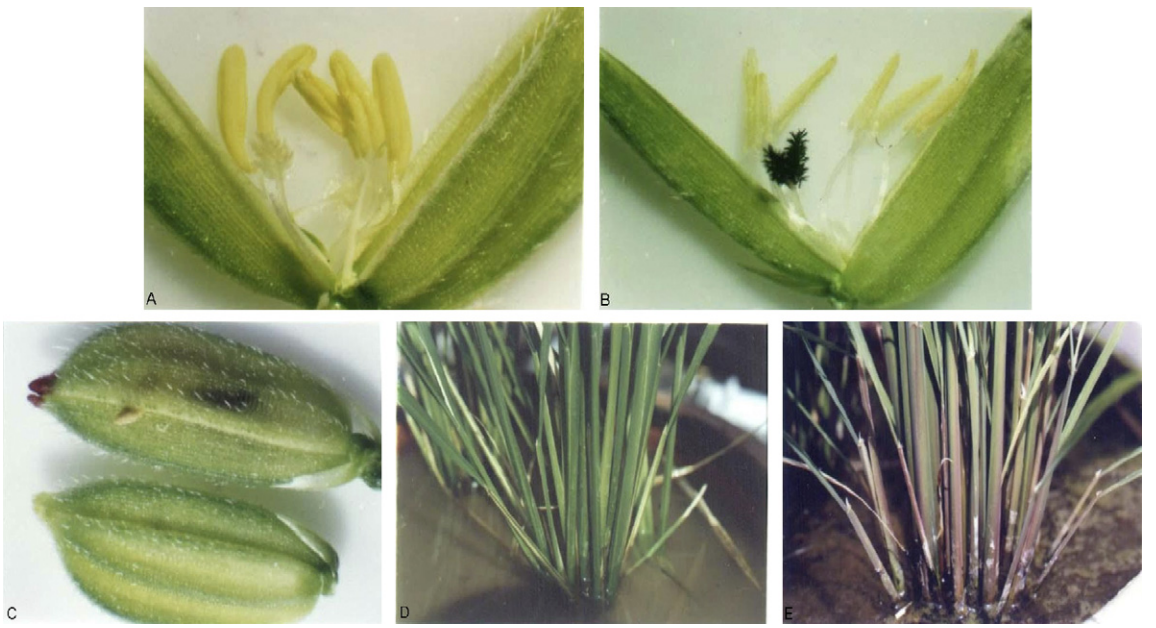

Fig. 38. Some maize characteristics are expressed in the offspring of rice that is transferred with the genomic DNA of maize by ion beam technology. (A) A spikelet of rice EI213, the receptor of transgene, showing the stigma in its natural buff color. (B) A spikelet of transgenic rice, showing the stigma in dark purple color. (C) Spikes of EI213 (bottom) and transgenic rice (top) with the tip in purple color. (D) Stem of EI213 in natural green color. (E) Stem of transgenic rice in purple color.

products are 4.29 and 294.86 mg per gram of dried cells. It is found that integral macromolecular DNA and nitrogen ion bombardment result in higher transformation efficiency than fragmented DNA and argon ion bombardment [307].

4.3. Ion beam mutation breeding of plants [1]

4.3.1. Induced DNA damage and its application in mutation breeding [1]

Biological effects arising from physical stress constitute an important part of the fundamental knowledge in life sciences. When a biological organism is acted upon by various physical factors, initial physical or biophysical processes can initiate within 10^{-9} s. This direct response is known as the preliminary effect or radiation damage. Afterwards, relatively stable biochemical changes may occur leading to primary biochemical effects. Other biological effects can be further induced, eventually bringing about changes in the structure or function at a certain level in the organism, and these are called the biological end-point effects. Gene mutation is one of the most important effects to organisms. In theory, it is closely related to the understanding of genetic substances as well as the evolution of life forms. In practice, mutation studies form the theoretical basis of modern breeding techniques.

It was generally regarded in the past that DNA structural changes, whether man-made or natural, would all result in death or aberrations of organisms. In fact, DNA structural changes may not bring about aberrations but may be the prelude to a complicated series of induced processes. Only when repair is ineffective or mistakes occur during the repair will aberrations or individual death follow [308]. An aberration process has the following stages: mutagen contacting DNA → premutation → mutation → occurrence of genotypes. Radiation damage refers to changes caused in the DNA structure and is thus premutation rather than mutant genotypes. After formation of premutation, DNA recovers to its original normal structure due to the organism repair system [309]. Only a few DNA molecules are transformed to the mutant state to bring about the occurrence of genotypes.

Mutations are essential to plant breeding. In plant material used for breeding, most of the useful genetic variations have evolved naturally and have been selected because of previous gene mutation or recombination. Crops for human use and consumption have been affected by planting practices and artificial selection by humans. However, for most plant varieties, the theoretical production limits have not been approached and future plant breeding is facing challenges. Hence, major improvements in breeding methods are needed.

Modern breeding methods originating from physics, chemistry, or biotechnology have two general steps. The first one is the creation of genetic variations and the second one is the screening of beneficial mutations. Artificially controlled hybridization is the current method in which the genetic materials of different crops are redistributed and recombined. The problem is that the natural gene reservoir is limited and the natural mutation rate is only about 10^{-7}. In order to increase the germ plasm resources for hybridization breeding, artificial and new genetic variations that have good adaptability are important.

One of the most important applications of artificially induced mutations is direct mutation breeding, which uses mutagens to treat the plant sexual or asexual offsprings to induce ideal genotypes. Actually, direct mutation breeding does not rule out the use of useful mutants as germ plasm resources. In principle, induction of excellent germ plasm resources and special genotypic materials can breed groups of excellent varieties. Traditionally, the so-called mutation breeding refers to direct applications of mutants.

At present, there is a variety of physical and chemical mutagens. Since the mutagenic effects of ion implantation were discovered, ion beam as a new mutagen has been extensively applied to genetically modify cereal crops, vegetables, and flowers [310–312]. One of the important reasons is that ion implantation induced mutation integrates the factors of mass, energy and charge together with the induced damage to the biological materials (including genetic substances) resulting in the biological molecules and atoms being displaced, recombined, and compounded as discussed in Section 2. From this point of view, ion implantation acts on organisms like a compound mutagen with both physical and chemical mutagenicity, and its mutation efficiency is generally higher than a single mutagen. The effects induced by ion implantation in plants include phenotype alterations in contemporary plants and offsprings [313,314], changes of biochemical and physiological properties [315], and molecular and genetic modifications in mutants [315–322].

4.3.2. Principle of ion beam mutation breeding [1]

Ion beam as a new mutagen has its own unique features determined by the interaction between low energy ions and biological organisms. After the breeding goal set, the ion-energy, ion species (active or inert gaseous ions or metal ions) and irradiation fluences must be estimated. These parameters also depend on many other factors, for instance, the

method of sample treatment. Table 5 shows the mutation rates of glutinousness (changing from the glutinous positive phenotype to negative) in the middle-season sticky japonica rice variety Shao 86–87 after N^+ irradiation of various parts of its dry seeds. When the embryo bud (growing tip) directly faces the ion beam, the mutation rate is the highest, whereas the data show no great differences from the control when the endosperm part is up or the ion beam is blocked. Hence, it is known that only when ion beam directly faces the embryo growing tip can effective mutations be induced, because the penetration depth of low-energy ions in organisms is limited.

In general, variations created by mutation methods are related to the properties of the mutagenic factors and also the characteristics of the biological objects. For the perspective of ion beam mutation, all of the characteristics of the mutagenic factor, properties of the chosen biological object, and correlations between the factors and the objects should be considered. The preferred way is to carry out preliminary treatments of the sample material and make a statistical study of the relationship between the mutation rate and damage degree (normally indicated by the survival rate) and the fluence. In order to get high mutation efficiency, a fluence level at 50% survival fraction is normally accepted for mutation breeding.

As aforementioned, the interaction between the implanted ions and complicated organism is more complex than classical radiation such as γ-ray. This is also manifested by the complex dependence of the damage rate on the ion fluence. In general, the survival rate under γ-ray radiation drops exponentially with the dose, whereas the survival rate under ion implantation exhibits oscillation with a down trend with the ion fluence. The survival rate decreases initially, increases at higher fluences, and decreases again with very high fluences (Fig. 39). The phenomenon can help to determine the proper fluence range in ion beam mutation breeding. According to statistical results, a high mutation rate and wide mutation spectrum can be obtained when the fluence is in the increasing segment of the survival curve. For example, improved mutation rates in *Arabidopsis thaliana* are obtained at the mutation fluence of 10^{15} ions/cm^2 (see Fig. 39) [319].

4.3.3. Ion beam mutation in plant breeding [1]

As a compound mutagen, the multiple combinations of implanted ion energy, ion species, charge number, and particle number lead to plentiful and diverse biological effects. This has boosted widespread applications in plant breeding. According to the breeding goals, different ways to exploit ion beam induced bioeffects in plant breeding are

Table 5
Mutation rates of glutinousness in the middle-season sticky japonica rice variety Shao 86–87 after N^+ irradiation at various parts of its dry seeds

Ion implantation mode	Glutinousness mutation rate (%)
Implantation in embryo bud	8.7
Implantation in endosperm	0.5
Blocking of ion beam	0.11
Control	0.15

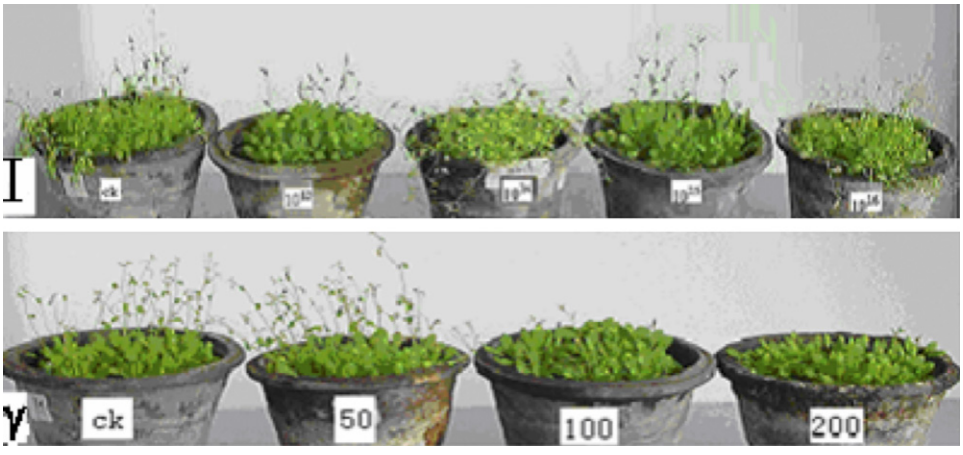

Fig. 39. Survival levels (indicated by the growth ability) of *Arabidopsis thaliana* after N^+ irradiation with fluences of 0, 10^{13}, 10^{14}, 10^{15}, 10^{16} ions/cm^2 (from left to right, upper panel) and ^{60}Co γ-ray irradiation at doses of 0, 50, 100, and 200 Gy (from left to right, lower panel) [319].

explored. For example, some ways take advantage of the stimulation effect of ion implantation on crops, some make use of ion implantation induced genetic effects, and some employ ion implantation to create aneuploids of wheat, and so on. Nevertheless, any effects beneficial to variety improvements have scientific and economical impact.

4.3.3.1. Application of a specific stimulation effect [1,323,324]. In ion implantation experiments, it has been observed that for crops such as tobacco and sweet-leaf chrysanthemum, the leaf production and intrinsic composition of leaf in the present-generation plants evolved from seeds bombarded by ion beams are improved. Such a stimulation effect, i.e. improvement of some beneficial agrinomic qualities exhibited in the present-generation plants (or fruits, etc.) induced by ion beam, is of important economical significance. This effect is partly ascribed to the etching process of low-energy ions on seeds, which can improve the permeability of the shell surface and facilitate the exchange of external substances (nutrients and water, etc.). Consequently, the germination rate is increased and the growth potential is enhanced and maintained. Although the stimulation effect may occur randomly in other mutagenic activities, its repeatability has only been reported in ion beam mutation research. In other words, the stimulation effect is unique to ion implantation into some plant species (Tables 6 and 7). When the ion energy and fluence are controlled properly, the reproducibility of the effects is high. No matter whether the stimulation effect is inherited or not, it can be directly applied to the present generation and its value is significant. This application is worthy of further exploration. For example, airplane sowing of grass seeds onto deserts and tree seeds on waste-mountains should be done shortly after raining and high-quality seeds are required to increase the germination speed and growth potential of seedlings. The biological effects of the physical factors are very complicated and the applications discussed here are only examples. In addition to the etching effect, it is likely to be related to the expression of some genes that are activated and thus the kinds, structures, and activities of the proteins determined by these expressions are subsequently changed.

4.3.3.2. Application of mutants

In ion beam mutation breeding, the frequency of inducible multiple mutations that have favorable characteristics is quite high. Therefore, most breeding workers take ion-beam-induced mutants directly for production. Indirect applications of the mutants also increase considerably as the mechanistic studies of ion interaction with organisms expand our practical experience.

4.3.3.2.1. Direct application of mutants. In breeding practices, plant breeders seek high production, high quality, and high adversity-resistant varieties. Varieties that are resistant to plant diseases and insect pests are particularly of interest. Ion beams can be used to induce mutations with the desired characteristics. A number of improved varieties and breeding materials with better compatibility and excellent agronomic traits have been screened and qualified [79,80,325,326]. Some of these stocks are suitable for immediate agricultural production.

In 1988, 500 dry seeds of rice variety Zhe-15 were implanted with 30 keV N^+. Extensive variations occurred in the M2 generation and 300 mutant plants were selected from which the early-season indica rice stock S9042 was bred. Its fertilizing period was 4.6 days ahead of normal early-season varieties and its trunk height was 10 cm shorter than the control. In laboratory test, S9042 exhibited high or medium resistance to 14 out of 20 species of rice-infecting pathogens. Its field production reached 515.3 kg/667 m^2 in a 2.5 hectare planting area, being the top of the eight varieties tested in field planting. In 1991, S9042 was planted in a 2-ha field. After the tassel stage, in spite of experiencing severe flooding including flood water for 4 days and inundation in water for 21 days, its yield still reached

Table 6
Alterations of the intrinsic chemical composition of leaves after 13 keV N^+ implantation in tobacco seeds (degree of increase or decrease in percentage) [323]

Variety	Holo-nitrogen (%)	Holo-phosphorus (%)	Holo-potassium (%)	Protein	Cl	K/Cl
S79-1	−6.9	14.3	17.7	−7.9	−27.4	62.2
K399	−19.6	31.4	43.0	−24.1	−8.72	65.6

Table 7
Alterations of some characteristics of sweet-leaf chrysanthemum after N^+ implantation (degree of increase or decrease in percentage) [324]

Germination rate +41%	Seedling rate +500%	Leaf production +41%	Sweet chrysan themum sugar +1%
Total sugar +2.8%	A glycosides +162%	Total glycosides +83%	High-quality rebaudioside A +1.8%

320.5 kg/667 m^2, which was 38% higher than the locally planted variety early-season-rice 213, displaying excellent resistance to water logging. During the rice growing period in 1993, there was frequent raining in southern China, resulting in severe rice blast of early-season-rice varieties. Some fields had nothing to harvest and the yields of 60% of the planted fields decreased tremendously. However, in an area of 3333 hectares, S9042 showed high resistance to rice blast disease and the yield was up to 384.4 kg/667 m^2. In 1994, S9042 was officially authorized by Anhui Province (named as Rice Wan 20) for large-scale planting in the Yangtze-river region (Table 9, No. 9).

Another new stock, late-season japonica D9055 with high yield and quality has been bred by ion beam mutation also. In comparison with its original variety Eryi-105, D9055 has stronger growth potential, higher stem, and bigger spikes, but its maturation time is 2 days later than the control. In a test held in 1990 for double-season-planting of late-rice varieties, D9055 achieved an average yield of 473.1 kg/667 m^2, an increment of 8.4% compared to Eryi-105. From 1991 to 1993, D9055 was planted in a few counties in Anhui, and the average yields were between 452.2 to 481.5 kg per unit area (667m^2), which were 20–38.25% higher than those of the local varieties. The major indices of the rice quality for this stock were rated first class according to the standards issued by the Ministry of Agriculture of China. D9055 has also been official authorized by Anhui Province (named as Rice Wan 42) for large-scale planting in both Anhui and Hubei Provinces (Table 9, No. 10).

4.3.3.2.2. Indirect application of mutants. As a new mutagen, ion beams can create abundant variations. However, only a limited fraction of these variations is directly applied in production. For example, according to a paper-survey at the end of 1994, we carried out ion implantation of plant seeds for more than 60 breeding groups from all over China, and a total of 11,831 mutants and 1382 usable mutated materials from these mutants were obtained. However, only a fraction of new stocks that accounted for ∼1.0% of the mutated materials were further bred. Most of the mutated materials would be indirectly used. Based on our present knowledge, indirect applications of aberrations may follow different ways. Firstly, mutants are hybridized with other parent materials to produce hybrids in next generations, from which new stocks that have improved characteristics or new materials that have special applications are selected. For example, rice yellowing mutants were hybridized with photo-sensitive sterile stocks to transfer the yellowing gene into photo-sensitive sterile stocks producing a group of new stocks which have good breeding, spawn-separation, and disease resistance characteristics. These new stocks have the yellowing marker. The self-crossing of sterile stocks produces yellowish leaves while the hybrid F1 has normal green leaves. Thus, it was easy to remove undesirable hybrids during the field-seedling period. Even if the yellowish seedlings are not artificially removed, due to their weak growth potential, they will not survive during the F1 growth period. This is very important to the practice of hybrid rice production. Secondly, ion beams can be used to modify some bad characteristics of hybrid parents to explore useful genes and breed good hybrid combinations. For example, ion implantation has been carried out on tomato stock ‘‘Zaoxia (Morning Glow)’’ to produce seven new stocks characterized by early maturation and large fruits. These are bred into hybrid tomato Yanfu-1 which has early-maturation and high-production characteristics. Tomato Yanfu-1 had been authorized by Shandong Province, named as Tomato Lu No. 7 in 1997 (Table 9, No. 1) Ion implantation into silkworm's eggs can improve characteristics of the hybrid parents for the father (named 991) and the mother (named 992) leading to better hybrid varieties. New silkworm variety 991 × 992 has high yield, thick fibers, and broad resistance. It has been authorized by Anhui Province in 2002 (Table 9, No. 21). In another example, good-compatibility rice stock 02428 is treated with ion beam and the subsequent generation mutant series that flower 1–2 h early are selected. This is of critical importance in overcoming the natural physiological obstacle between 02428 and indica rice. In their natural conditions, flowering periods of the two series do not overlap with each other, and their hybridization is almost impossible. The selected 02428 mutants that have advanced flowering time and long stem can facilitate their hybridization with the short-stem sterile mothers. The applications of these mutant series are notably significant in hybrid rice study and production. Thirdly, mutants can be used to study gene regulation and control. The basic clue is to first look at a certain function of the biological organism and then to induce and identify mutants which cannot realize this function. Genes normally encode various characteristics and these characteristics can be clearly expressed in experimental biological organisms. If mutants can be obtained and they also have sufficient survival time for analysis, important inferences on transmitting coding can be derived from them. Therefore, utilization of ion beams to produce rich variations is of significance to both production and scientific research.

4.3.3.3. Application of distant hybridization. Distant hybridization is an important way to create new bio-species and resources and transfer the allo-genetic substances. However, it is difficult to apply distant hybridization to hybrid fruiting and hybrid sterility and so hybrid offspring is rarely produced. Ion implantation of either fathers or mothers or

hybridized generations can have effects on the hybridization fruiting rate, hybrid fruiting rate, and hereditary process of the offspring.

Effects on hybridization fruiting rate. Ion implanted common wheat Premebi as the mother has been hybridized with rye AR1. The fruiting rates under three ion fluences are all higher than the rate of control (0.64%), and the mean rate is 4.03% which is 6.3 times of the control. The ion implanted tetraploid rye as the father is hybridized with octaploid rye and produces an obvious effect in the present-generation fruiting rate. Generally, the fruiting rate can be increased by 1.5–3 times after ion implantation.

Effects on hybrid fruiting rate. In another experiment, the hybrid F1 of the controls of octaploid rye DDIB and tetraploid rye shows a spike-fruiting rate of 25% and mean fruiting of 0.38 grains per spike. In comparison, the hybrid F1 of the controls of octaploid rye DD7A and tetraploid rye has a spike-fruiting rate of 37.5% and mean fruiting of 0.56 grains per spike. After ion beam treatment, the spike-fruiting rates and mean fruiting grain number per spike of both hybrids F1 all increase. With a fluence of 2×10^{16} ions/cm^2, the mean spike-fruiting rate goes up by 32.15% and the mean fruiting grain number per spike is increased by 2.58 for both hybrids.

Effects on the hereditary process of hybrid offspring. In the offspring of distant hybrids, due to gene partition and recombination, segregation starts from the second generation. For example, for the hybrid of sea-island cotton and land cotton, generational segregation and selection can lead to stably hereditary cotton plants after more than ten generations. However, the characteristics of the cotton are of either the sea-island cotton or the land cotton. It is very difficult to obtain new varieties which have both characteristics such as high quality from the sea-island cotton and high-productivity from the land cotton. After ion implantation treatment of the normal hybrid or reciprocal hybrid F1 seeds, the variation coefficient becomes smaller and smaller. The character segregation degree continuously decreases and stabilizes as the number of generation increases. Up to the F4 generation, the variation degree (the ratio between the total variation coefficient and the F2-generation total variation coefficient) is only 10% whereas the variation degree of the control F4 generation (i.e. non ion-implanted hybrid F4) is 30%. This indicates that ion implantation can noticeably accelerate hereditary stability in the sea-land cotton hybrid. The reasons may be that ion implantation induces high-rate lagging chromosomes that are easily eliminated when forming gametes or/and ion implantation induced chromosomal displacement. These can accelerate the exchange of hereditary substances between sea and land hybrids and thereby speed up the hereditary stability.

4.3.3.4. Creation of aneuploids. Aneuploids which are the basic materials of plant genetic breeding play an important role in genetic analysis and crop improvement. In ion implanted wheat Premebi, tetraploid wheat and AR1 rye, chromosome lagging, unequal segregation, 3-pole segregation and early segregation are all observed. A large amount of chromosomal lagging can definitely induce changes in the chromosome number and thus possibly result in new idioplasms of aneuploid wheat.

Table 8 shows the types and rates of aneuploid wheat obtained by ion implantation. Aneuploid wheat is obtained from all M2 generations for three tested materials. After N^+ implantation with fluences of 3×10^{16} ions/cm^2 and

Table 8
Types and rates of aneuploid wheat obtained by N^+ implantation

Tested material	Control number of chromosomes	Ion fluence ($\times 10^{16}$ cm^{-2})	Number of samples examined	Number of chromosomes	Number and type of aneuploids		Rate (%)
Premebi	42	3	38	41	$2n-1$	2	5.26
		4	22	41	$2n-1$	1	4.55
AR1	18 (14R + 4B)	4	23	19 (15R + 4B)	$2n-1$	1	4.53
Tetra-ploidrye	28	1	27	27	$2n-1$	2	7.41
		2	29	29	$2n-1+2t$	1	3.45
		2	29	27	$2n-1$	2	6.89
		3	36	27	$2n-2+1t$	1	2.78
		3	36	27	$2n-1$	2	5.56
		3	36	26	$2n-2$	1	2.78
		4	33	26	$2n-2$	2	6.06
		4	33	27	$2n-1$	1	3.03
		4	33	29	$2n+1$	1	3.03

4×10^{16} ions/cm^2, monomers with the chromosome number 41 appear in wheat Premebi. In rye AR1 implanted with an ion fluence 4×10^{16} ions/cm^2, monomers with the number of chromosomes of 19 appear, 15 of them being normal chromosomes and 4 as B chromosomes which are obviously a trisome. In tetraploid rye, the aneuploids appear after implantation with four fluences. There are not only the numbers of chromosomes as 26, 27 and 29 but also telomeres. The appearance rate of aneuploids is between 3.03% and 7.41%. Compared to the control, the phenotypes of aneuploids are unchanged and the fruiting rate slightly decreases. In chromosome engineering, it is ideal that inside the cell a section of the gene vector (chromosome) that controls bad characteristics is cut and replaced with a section of chromosome that controls good characteristics. Currently this kind of operation inside the cell is not easy to do, but the appearance of wheat aneuploids such as monomers and nullisomes provides wheat chromosome engineering with easy-to-obtain and cheap original materials. In order to create wheat aneuploid materials, the normal way is to first have the original variety resources, and through hybridization. The transmitting breeding procedure of the aneuploids can then be accomplished. After hybridization, identification, selection, and breeding continuously for several generations, ion implantation induced variation of chromosome number provides breeding and developing aneuploid wheat with a new route.

4.3.4. New varieties bred by ion beam technology

Since 1997, ion beam biotechnology has been developed in some countries, particularly in China. There have been impressive accomplishments in biology and agriculture. Laboratories of ion beam bioengineering have been established in Chinese Academy of Sciences, Anhui, Xinjiang, Inner Mongolia, Shanxi, Hu'nan, He'nan, Jiangsu, Zhejiang Provinces in China, equipped with ion beam bioengineering devices (see Section 3). These laboratories have made great contributions to the development of agriculture and fermentation industry by means of ion beam breeding of plants and microorganisms. In Anhui Province, planting areas of the new crop varieties have expanded to over 2.36 million hectares and grain output has increased by more than 0.8 million tons in 2004. Table 9 lists some representative new varieties bred by ion beam technology in previous years. Among these new varieties, some have special characteristics and investigations have been performed.

Rice varieties of retaining fresh quality after long-term storage are bred, and authorized by He'nan and Hubei Provinces in 2006 (Table 9, Nos. 18 and 19). Rice is a staple diet in many parts of the world and its safe storage is very important. Many investigators have suggested that lipid degradation is responsible for the deteriorative changes during storage, and that the absence of lipoxygenase (LOX) in rice grains may reduce oxidative deterioration. A rapid

Table 9
Some new varieties bred by ion beam technology (data from the Committee for evaluating and approving of varieties of Anhui Province)

No.	Varieties	Main characteristic of new varieties (abbr. H. y. is high yield)	Organization for examining and approving of new varieties	Authorization time
1	Tomato Lu No. 7	H. y., big fruit	Shandong Province	1997
2	Soybean Jin No. 28	H. y., big grain	Shanxi Province	2004
3	Corn Wan No. 10	H. y., high sweet	Anhui Province	1999
4	Corn Wan No. 14	H. y., opposite leaves	Anhui Province	2000
5	Corn Wan No. 15	H. y., high sweet, opposite leaves	Anhui Province	2003
6	Wheat Wan No. 32	H. y., high resistance	Anhui Province	1997
7	Wheat Wan No. 43	H. y., resistant to smut	Anhui Province	1999
8	Wheat Wan No. 54	H. y., resistant disease	Anhui Province	2003
9	Rice Wan No. 20 (S9042)	H. y., short growth period, resistant to disease	Anhui Province	1994
10	Rice Wan No. 42 (D9055)	H. y., resistant to rice blast	Anhui Province	1994
11	Rice Wan No. 44	H. y., high quality	Anhui Province	1999
12	Rice Wan No. 45	H. y., resistant to disease	Anhui Province	1996
13	Rice Wan No. 48	H. y., resistant to rice fulgorid	Anhui Province	1999
14	Rice Wan No. 60	H. y., high quality, resistant to rice stripe disease	Anhui Province	2000
15	Rice Wan No. 71	H. y., resistance to coldness	Anhui Province	1999
16	Rice Wan No. 96	H. y., high quality	Anhui Province	2006
17	Rice Wan No. 143	H. y., direct sowing (no rice seedling planter)	Anhui Province	2005
18	Rice Fengyou 293	H.y., long-term storage	Henan Province	2006
19	Rice Zhongyou 292	H.y., long-term storage	Hubei Province	2006
20	Rice Wan No. 179	H. y., high quality, short growth period	Anhui Province	2006
21	Silkworm 991 × 992	H. y., thick fibre, high resistant to diseases	Anhui Province	2002

biochemical assay, which makes use of LOXs' coupled oxidation and an oxidation reduction indicator to induce a color reaction, has been developed to determine the LOX isoenzymes status (Chinese patent, ZL00112539.7) [327–329]. Using ion beam mutation, hybridization, back crossing, and tissue culture, several new rice lines D055, D055-7, D597 and D644 without the lipoxygenase isoenzymes (LOXs) have been bred. The approval of D055 as a standard new rice is pending approval (Publication No. CNA 000937E). D055-7 exhibits high yield and outstanding cold resistance, and is being evaluated as a standard crop. D597 and D644 also possess excellent agricultural characteristics, strong resistance to harsh environment, and good cooking and taste quality. These varieties integrate the genes for storage compatibility and excellent agricultural characteristics, thereby overcoming the drawbacks of early-season paddy rice that matures early but has low quality.

In a series of experiments, the quality of five rice varieties, either with or without lipoxygenase (LOX) isoenzymes, is assessed after storing for 42 months at room temperature, and accelerated aging experiments are also performed. The grain quality, germination percentage, and insect damage are investigated. In the varieties without LOX-1, 2, the rice quality is normal after storage, but for varieties with LOX-1, 2, the rice quality deteriorates. With increasing storage time, the germination rate of the seed for most varieties decreases greatly except for those without LOX-1, 2 which show no changes in the germination rate. During storage, there is also a significant difference in the degree of insect damage. In the varieties without LOX-3, insect damage is lower but in the varieties with LOX-3, insect damage is higher. It shows that the loss of LOX-1, 2 is probably the main factor that influences the lifetime of seeds and the absence of LOX-3 may be important to the insect resistance in rice grains [330]. The effect of the loss of lipoxygenase isoenzymes (LOXs) on the deterioration in seeds of soybean and maize are currently being investigated, with the aim of developing new species of soybean and maize without deterioration and development of a stale flavor during long-term storage. Preliminary results demonstrate that the maize varieties lacking LOX-1, 2 can retain higher vigor during accelerated aging than lines containing LOX-1, 2 [331].

The maize (*Zea Mays*) opposite mutant, characterized by decussate phyllotaxis and fruits throughout their life cycle, is very rare. It is of great theoretical and practical use to study the genetics, phylogeny, plant physiology, plant taxonomy, and breeding of maize. Chen et al. have obtained one opposite mutant of maize from the self-inbred line Yellow 48 by 30 keV N^+ implantation. It results in a straight opposite plant in further selection (Fig. 40) [332]. The leaf number and leaf area of opposite maize increase by almost a factor of two compared to that in other plants, but the mean leaf area of the opposite plant is lower than that of the alternate. The chlorophyll content in oppositifolious maize is found to be higher than that in the alternate plant. Measurements on the diurnal fluctuation of the transpiration rate and stomatic conductance and water use efficiency indicate that the oppositifolious maize can adapt to drought conditions better than the alternate [333]. The genes responsible for opposite phenotype are primarily localized by restriction fragment length polymorphism (RFLP) analysis to the short arm of the linkage group 2 (LG2) near the RFLP marker umc 34 [334]. Research by Tian and Cheng suggests that the opposite characteristic is controlled by three pairs of dominant genes and one pair of recessive genes [335]. By RFLP, the recessive site op4 is correlated to the fifth linkage group. Xie et al. have constructed one pair of near-isogenic lines (NILs), H14D and H53, and determined that the opposite phenotype is controlled by two independent, mutually complementary dominant genes O*pp-1* and *Opp-2*. Two markers ($S312_{377}$ and $S360_{602}$) are then identified by RAPD (Random amplified polymorphic DNA) to be

Fig. 40. Maize plants that show opposite (left) or alternate (right) pairs of leaves and fruits.

in linkage with *Opp-1* or *Opp-2*. These two markers are subsequently transformed to the more elaborate SCAR (the sequence characterized amplified region) markers, named CBJ1 and CBJ2 [336]. Recently, Tan and Cheng et al. have further identified several SSR (simple sequence repeat) markers: SSR umc2094 in Bin2.01 being linked to the opposite gene 1 (*Opp-1*) at a genetic distance of 6.7 cM, SSR bnlg 1831 in Bin2.06 being linked to the opposite gene 2 (*Opp-2*) at 6.1 cM, bnlg 1092 in Bin2.01 being linked with O*pp-1* at 12.2 cM, as well as bnlg 1887 and umc1028 in Bin2.06 being linked with *Opp-2* at 16.8 and 1.9 cM. These markers are useful for marker-assisted selection breeding and also provide the basis for separation and cloning of opposite genes [337]. To increase its value of opposite maize in practice, three varieties of sweet opposite maize have been bred through sequential ion beam mutation and hybridization, and authorized by Anhui Province in 2000, 2002, and 2003 (Table 9, Nos. 3–5).

4.4. Ion beam mutation breeding of microbes

Mutation is the fountainhead of genetic variation. Although hybridization induced gene recombination is one route to variation, mutation is more important. Without various mutation-induced allelomorphic genes enriching the gene pool, it would be impossible to talk about gene recombination. Inducing artificial mutation is an important means of accelerating mutation and the artificial rate can be thousands of times greater than the natural rate of mutation [338]. It is natural that artificial-mutation-based microbial breeding monopolizes germ breeding in the fermentation industry. At present, most of the various production strains of microbes used in the international and domestic fermentation industries are mutated strains [339]. In particular, almost all of the strains used in the antibiotic industry are mutant strains. Although genetic engineering is well developed for the improvement of strain species and there are numerous examples of good achievements, applications in production are not yet very extensive. Therefore studies on the mutation breeding of microorganisms with ion beam mutation have attracted more attention since microbe mutation was discovered in 1992.

4.4.1. Mutagenic effects of ion implantation into microbes [1]

After energetic ion implantation, microbes suffer from various kinds of effects such as damage to the morphology of large cells, changes in various subcellular structures, and modification of the biological macromolecules that compose the cells [96,340–345]. The damage affects the life activities of the microbe. When the genetic substance DNA is damaged, the corresponding DNA repair enzymes are activated to induce repair. However, it is inevitable that some errors occur and these can lead to genetic mutations.

When the inactivation level of both ion beam and ^{60}Co γ-ray radiation is adjusted to the same survival rates, it is found that in most cases, the mutation rate due to ion implantation is higher than γ-ray radiation. The rifampicin-resistant (Rif^r) mutation frequencies in *E. coli* induced by γ-ray radiation and energetic ion implantation are compared (Fig. 41) [96]. At the average 50% cell killing level, the mutation frequency of 10 keV N^+ implantation reaches

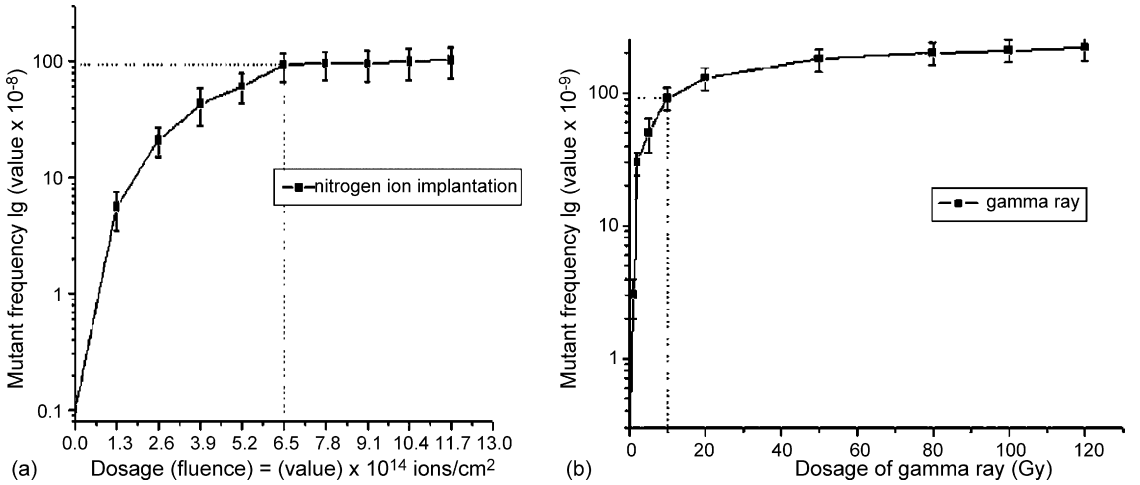

Fig. 41. Mutation frequencies of Rifr induced by (a) 10 keV N^+ implantation and (b) ^{60}Co-γ ray. Dotted lines indicate the ion fluence or ^{60}Co-γ ray dose with 50% survival fractions, at which points the Rifr mutation frequency by N^+ implantation is ∼10 times that by ^{60}Co-γ ray. Reprinted with permission from [96]. Copyright 2004 by Brazilian Society of Genetics.

9.5×10^{-7}, which is an order of magnitude higher than that of γ-ray (9.3×10^{-8}) (Fig. 41). The cascade damage caused by ions leads to atomic displacement and rearrangement or gene deletion of the genetic substance. Ion implantation induced damage also includes chemical damage resulting from recombination reactions between the ions, displaced atoms and matrix atoms, as well as transfer of electrons in the biomolecules due to charge exchange. A combination of mutations is more effective than a single mutation. Thus, it is not difficult to understand why in most cases, ion implantation of microbes results in higher mutation rate and efficiency than γ-ray radiation.

Experimental protocols have been developed with particular emphasis on the practical flexibility for ion bombardment and subsequent screening of mutants. Here, several points need to be considered. First of all, a homogeneous smear of a small quantity, normally 50–100 μl (approximately 10^6 to 10^8 cells/ml) of single-cell microbes or spores is required for ion bombardment in vacuum. For filiform fungi that do not produce spores, the bacteria should be mashed with glass beads beforehand. If a petri dish is used for growing the bacteria colonies, it can be simply placed inside the chamber for treatment but the culture medium must not be too thick. Secondly, the implantation fluence is normally an order of magnitude lower than that used in implantation of dry seeds. The optimal beam energy and fluence should be determined by experiments, namely, by plotting the survival rate of the treated microbes as a function of ion parameters. Thirdly, attention must be paid to the establishment and development of a fast, accurate, and convenient screening analysis. This has a large impact on the success of the screening work. Different methods are used at different stages of the screening process. For instance, as there are many samples in the primary screening, rough and simple detection methods can be used. In secondary screening, more precise determination methods should be adopted. Observation of the morphology of the implanted colonies is often used. High production mutations are usually related to morphology mutations. Before selection, high-production and low-production colonies should be studied. Thus, in the primary screening, those low-production strains can confidently be bypassed. This is equivalent to expanding the screening quantity. However, it should be noted that sometimes the grown colonies are morphologically irregular, and so special attention should be paid to natural segregation screening because high-production mutants often hide in the damaged colonies. Lastly, when new mutants are selected, the culture media and conditions should be frequently adjusted so that the selected strains can further display their potential. With regard to the culture media and conditions, several cross experiments can be performed to determine the optimal culture plan. Multiple ion implantation and screening can generate a small quantity of high-production mutations each time to achieve the breeding goal.

4.4.2. Application of ion beam mutation of microbes in fermentation industries

In the past decade, more than 30 strains have been treated by ion implantation. They include various microbial products, covering enzymes, vitamins, organic acids, antibiotic and amino acids, etc (Table 10). Many excellent mutants have been obtained from breeding experiments. Some of them have been transferred to the industry while the rest are still in the experimental stage. A few significant examples representing various sorts of bio-products with different functions and potentials are described in the following sections.

4.4.2.1. Xylanase by Aspergillus niger [346,347]. A class of enzyme produced by microorganisms is able to degrade the linear polysaccharide beta-1, 4-xylan into xylose, thus breaking down hemicellulose which accounts for 17–48% in most agricultural wastes such as corn cob, wheat straw, and wheat bran. Presently, xylanase is used for biobleaching in the pulp and paper industries and has the potential to transform those environmentally unfriendly agricultural wastes into valuable resources. However, the cost of production and low yields of xylanase of strains prevent large-scale industrial applications. Hence, obtaining high yield xylanase producing strains is imperative for efficient utilization of those natural substrates.

The fungal mutant strain, *A. niger* N218, is treated by a 10 keV 1–2 $\times 10^{15}$ ions/cm^2 nitrogen beam to produce a high yield, stable mutant strain, *A. niger* P602 after consecutive breeding selection. Its activity is constant throughout nine generations at an average of 6068 IU/g, which is in great contrast with 2989 IU/g of N218 (Fig. 42). Moreover, P602 displays a broader fermentation temperature range and shorter fermentation period than N218, indicating that the power consumption can be reduced in the summer season such that the efficiency is improved. These results suggest that the *A. niger* mutant strain bred by N^+ implantation is suitable for industrial production.

4.4.2.2. L-Ascorbic acid by Gluconobacter oxydans and Bacillus megaterium. Commonly known as Vitamin C, L-ascorbic acid is a water-soluble essential nutrient. It is the most widely taken nutritional supplement and usually

Table 10
List of industrial microbial strains improved by ion beam technology

	Products (Ref.)	Original strains	Improved strains, increment of enzyme activity or enzyme yield
Enzyme	Saccharifying enzyme [1]	*Aspergillus niger*	Up to 26,000 unit, 20% increment
	Proteolytic enzyme [378]	*Aspergillus oryzae* (3042-1)	TK-7, 36% increment
	Xylanase [346–347]	*Aspergillus niger* A3	N212, 600 units/ml, 100% increment
	Protopectinase [379]	*Aspergillus* sp. XZ-131	Z-25, 179% increment
	Cyclodextrin glucanotransferase [380]	*Bacillus alcalophilus*	>6000 units/ml, two folds increment
	SOD [381]	*Bacillus subtilis*	3429.3 units/g fresh cells, 88% increment
	α-acetolactate decarboxylase [382]	*Bacillus Licheniformis* BL391	HL115, 40% increment
	Alkaline chitinase [383]	*Streptomyces griseofuscus* S1001	Eβ 11, 16.5 units/ml, five times increment
	Xanthine oxidase [384]	*Arthorbacter globiformis* ATCC8010	43% increment
	Ubiquinone-10 [385]	*Agrobacterium tumefaciens* ATCC4452	CPM7503 with ubiquinone-10 yield 405 mg/l, 70% increment
	Chitosanase [386]	*Bacillus* sp. S65	S65F5, from 4.1 U/ml to 25 U/ml, fermentation time from 72 to 56 h
Vitamins	Vitamins C [356–358]	*Gluconobacter oxydans* and *Bacillus megaterium*	BG112-302, transformation rate increased from 79.3% to 94.5%
	Ergosterol [387,388]	*Saccharomyces cerevisia* YE1	YA1, YA2, 55–60% increment
Organic acids and amino acids	L-Lactic acid [361,362]	*Rhizopus oryzae* PW352	RLC41-6, 133 g/L, 75% increment
	L-Lactic acid [363]	*Lactobacillus casei* L110Z	L110Z5, 18% increment
	L-Lactic acid [364]	*Bacillus coagulans*	RS12-6C, 117 g/L, 10% increment
	L-Phenylalanine [389]	*E. coli*	17.1 g/L, 23% increment
	Decane dicarboxylic acid [390]	*Candida tropicalis*	SCB609, 73.2 g/L with 15% *n*-dodecane
	Itaconic acid [391]	*Aspergillus terreus* A9003	60.1% conversion rate at 30 L fermentation volume
	Itaconic acid [392]	*Aspergillus terreus* T730	HA8, 61.3% conversion rate, 74% increment
	Glutamic acid [393–394]	*Corynebacteriaceae* D110	D5221 and B3263, 35%, 25% increment, respectively
	Polysialic acid [395]	*E. coli*	JYL-1, 3100 μg/ml
Antibiotics	Zhijiang bacterin [396]	*Streptomyces roseoflavus* 93-15-32	97–49, up to 905 g/mL, four-folds increment
	Rifamycin [1]	*Nocardia mediterranei*	Up to 6800 units, 35% increment
	Oxytetracyline [397]	*Streptomycesr imosus* 98-4-48	In 57 m^3 fermenter, 3.42% increment
	Aureonuclemycin [398]	JH-926	Up to 3902 mg/L, 13.89% increment
	Gentemicin [399]	Provided by hebei pharmaceutical manufacture	27% increment
	Spectinomycin [400]	*Streptomyces spectabilis* 1043	102.3% increment
	Rifamycin [401]	*Nocardia mediterrane* A606	A606-3-1, up to 7890 units, 58.7% increment
	Penicillin [402]	*Penicillium chrysogenum* 18-101	18-104-31, up to 59,175 units/ml, 11.8% increment
	Streptomycin [403]	*Streptomyces erythreus*	From 4015 to 5531 μg/ml
Others	Arachidonic acid [370–372]	*Mortierelle alpine*	149-N18, 5.11 g/L AA yield, 1.26-fold higher
	Anti-fungi lipopeptide [375–377]	*Bacillus subtitles* JA	JA-026, 14.3% increment of inhibitory activity
	Red pigment [404]	*Monascus*	38.1% increment of red pigment yield
	Carotenoid [405]	*Rhodotorula* RY-3	RY-3-9, 76.2% increment of carotenoid yield

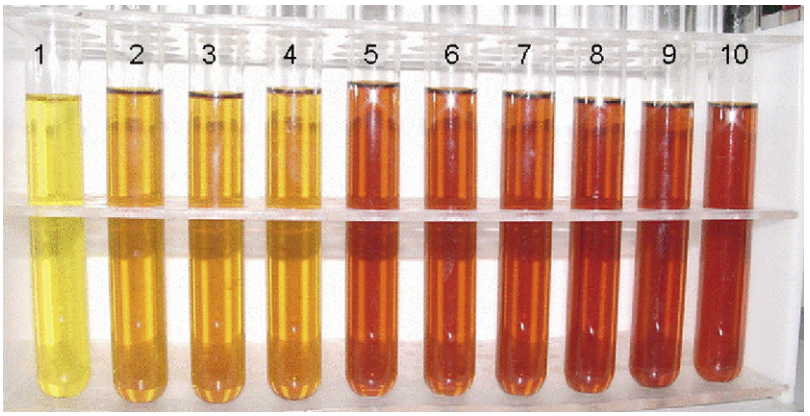

Fig. 42. Enzymatic activity test of original and ion beam mutated xylanase producing strains. (1) Control tube without bacteria; (2–4) original strain showing basic levels of xylanase activity; (5–10) mutated strains showing increased enzymatic activity.

provided in tablets and an additive to food and beverages. Production of L-ascorbic acid has become a big industry. The first method to produce L-ascorbic acid in a commercial scale was developed by Reichstein and Grussner [348,349] using a single biocatalysis step. Compared to chemical synthesis, a microbial process to produce L-ascorbic acid is more economical and ecologically greener [350]. A two-step fermentation process to manufacture L-ascorbic acid on a large scale has been developed using a mixed culture of *G. oxydans* and *B. megaterium* [351,352]. The process takes advantage of the enhanced yield of the key intermediate 2-keto-L-gulonic acid (2-KLG) when *G. oxydans* are mixed with *B. megaterium* or other microbes [353,354]. However, the transformation rate from L-sorbose to 2-KLG used to be only about 75–80%, although various mutagenic efforts were made to improve the efficiency [355].

About ten years ago, the two original strains, *G. oxydans* (GO29) and *B. megaterium* (BM80) were subjected to ion beam mutation for screening of high-yield strains. Both original strains were implanted separately with H^+ or N^+ of various fluences. The implanted GO29 and BM80 were then matched randomly and cultured with its counterpart strain BM80 or GO29, respectively. The yields of 2-KLG in the mixed culture broth were measured by iodometry. The transformation rate was determined by the ratio of the gram-molecule yield of 2-KLG and the concentration of sorbose added to the culture broth. After subculture for eight passages in agitated flasks, the average transformation rate of GB112-302 (mixed BM-GO) bred by ion beam in gram-molecule increased from 79.3% to 94.5% [356–358]. This high-yield strain has been transferred to the industry and even on the commercial scale. The transformation rate is stable at 92.0%, indicating that a producer can get 0.99 kg of gulonic acid from 1.0 kg of sorbose.

4.4.2.3. Lactic acid by Rhizopus oryzae. Together with its salt derivatives, lactic acid is one of the most widely used organic acids in the food, pharmaceutical, textile, and leather industries. In particular, L(+)-lactic acid is an excellent substrate for the synthesis of poly lactic acid (PLA), which is a potential environmental friendly and biodegradable plastic [359]. The fungus, *R. oryzae* can produce L(+)-lactic acid from starch [360], but the yield is relatively low.

Ion beam mutation of *R. oryzae* has been practiced on the wild strain PW352 and two mutants, RE3303 and RF9502, are isolated [361]. After culturing for 36 h in agitated flasks, the concentration of lactic acid reaches 131–136 g/L and the conversion rate from glucose to lactic acid attains 86–90%. The productivity is 3.61 g/L h which is 75% higher than the production yield of the wide type strain. Moreover, the temperature range of RE9502 for optimum fermentation is widened. On the other hand, another mutant strain RF3608 using glucose as the carbon source is isolated. To further lower the production cost, liquid corn starch is used as the carbon source for the strain RF3608, and mutation breeding is conducted using ion implantation. At the present time, the lactic acid yield of the newly obtained strain, RLC41-6, is equivalent to that produced by lactic acid bacteria. Under the optimal conditions (150 g/L liquid corn starch, 2 g/L $(NH_4)_2SO_4$), the fermenting strain is capable of producing 133–137 g/L after 36 h of fermentation at 38 °C, indicating a potential for large-scale industrial manufacturing [362]. Furthermore, *Lactobacillus casei* L110Z and *Bacillus coagulans*, another two strains that are capable of producing L-lactic acid have also been mutated by ion implantation and new strains with increased yield of lactic acid of 10–18% have been reported [363,364].

4.4.2.4. Arachidonic acid by Mortierelle alpine. Arachidonic acid or 5, 8, 11, 14-eicosatetraenoic acid is an essential dietary component for human beings and a precursor of many important eicosanoids such as prostaglandins, thromboxanes, and leukotrienes [365]. Because of its various physiological functions and important contribution to the development of infant's brain [366], industrial-scale production of AA has attracted much attention. Although it is common in animals, the extremely low yield of AA of 0.2% (A, B) or lower [367] makes it impractical to isolate sufficient AA on a large scale from natural sources. The alternative is to produce polyunsaturated fatty acids (PUFAs) such as AA by fermentation with fungi [368].

Mutation breeding and fermentation studies of AA produced by *M. alpine* have been attempted. By 10 kV, 3×10^{14} ions/cm^2 N^+ implantation, 149-N18, a high-yield AA producing strain, has been screened out with an arachidonic acid yield of 4.66 g/L that is about two times higher than that of the original strain. This strain is then transferred to a 50-tonnes fermenter to evaluate the commercial potential [369,370]. The results show that the biomass, lipid in biomass, and arachidonic acid in lipids, and arachidonic acid yields are 2.64 g/100 ml, 40.5% (w/w), 47.98% (w/w) and 5.11 g/L, respectively, indicating a similar or even better productivity compared to those in the laboratory. Gas chromatography/mass spectrometry (GC/MS) shows that the oil contains 80% of polyunsaturated acids such as arachidonic acid, γ-linolenic acid and linoleic acid [371,372].

4.4.2.5. Anti-fungi lipopeptide by Bacillus subtitles JA. Biological pesticides are thought to be potential substitutes for chemically synthesized pesticides. Extensive efforts have been devoted to the study, development, and application of safe and efficient pest control *via* natural biological pathways. The *Bacillus subtilis* strains can produce a broad spectrum of antagonistic compounds and so possesses a natural fungicidal activity. Some of the strains or their metabolites have been employed as biological control agents such as the *B.* subtilis strain QST 713 (marketed as QST 713 or Serenade^{TM}) [373,374].

B. subtitles JA produces an abundant amount of antifungal substances that exhibit strong inhibitory activity against various fungi and bacteria which are pathogenic to plants and human beings such as *Rhizoctonia solani*, *Fusarium graminerarum*, *Pseudomonas solanacearum*, *Trichophyton rubrum*. After N^+ implantation, a mutant strain, B subtitles JA-026 with a higher antifungal activity, has been screened and obtained [375]. Preliminary experiments indicate that the antifungal substances are thermally stable and partially sensitive to proteinases K and tryproteinase. The fermentation broth is then precipitated with 70% ammonium sulfate, and it is found that the inhibitory activity of precipitation increases while the supernatant loses this activity, implying that the antifungal substances are likely to be peptides or proteins. Activity tests of culture filtrates from JA-026 against the indicating organisms, *A. niger* and *Gibberella zeae*, display a 14.3% enhancement in the inhibitory activity as manifested by the enlarged area of inhibition zone on the indicator plates [376]. The culture filtrates from JA-026 are subjected to multi-step purification using anion exchange, column chromatography, and FPLC (fast protein liquid chromatography). Three types of antimicrobial lipopeptides, namely AFP1, AFP2 and AFP3, are obtained and all display strong inhibitory activity against *R. solani* and *Fusarium graminearum*. By MALDI-TOF and ESI (electrospray ionization) mass spectrometry analyses, the molecular weights of these three peptides are determined to be 1462.645, 1476.39, and 1490.53 Da, respectively, and they are identical to those produced by the wild-type strain. These properties suggest that the mutant strain is a promising bio-control candidate in agriculture (Fig. 43) [377].

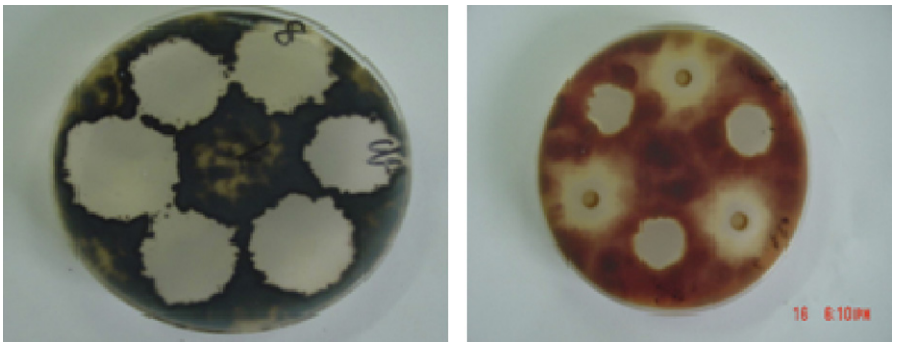

Fig. 43. Antifungal tests of *B. subtitles* JA-026 against *Rhizoctonia solani* (left) and *Fusarium graminearum* (right). The white circles indicate that the bacteria in this areas are killed by the addition of fermentation media from *B. subtitles* JA-026.

In summary, ion implantation has been proven to be a highly efficient mutagenic means for microorganism breeding in many commercial applications. This is achieved by its higher mutation rate, broader mutation spectrum, and mild inactivation effects compared to most conventional mutation sources like X-, γ-rays, and high-energy ion beams. In comparison with chemical mutagenesis, implantation of ions like N^+ and H^+ which are constituent elements in living systems eliminate the potential health and environmental hazards. In terms of its applicability and feasibility, keV ion beams can be generated by a straightforward bench-top instrument at low cost, and the instrumentation is much simpler than large-scale accelerators required by high-energy beams or complex radiation shielding components for X-ray or neutron machines. Miniaturized ion beam machines are being developed for microorganism mutation breeding.

5. Conclusion

Energetic ion implantation of complex biological material exists in nature. Energetic ions in the environment can be implanted into biological cells, and affect the character of organisms, the evolution of life, and the health of human beings. This article presents an overview of keV ion interaction with biomolecules and organisms. The study of ion interaction with non-living materials and its application in physical, material and biomedical research in the past century are briefly retrospected. Encouraged by the successful development of ion beam modification of materials, investigation of the interaction between implanted ions and complex biological systems was initiated over twenty years ago and has been the subject of active research in a few countries. Recent progress in both fundamental and application research of this original yet young area is discussed in detail in this report. Updated practical achievements in agriculture and fermentation industry are presented with a number of examples. Mechanism study on low-energy ion collision with critical biological molecules at various scales has provided new evidence for DNA damage induced by extremely low-energy ion tracks which are ubiquitous in a variety of radiation events. In contrary to inorganic materials, chemical reactions between incident ions and target atoms/molecules play an important role in ion collision induced bio-effects in organisms. A large amount of data has been obtained supporting that formation of biogenic species in simple targets by energetic ion implantation is one of the pathways for life origin in the universe. Radiation damage to bulk organisms due to the implanted ion deposition in cells as well as the deposited ions themselves has been closely examined. Determined by the unique structural frame of biological systems, a different penetrating profile of implanted ions in living material has been experimentally manifested as compared to conventional non-porous solid materials. The technique issues pertaining ion implantation of living material is discussed and methodology approaches developed for this purpose are presented also. Ion beam genetic modification of plants and microbes is now a well-established mutation breeding technique, by which many new crop varieties and microbe strains have been bred and are currently used in practice. Gene delivery assisted by ion beams has found successes in the bacteria *E. coli* and several plant species. Delivery of gene clusters by ion beams is a promising ways for hybridization of different plant species by breaking through the limitation of progeny incompatibility of distant crossing varieties. Future study includes further improvement of instrument and methodology for study of ion interaction with living materials, investigation of the primary interaction process and physical model of energetic ion interaction with complex biological systems, and analyses and processing of living materials by high-precision ion beams as that generated by focused ion beam or single-particle beam lines.

Acknowledgements

The authors are grateful to Drs. Yuejin Wu, Beijiu Cheng, Shaobing Gu, Lianyun Chen, Wei Wang, Po Bian, Kejian Ding and Mingli Tang for assistance in the preparation of the manuscript. We acknowledge financial support from Hong Kong Research Grants Council (RGC) Competitive Earmarked Research Grant (CERG) No. CityU 1120/04E, City University of Hong Kong Applied Research Grant No. 9667002, and Chinese Academy of Sciences (Project KSCX2-SW-324).

References

[1] Z.L. Yu, L.D. Yu, I.G. Brown, Introduction to Ion Beam Biotechnology, Springer-Verlag, NewYork, 2005 (English edition);
Z.L. Yu, L.D. Yu, I.G. Brown, Introduction to Ion Beam Biotechnology, Anhui Sci. & Tech. Press, Hefei, 1998 (Chinese edition).

[2] R.B. Decker, S.M. Krimigis, T.P. Armstrong, C.J. Mosley, D.C. Hamilton, G. Gloeckler, Adv. Space Res. 32 (2003) 591.
[3] R.B. Decker, S.M. Krimigis, Adv. Space Res. 32 (2003) 597.
[4] V. Grill, J.W. Shen, C. Evans, R. Graham Cooks, Rev. Sci. Instrum. 72 (2001) 3149.
[5] H. Geissel, H. Weick, C. Scheidenberger, R. Bimbot, D. Gardes, Nucl. Instrum. Methods Phys. Res. B 195 (2002) 3.
[6] L. Hanley, S.B. Sinnott, Surf. Sci. 500 (2002) 500.
[7] J.F. Ziegler (Ed.), Ion Implantation: Science and Technology, Academic Press, San Diego, 1988.
[8] H. Gnaser, Low-Energy Ion Irradiation of Solid Surfaces, Springer-Verlag, Heidelberg, 1999.
[9] J. Linhard, M. Scharff, H.E. Schiott, Kgl. Dan. Vid. Selsk. Mater. Fys. Medd. 33 (1963) 14.
[10] J. Lindhard, A.H. Sorensen, Phys. Rev. A 53 (1996) 2443.
[11] J.F. Ziegler, J.P. Biersack, U. Littmark, The Stopping and Range of Ions in Solids, Pergamon Press, New York, 1984, http://www.srim.org.
[12] P.K. Chu, in: C.R. Brundle, C.A. Evans, Jr., S. Wilson (Eds.), Encyclopedia of Material Characterization, Butterworth-Heinemann, 1992, pp. 532–548 (Chapter 10.1).
[13] J.R. Bird, J.S. Williams, Ion Beams for Material Analysis, Academic Press, Marrickville, Australia, 1989.
[14] D.R. Clarke, S. Suresh, I.M. Ward, FRS Ion–solid Interactions: Fundamentals and Applications, Cambridge Univ. Press, Cambridge UK, 1996.
[15] F.Z. Cui, Z.S. Luo, Surf. Coat. Technol. 112 (1999) 278.
[16] P.K. Chu, S. Qin, C. Chan, N.W. Cheng, L.A. Larson, Mater. Sci. Eng. R 17 (1996) 207.
[17] A. Garg, E. Kokkoli, IEEE Eng. Med. Biol. (2005) 87.
[18] S. Prasad, J. Quijano, Biosens. Bioelectron. 21 (2006) 1219.
[19] P.K. Chu, J. Vac. Sci. Technol. B 22 (2004) 289.
[20] X.Y. Liu, P.K. Chu, C.X. Ding, Mater. Sci. Eng. R 47 (2004) 49.
[21] B.D. Ratner, A.S. Hoffman, F.J. Schoen, J.E. Lemons, Biomaterial Science: An Introduction to Material in Medicine, vol. 2, Academic Press, New York, 1996.
[22] S.I. Stupp, P.V. Braun, Science 277 (1997) 1242.
[23] J. Enderle, S. Blanchard, J. Bronzino, Introduction to Biomedical Engineering, Academic Press, New York, 1999, p. 538.
[24] I.G. Brown, K.A. Bjornstad, E.A. Blakely, J.E. Galvin, O.R. Monteiro, S. Sangyuenyongpipat, Plasma Phys. Contr. Fusion 45 (2003) 547.
[25] C.L. Klein, M. Scholl, A. Maelicke, J. Mater. Sci.: Mater. M 10 (1999) 721.
[26] J.L. Li, D. Stein, C. McMullan, D. Branton, M.J. Aziz, J.A. Golovchenko, Nature 412 (2001) 167.
[27] D. Hill, Design Engineering of Biomaterial for Medical Devices, Wiley, London, 1998, pp. 1–8.
[28] M.A. Correa-Duarte, N. Wagner, J. Rojas-Chapana, C. Morsczeck, M. Thie, . Giersig, Nano Lett. 4 (2004) 2233.
[29] R.W.Y. Poon, J.P.Y. Ho, C.M.Y. Luk, X.Y. Liu, J.C.Y. Chung, P.K. Chu, K.W.K. Yeung, W.W. Lu, K.M.C. Cheung, Nucl. Instrum. Methods Phys. Res. B 242 (2006) 270.
[30] C.L. Chu, C.Y. Chung, P.K. Chu, Mater. Sci. Eng. A: Sturct. 417 (2006) 104.
[31] U. Lindh, Nucl. Instrum. Methods Phys. Res. B 104 (1995) 285.
[32] R.D. Macfarlane, Braz. J. Phys. 29 (1999) 415.
[33] S. Schurch, E. Bernal-Mendez, C.J. Leumann, J. Am. Soc. Spectrom. 13 (2002) 936.
[34] L.J. Wu, G. Randers-Pehrson, A. Xu, C.A. Waldren, C.R. Geard, Z.L. Yu, T.K. Hei, Proc. Natl. Acad. Sci. USA 96 (1999) 4959.
[35] W.F. Morgan, M.B. Sowa, Proc. Natl. Acad. Sci. USA 102 (2005) 14127.
[36] N. Dennis, Science 278 (1997) 1884.
[37] B. Jones, N. Burnet, Br. Med. J. 330 (2005) 979.
[38] J.R. Williams, Y.G. Zhang, H.M. Zhou, M. Osman, D. Cha, R. Kavet, F. Cuccinotta, J.F. Dicello, L.E. Dillehay, Mutat. Res.: Fund. Mol. M 430 (1999) 255.
[39] R.W. Court, M.A. Sephton, J. Parnell, I. Gilmour, Geochim. Cosmochim. Acta 70 (2006) 1020.
[40] M. Tuleta, L. Gabla, J. Madej, Phys. Rev. Lett. 87 (2001) 078103.
[41] D. Lario, B. Sanahuja, A.M. Heras, Adv. Space Res. 15 (1995) 389.
[42] M. Tuleta, L. Gabla, A. Szkarlat, Europhys. Lett. 70 (2005) 123.
[43] L.V. Vaeck, A. Adriaens, R. Gijbels, Mass Spectrom. Rev. 17 (1999) 1.
[44] A. Adriaens, L.V. Vaeck, F. Adams, Mass Spectrom. Rev. 17 (1999) 48.
[45] B.J. Garrison, J. Am. Chem. Soc. 104 (1982) 6211.
[46] S. Bouchonnet, J.-P. Denhez, Y. Hoppilliard, C. Mauriac, Anal. Chem. 64 (1992) 743.
[47] D.M. Cannon Jr., N. Winograd, A.G. Ewing, Annu. Rev. Biophys. Biomol. Struct. 29 (2000) 239.
[48] A. Wucher, S. Sun, C. Szakal, N. Winograd, Anal. Chem. 76 (2004) 7234.
[49] T. Schenkel, K.J. Wu, Int. J Mass Spectrom. 229 (2003) 47.
[50] L. Hanley, P.D. Edirisinghe, W.F. Calaway, I.V. Veryovkin, M.J. Pellin, J.F. Moore, Proceedings of the SIMS XV, September 2005. Appl. Surf. Sci. 252 (2006) 6723.
[51] D. Drobne, M. Milani, M. Ballerini, A. Zrimec, F. Tatti, K. Draslar, J. Biomed. Opt. 9 (2004) 1238.
[52] J.-L. Guerquin-Kern, F. Hillion, J.-C. Madelmont, P. Labarre, J. Papon, A. Croisy, Biomed. Eng. Online 3 (2004) 10.
[53] R. Peteranderl, C. Lechene, J. Am. Soc. Mass Spectrom. 15 (2004) 478.
[54] Institute for Atomic and Molecular Physics, The Netherlands, IBA-Amolf_visitorsguide, from http://www.amolf.nl/.
[55] C. von Sonntag, The chemical Basis for Radiation Biology, Taylor and Francis, London, 1987.
[56] M.D. Sevilla, D. Becker, M. Yan, S.R. Summerfield, J. Phys. Chem. 95 (1991) 3409.
[57] L. Sanche, Mass Spectrom. Rev. 21 (2002) 349.

[58] B. Boudaiffa, P. Cloutier, D. Hunting, M.A. Huels, L. Sanche, Science 287 (2000) 1658.
[59] R. Lee, S. Yamada, N. Yamamoto, T. Miyamoto, K. Ando, M. Durante, H. Tsujii, J. Radiat. Res. 45 (2004) 195.
[60] T. Miyamoto, N. Yamamoto, H. Nishimura, M. Koto, H. Tsujii, J. Mizoe, T. Kamada, H. Kato, S. Yamada, S. Morita, K. Yoshikawa, S. Kandatsu, T. Fujisawa, The Working Group for Lung Cancer, Radiother. Oncol. 66 (2003) 127.
[61] P. Gastelblum, M. Roelandts, P.V. Houtte, Eur. Urol. Suppl. 5 (2006) 487.
[62] Z.W. Deng, I. Bald, E. Illengerger, M.A. Huels, Phys. Rev. Lett. 95 (2005) 153201.
[63] Z.W. Deng, M. Imhoff, M.A. Huels, J. Chem. Phys. 123 (2005) 144509.
[64] H. Jung, K. Kurzinger, Radiat. Res. 36 (1968) 369.
[65] D.E. Watt, S. Hughes, Phys. Med. Biol. 17 (1972) 306.
[66] W. Gunthera, W. Heinrich, F. Flesch, G. Reitz, Radiat. Meas. 34 (2001) 245.
[67] F. Antonelli, M. Belli, A. Campa, A. Chatterjee, V. Dini, G. Esposito, B. Rydberg, G. Simone, M.A. Tabochini, Adv. Space Res. 34 (2004) 1353.
[68] G. Kraft, in: F.J. Currell (Ed.), The Physics of Highly and Multiply Charged Ions, Kluwer Academic Publisher, 2002.
[69] F.A. Cucinotta, Radiat. Meas. 30 (1999) 261.
[70] O.V. Belyakov, S.A. Mitchell, D. Parikh, G. Randers-Pehrson, S.A. Marino, S.A. Amundson, C.R. Geard, D.J. Brenner, Proc. Natl. Acad. Sci. U.S.A. 102 (2005) 14203.
[71] J.B. Little, Carcinogenesis 21 (2000) 397.
[72] T.B. McCord, R.W. Carlson, Science 278 (1997) 271.
[73] G. Strazzulla, G. Leto, O. Gomis, M.A. Satorre, Icarus 164 (2003) 163.
[74] R.W. Carlson, R.E. Johnson, Science 286 (1999) 97.
[75] L. Moroz, G. Baratta, G. Strazzulla, L. Starukhina, E. Dotto, M.A. Barucci, G. Arnold, E. Distefano, Icarus 170 (2004) 214.
[76] C.F. Chyba, Nuture 403 (2000) 381.
[77] R.W. Carlson, M.S. Anderson, R.E. Johnson, W.D. Smythe, A.R. Hendrix, C.A. Barth, L.A. Soderblom, G.B. Hansen, T.B. McCord, J.B. Dalton, R.N. Clark, J.H. Shirley, A.C. Ocampo, D.L. Matson, Science (1999) 2062.
[78] R.A. Baragiola, M.J. Loeffler, U. Raut, R.A. Vidal, C.D. Wilson, Radiat. Phys. Chem. 72 (2005) 187.
[79] Z.L. Yu, IEEE Trans. Plasma Sci. 28 (2000) 128.
[80] Z.L. Yu, J.G. Deng, J.J. He, Nucl. Instrum. Meth., B 59/60 (1991) 705.
[81] L.F. Wu, Z.L. Yu, Radiat. Environ. Biophys. 40 (2001) 53.
[82] Z.L. Yu, Y.J. Wu, J.G. Deng, J.J. He, J. Zhou, Anhui Agricult. Sci. 16 (1989) 9 (in Chinese).
[83] T. Konishi, N. Yasuda, A. Takeyasu, S. Ishizawa, T. Fujisaki, K. Matsumoto, Y. Furusawa, Y. Sato, K. Hieda, Rev. Sci. Instrum. 76 (2005) 114302.
[84] M.E. Itoiz, B. Molinari, O. Bernaola, E.L. Kreimann, G. Saint-Martin, A.E. Schiwint, Radiat. Environ Biophys. 41 (2002) 257.
[85] S. Matsumoto, B. Goto, M. Furuse, T. Kanai, F. Soga, Nucl. Instrum. Meth., B 139 (1998) 372.
[86] A.M. Belu, D.J. Graham, D.G. Castner, Biomaterial 24 (2003) 3635.
[87] M.L. Pacholski, N. Winograd, Chem. Rev. 99 (1999) 2977.
[88] J.-L. Guerquin-Kern, T.D. Wu, C. Quintana, A. Croisy, BBA-Gen. Subjects 1724 (2005) 228.
[89] A. Daskalova, W. Husinsky, Plasma Process. Polym. 3 (2006) 257.
[90] D.F. Hunt, C.E. Hignite, K. Biemann, Biochem. Biophys. Res. Commun. 33 (1968) 378.
[91] E. Nordhoff, F. Klrpekar, P. Roepstorff, Mass Spectrom. Rev. 15 (1996) 67.
[92] S. Schurch, E. Bernal-Mendez, C.J. Leumann, J. Am. Soc. Mass Spectrom. 13 (2002) 936.
[93] J. Wang, J. Liu, X. Wang, J. Yao, Z. Yu, Lett. Appl. Microbiol. 39 (2004) 98.
[94] B. Rydberg, Int. J. Radiat. Biol. 47 (1985) 57.
[95] Y. Chen, B.Y. Jiang, Y.S. Chen, X.Z. Ding, X.H. Liu, C.S. Chen, X.Y. Guo, G.L. Yin, Radiat. Environ. Biophys. 37 (1998) 101.
[96] C.X. Xie, A. Xu, L.J. Wu, J.M. Yao, J.B. Yang, Z.L. Yu, Genet. Mol. Biol. 27 (2004) 284.
[97] D. Michael, P. O'Neill, Science 287 (2000) 1603.
[98] P. Das, G.B. Schuster, Proc. Natl. Acad. Sci. U.S.A. 102 (2005) 14227.
[99] H. Luna, E.C. Montenegro, Phys. Rev. Lett. 94 (2005) 043201.
[100] A.L. Lane, R.M. Nelson, D.L. Matson, Nature 292 (1981) 38.
[101] J.F. Copper, R.E. Johnson, B.H. Mauk, H.B. Garret, N. Gehrels, Icarus 149 (2001) 133.
[102] G.H. Olivera, C. Caraby, P. Jardin, A. Cassimi, L. Adoui, B. Gervais, Phys. Med. Biol. 43 (1998) 2347.
[103] P. Sobocinski, Z.D. Pesic, R. Hellhammer, N. Stolterfoht, B. Sulik, J.-Y. Chesnel, J. Phys. B: At. Mol. Opt. Phys. 38 (2005) 2495.
[104] C. Giustranti, S. Rousset, E. Balanzat, E. Sage, Biochimie 82 (2000) 79.
[105] Z.D. Pesic, J.-Y. Chesnel, R. Hellhammer, B. Sulik, N. Stolterfoht, J. Phys. B: At. Mol. Opt. Phys. 37 (2004) 1405.
[106] J.A. LaVerne, Nucl. Instrum. Meth. B 107 (1996) 302.
[107] C. Ferradini, J.P. Jay-Gerin, Can. J. Chem. 77 (1999) 1542.
[108] A. Appleby, H.A. Schwarz, J. Phys. Chem. 73 (1969) 1937.
[109] J.A. LaVerne, R.H. Schuler, J. Phys. Chem. 89 (1985) 4171.
[110] J.A. LaVerne, Radiat. Res. 118 (1989) 201.
[111] J.A. LaVerne, H. Yoshida, J. Phys. Chem. 97 (1993) 10720.
[112] G. Baldacchino, D. Le Parc, B. Hickel, M. Gardes-Albert, Radiat. Res. 149 (1998) 128.
[113] Y. Frongillo, M.J. Fraser, V. Cobut, T. Goulet, J.P. Jay-Gerin, J.P. Patau, J. Chim. Phys. 93 (1996) 93.
[114] V. Cobut, Y. Frongillo, J.P. Patau, T. Goulet, M.-J. Fraser, J.-P. Jay-Gerin, Radiat. Phys. Chem. 51 (1998) 229.
[115] Y. Frongillo, T. Goulet, M.-J. Fraser, V. Cobut, J.P. Patau, Radiat. Phys. Chem. 51 (1998) 245.

[116] B. Gervais, M. Beuve, G.H. Olivera, M.E. Galassi, Radiat. Phys. Chem. 75 (2006) 493.
[117] S. Uehara, H. Nikjoo, J. Radiat. Res. 47 (2006) 69.
[118] N.J.B. Green, M.J. Pilling, S.M. Pimblot, P. Clifford, J. Phys. Chem. 94 (1990) 251.
[119] U. Werner, K. Beckord, J. Becker, H.O. Lutz, Phys. Rev. Lett. 74 (1995) 1962.
[120] F. Alvarado, R. Hoekstra, T. Schlatholter, J. Phys. B: At. Mol. Opt. 38 (2005) 4085.
[121] B. Seredyuk, R.W. McCullough, H. Tawara, H.B. Gilbody, D. Bodewits, R. Hoekstra, A.G.G.M. Tielens, P. Sobocinski, D. Pesic, R. Hellhammer, B. Sulik, N. Stolterfoht, O. Abu-Haija, E.Y. Kamber, Phys. Rev. A 71 (2005) 022705.
[122] F. Gobet, B. Farizon, M. Farizon, M.J. Gaillard, M. Carre, M. Lezius, P. Scheier, T.D. Mark, Phys. Rev. Lett. 86 (2001) 3751.
[123] E.C. Montenegro, H. Luna, Braz. J. Phys. 35 (2005) 927.
[124] C.S. Lee, M.C. Chueh, Y.C. Liu, C.-Y. Hsu, S.H. Liu, W.H. Ip, S. Lee, Nucl. Instrum. Meth. B 240 (2005) 345.
[125] G.A. Baratta, M. Domingo, G. Ferini, G. Leto, M.E. Palumbo, M.A. Satorre, G. Strazzulla, NIMB 209 (2003) 283.
[126] G.A. Baratta, M.E. Palumbo, G. Strazzulla, Astron. Astrophys. 357 (2000) 1045.
[127] W.L. Brown, L.J. Lanzerotti, J.M. Poate, W.M. Augustyniak, Phys. Rev. Lett. 40 (1978) 1027.
[128] R.A. Baragiola, R.A. Vidal, W. Svendsen, J. Schou, M. Shi, D.A. Bahr, C.L. Atteberrry, Nucl. Instrum. Meth. B 209 (2003) 294.
[129] B.D. Teolis, R.A. Vidal, J. Shi, R.A. Baragiola, Phys. Rev. B 72 (2005) 245422.
[130] A. Plonka, W. Szajdzinska-Pietek, J. Bednarek, A. Hallbrucker, E. Mayer, Phys. Chem. Chem. Phys. 2 (2000) 1587.
[131] R.A. Baragiola, Planet. Space Sci. 51 (2003) 953.
[132] O. Gomis, M.A. Satorre, G. Strazzulla, G. Leto, Planet. Space Sci. 52 (2004) 371.
[133] R.E. Johnson, in: B. Schmitt, C. De Bergh, M. Festou (Eds.), In Solar System Ices,, Kluwer Academic Press, The Netherlands, 1998.
[134] J.P. Bibring, F. Rocard, Adv. Space Res. 4 (1984) 103.
[135] M.J. Loeffler, U. Raut, R.A. Vidal, R.A. Baragiola, R.W. Carlson, Icarus 180 (2006) 265.
[136] J. Ruiz-Laguna, C. Pueyo, Mutagenesis 14 (1999) 95.
[137] M. Kruszewski, M.H. Green, J.E. Lowe, I. Szumiel, Mutat Res. 16 (1994) 233.
[138] B. Epe, Rev. Physiol. Biochem. Pharmacol. 127 (1995) 223.
[139] A. Radschuweit, H.H. Ruttinger, P. Nuhn, W. Wohlrab, C. Huschka, Photochem. Photobiol. 73 (2001) 119.
[140] X.N. Pan, A.D. Bass, J.P. Jay-Gerin, L. Sanche, Icarus 172 (2004) 521.
[141] W.M. Dale, J.V. Davies, C.W. Gilbert, J.P. Keene, L.H. Gray, Biochem. J. 51 (1952) 268.
[142] D.A. Bahr, M. Fama, R.A. Vidal, R.A. Baragiola, J. Geophys. Res.: Planets 106 (2001) 33285.
[143] R.A. Baragiola, M.J. Loeffler, U. Raut, R.A. Vidal, C.D. Wilson, Radiat. Phys. Chem. 72 (2005) 187.
[144] M.H. Moore, R.L. Hudson, Icarus 145 (2000) 282.
[145] O. Gomis, G. Strazzulla, Icarus 177 (2005) 570.
[146] V. Mennella, M.E. Palumbo, G.A. Baratta, Astrophys. J. 615 (2004) 1073.
[147] M.E. Palumbo, A.C. Castorina, G. Strazzulla, Astron. Astrophys. 342 (1999) 551.
[148] M.E. Palumbo, Adv. Space Res. 20 (1997) 1637.
[149] G.A. Baratta, G. Leto, M.E. Palumbo, Astron. Astrophys. 384 (2002) 343.
[150] R.L. Hudson, M.H. Moore, J. Geophys. Res. E: Planets 12 (106) (2001) 33275.
[151] D.C. Knauth, B.-G. Andersson, S.R. McCandliss, H. Warren Moos, Nature 429 (2004) 636.
[152] G. Strazzulla, G.A. Baratta, M.E. Palumbo, M.A. Satorre, Nucl. Instrum. Meth. B 166/167 (2000) 13.
[153] M.H. Moore, R.L. Hudson, Icarus 161 (2003) 486.
[154] M.E. Palumbo, G. Strazzulla, Y.J. Pendleton, A.G.G.M. Tielens, Astrophys. J. 534 (2000) 801.
[155] X.Q. Wang, C.L. Shao, J.M. Yao, Z.L. Yu, Radiat. Phys. Chem. 59 (2000) 67.
[156] X.Q. Wang, J.W. Han, Z.L. Yu, Acta Biophys. Sin. 14 (1998) 337 (in Chinese).
[157] X.Q. Wang, Z.L. Yu, J. Phys. D: Appl. Phys. 36 (2003) 2027.
[158] Z.L. Yu, J.W. Han, X.Q. Wang, W.D. Huang, C.L. Shao, The Role of Radiation in the Origin and Evolution of Life, Conference Book, Viva Origino, 26, 1998, p. 175.
[159] S. Eon, F Culard, D. Sy, M. Charlier, M. Spotheim-Maurizot, Radiat. Res. 156 (2001) 110.
[160] M. Charlier, S. Eon, E. Seche, S. Bouffard, F. Culard, M. Spotheim-Maurizot, Biophys. J. 82 (2002) 2373.
[161] A.M. Foti, F. Milano, L. Torrisi, Nucl. Instrum. Meth. B 46 (1990) 361.
[162] A.M. Foti, G.A. Baratta, G. Leto, Europhys. Lett. 16 (1991) 201.
[163] A.M. Foti, G.A. Baratta, G. leto, G. Strazzulla, Infrared Phys. 31 (1991) 511.
[164] W.D. Huang, Z.L. Yu, Y.H. Zhang, Chem. Phys. 327 (1998) 223.
[165] G. Compagnini, A. Licciardello, L. Romano, O. Puglisi, Nucl. Instrum. Meth. B 116 (1996) 242.
[166] F.Z. Cui, S.Q. Sun, D.M. Zhang, Z.L. Ma, G.Q. Chen, Nucl. Instrum. Meth. B 169 (2000) 48.
[167] J.W. Han, Z.L. Yu, Acta Biophys. Sin. 14 (1998) 341 (in Chinese).
[168] C.L. Shao, Z.L. Yu, Radiat. Phys. Chem. 50 (1997) 595.
[169] Z.L. Yu, C.L. Shao, Radiat. Phys. Chem. 43 (1994) 349.
[170] F.Z. Cui, Y.B. Liu, D.M. Zhang, M.B. Tian, Radiat. Phys. Chem. 60 (2001) 35.
[171] F. Culard, A. Glain, G. de Vuyst, M. Spotheim-Maurizot, M. Charlier, J. Mol. Biol. 328 (2003) 1185.
[172] P. Ehrenfreund, W. Lrvine, L. Becker, J. Blank, J.R. Brucato, L. Colangeli, S. Derenne, D. Despois, A. Dutrey, H. Fraaije, A. Lazcano, T. Owen, F. Robert, International Space Science Institute ISSI-Team, Rep. Prog. Phys. 65 (2002) 1427.
[173] G.M. Munoz Caro, U.J. Meierhenrich, W.A. Schutte, B. Barbier, A. Arcones Segovia, H. Rosenbauer, W.H.-P. Thiemann, A. Brack, J.M. Greenberg, Nature 416 (2002) 403.

[174] M.P. Bernstein, J.P. Dworkin, S.A. Sandfor, G.W. Cooper, L.J. Allamandola, Nature 416 (2002) 401.
[175] M. Tuleta, L. Gabla, J. Madej, Phys. Rev. Lett. 87 (2001) 078103–78111.
[176] Windows to the Universe team. *Life on Earth*. Boulder, CO: ©2000–04 University Corporation of Atmospheric Research (UCAR), ©1995–1999, 2000 The Regents of the University of Michigan, December 4, 2002. Online available at: http://www.windows.ucar.edu (Jan 1, 2007).
[177] H.B. Shi, C.L. Shao, Z.L. Yu, Nucl. Instrum. Meth. B 183 (2001) 369.
[178] H.B. Shi, C.L. Shao, Z.L. Yu, Nucl. Instrum. Meth. B 194 (2002) 141.
[179] H.B. Shi, C.L. Shao, Z.L. Yu, Radiat. Phys. Chem. 62 (2001) 393.
[180] T. Schlatholter, F. Alvarado, S. Bari, R. Hoekstra, Phys. Scr. 73 (2006) C113.
[181] T. Schlatholter et al., J. Phys. B 2000.
[182] M. Imhoff, Z.W. Deng, M.A. Huels, Int. J. Mass Spectrom. 245 (2005) 68.
[183] T. Schlatholter, F. Alvarado, R. Hoekstra, Nucl. Instrum. Meth. B 233 (2005) 62.
[184] B. Manil, H. Lebius, B.A. Huber, D. Cormier, A. Pesnelle, Nucl. Instrum. Meth. B 205 (2003) 666.
[185] J. de Vries, R. Hoekstra, R. Morgenstern, T. Schlatholter, Phys. Scr. T 110 (2004) 336.
[186] J. de Vries, R. Hoekstra, R. Morgenstern, T. Schlatholter, Eur. Phys. J. D. 24 (2003) 161.
[187] J. de Vries, R. Hoekstra, R. Morgensterm, T. Schlatholter, J. Phys. B: At. Mol. Opt. Phys. 35 (2002) 4373.
[188] F. Alvarado, S. Bari, R. Hoekstra, T. Schlatholter, Phys. Chem. Chem. Phys. 8 (2006) 1922.
[189] S. Ptasinska, S.D. ifl, P. Scheier, T.D. Mark, J. Chem. Phys. 120 (2004) 8505–8511.
[190] H.W. Jochims, M. Schwell, H. Baumga rtel, S. Leach, Chem. Phys. 314 (2005) 263–282.
[191] K. Fujii, K. Akamatsu, A. Yokoya, Surf. Sci. 528 (2003) 249.
[192] J.F. Ward, I. Kuo, Int. J. Radiat. Biol. 23 (1973) 543.
[193] C.L. Shao, X.Q. Wang, Z.L. Yu, Radiat. Phys. Chem. 50 (1997) 561.
[194] C.L. Shao, Z.L. Yu, Radiat. Phys. Chem. 44 (1994) 651.
[195] C.L. Shao, Z.L. Yu, Radiat. Phys. Chem. 49 (1997) 337.
[196] K.L. Rinehart, Science 218 (1982) 254.
[197] S.J. Pachuta, R.G. Cooks, Chem. Rev. 87 (1987) 647.
[198] S. Schürch, E. Bernal-Méndez, C.J. Leumann, J. Am. Soc. Mass. Spectrom. 13 (2002) 936.
[199] S. Pan, K. Verhoeven, J.K. Lee, J. Am. Soc. Mass Spectrom. 16 (2005) 1853.
[200] S. Brons, K. Psonka, M. Heiss, E. Gudowska-Nowak, G. Taucher-Scholz, R. Neumann, Radiother. Oncol. 73 (Suppl. 2) (2004) S112.
[201] M. Murakami, H. Hirokawa, I. Hayata, J. Biochem. Biophys. Meth. 44 (2000) 31.
[202] C. Ruehlicke, D. Schneider, M. Schneider, R.D. Dubois, R. Balhorn, Nanotechnology 9 (1998) 251.
[203] H.G. Hansma, R. Golan, W. Hsieh, C.P. Lollo, P. Mullen-Ley, D. Kwoh, Nucleic Acids Res. 26 (1998) 2481.
[204] Y. Zhao, Z. Tan, Y.H. Du, G.Y. Qiu, Nucl. Instrum. Meth. B 211 (2003) 211.
[205] S. Lacombe, C. LeSech, V.A. Esaulov, Phys. Med. Biol. 49 (2004) N65.
[206] C. Giustranti, S. Rousset, E. Balanzat, E. Sage, Biochimie 82 (2000) 79.
[207] Q. Wang, G. Zhang, Y.H. Du, Y. Zhao, G.Y. Qiu, Mutat. Res.: Fund. Mol. M 528 (2003) 55.
[208] J.B. Yang, J.D. Wu, Z.H. Xu, Y.L. Yu, et al. Sci. China Ser. C 40. (1997).
[209] A. Tanaka, H. Watanabe, T. Shimizu, M. Inoue, M. Kikuchi, Y. Kobayashi, S. Tano, Nucl. Instrum. Meth. B 129 (1997) 42.
[210] http://www.dupont.com.
[211] V. Hable, G. Dollinger, C. Greubel, A. Hauptner, R. Krucken, S. Dietzel, T. Cremer, G.A. Drexler, A.A. Friedl, R. Lowe, Nucl. Instrum. Meth. B 245 (2006) 198.
[212] B.R. Hu, L.J. Wu, W. Han, L.L. Zhang, S.P. Chen, A. Xu, T.K. Hei, Z.L. Yu, Carcinogenesis 27 (2006) 245.
[213] S. Sangyuenyongpipat, T. Vilaithong, L.D. Yu, R. Yimnirun, P. Singjai, I.G. Brown, Solid State Phenom. 107 (2005) 47.
[214] S. Sangyuenyongpipat, L.D. Yu, N. Tondee, K. Wattanavatee, T. Vilaithong, C. Thongleurm, B. Phanchaisri, S.Anuntalabhochai, I.G. Brown, Proceedings of the 29th International Conference on Plasma Science, Banff, Alberta, Canada, May 26–30, 2002, IEEE Conference Record–Abstracts, Cat. No. 02CH37340, p. 310.
[215] R. Tanaka, T. Kamiya, T. Sakai, M. Fukuda, Y. Kobayashi, A. Tanaka, H. Watanabe, APAC98 Proceedings, http://www-proc.kek.jp/Contents.html.
[216] H.Y. Feng, L.J. Wu, A. Xu, B.R. Hu, T.K. Hei, Z.L. Yu, Cryobiology 49 (2004) 241.
[217] H.Y. Feng, X.L. Liu, H. Yuan, M.G. Kong, L.J. Wu, Y.J. Wu, Z.L. Yu, Proceedings of the 14th International. Conference on Surface Modification of Materials by Ion Beams, Kusadasi, Turkey, Sept 04–09, 2005, accepted.
[218] L.D. Yu, B. Phanchaisri, P. Apavatjrut, S. Anuntalabhochai, T. Vilaithong, I.G. Brown, Surf. Coat. Technol. 158/159 (2002) 146.
[219] S. Sangyuenyongpipat, T. Vilaithong, L.D. Yu, A. Verdaguer, I. Ratera, D.F. Ogletree, O.R. Monteiro, I.G. Brown, Nucl. Instrum. Meth. B 227 (2005) 289.
[220] P. Apavatjrut, C. Alisi, B. Phanchaisri, L.D. Yu, S. Anuntalabhochai, T. Vilaithong, Sci. Asia 29 (2003) 99.
[221] T. Vilaithong, L.D. Yu, C. Alisi, B. Phanchaisri, P. Apavatjrut, S. Anuntalabhochai, Surf. Coat. Technol. 128/129 (2000) 133.
[222] F. Watt, G.W. Grime, Principles and Applications of High Energy Ion Microbeams, Adam Hilger, Brostol, 1987.
[223] R.E. Zirkle, W. Bloom, Science 117 (1953) 487.
[224] W. Bloom, Rev. Modern Phys. 31 (1959) 66.
[225] G.J.F. Legge, Nucl. Instrum. Meth. B 130 (1997) 9.
[226] T.K. Hei, L.J. Wu, S.X. Liu, Proc. Natl. Acad. Sci. U.S.A. 94 (1997) 3765.
[227] M. Cholewa, A. Saint, G.J.F. Legge, Nucl. Instrum. Meth. B 130 (1997) 275.
[228] T. Sakai, Y. Naitoh, T. Kamiya, Y. Kobayashi, Nucl. Instrum. Meth. B 158 (1999) 250.

[229] D.J. Brenner, E.J. Hall, Radiat. Prot. Dosim. 99 (2002) 283.
[230] M. Folkard, B. Vojnovic, K.J. Hollis, Int. J. Radiat. Biol. 72 (1997) 387.
[231] A.D. Dymnikov, D.J. Brenner, G. Johnson, Rev. Sci. Instrum. 71 (2000) 1646.
[232] T. Butz, R.-H. Flagmeyer, J. Heitmann, Nucl. Instrum. Meth. B 161/163 (2000) 323.
[233] B.E. Fischer, M. Cholewa, N. Hitoshi, Nucl. Instrum. Meth. B 181 (2001) 60.
[234] G. Randers-Pehrson, C.R. Geard, G. Johnson, Radiat. Res. 156 (2001) 210.
[235] C. Michelet, Ph. Moretto, Ph. Barberet, Radiat. Res. 158 (2002) 370.
[236] G. Dollinger, G. Datzmann, A. Hauptner, Nucl. Instrum. Meth. B 210 (2003) 6.
[237] K.D. Greif, H.K. Brede, U. Giesen, Radiat. Res. 161 (2004) 89.
[238] M. Oikawa, T. Kamiya, M. Fukuda, Nucl. Instrum. Meth. B 210 (2003) 54.
[239] M. Cholewa, B.E. Fischer, M. Heiß, Nucl. Instrum. Meth. B 210 (2003) 296.
[240] M. Folkard, B. Vojnovic, S. Gilchrist, Nucl. Instrum. Meth. B 210 (2003) 302.
[241] The Radiological Research Accelerator Facility, RARAF Annual Report, Columbia University, USA, 2002.
[242] Z.W. Hu, Z.L. Yu, L.J. Wu, Nucl. Instrum. Meth. A 507 (2003) 617.
[243] X.F. Wang, L.Y. Chen, Z.W. Hu, X.H. Wang, J. Zhang, J. Li, L.J. Wu, S.H. Wang, Z.L. Yu, Chin. Phys. Lett. 21 (2004) 821.
[244] Ph. Moretto, C. Michelet, A. Balana, Nucl. Instrum. Meth. B 181 (2001) 104.
[245] R. Cherubini, M. Conzato, G. Galeazzi, Radiat. Res. 158 (2002) 371.
[246] A.W. Bigelow, G. Randers-Pehrson, D.J. Brenner, Rev. Sci. Instrum. 73 (2002) 770.
[247] B.E. Nelms, R.S. Maser, J.F. MacKay, Science 280 (1998) 590.
[248] B.H. Bransden, Rep. Prog. Phys. 35 (1972) 949.
[249] R.E. Johnson, E.T. Trevisani, J.H. Harberger, Phys. Med. Biol. 18 (1973) 287.
[250] P. Sigmund, L. Glazov, Nucl. Instrum. Meth. B 136–138 (1998) 47.
[251] A. Arnau, Nucl. Instrum. Meth. B 115 (1996) 2.
[252] C.L. Shao, A. Xu, Z.L. Yu, Nucl. Techn. 20 (1997) 70 (in Chinese).
[253] M.C. Bacchus-Montabonel, M. Labuda, Y.S. Tergiman, J.E. Sienkiewicz, Phys. Rev. A 72 (2005) 052706.
[254] J. de Vries, R. Hoekstra, R. Morgenstern, T. Schlatholter, Phys. Rev. Lett. 91 (2003) 053401.
[255] P. Sigmund, I.R. Behrisch (Eds.), Sputtering by Particle Bombardment, Springer-Verlag, Berlin, 1981.
[256] Z. Yu, J. Yang, Y. Wu, B. Cheng, J. He, Y. Huo, Nucl. Instrum. Meth. B 80/81 (1993) 1328.
[257] G. de Stasio, B.H. Frazer, M. Girasole, L.M. Wiese, E.K. Krasnowska, G. Greco, A. Serafino, T. Parasassi, Microsc. Res. Techn. 63 (2004) 115.
[258] L.W. Black, W.W. Newcomb, J.W. Boring, J.C. Brown, Proc. Natl. Acad. Sci. U.S.A. 82 (1985) 7960.
[259] S. Sangyuenyongpipat, L.D. Yu, T. Vilaithong, I.G. Brown, Nucl. Instrum. Meth. B 242 (2006) 8.
[260] M.C. Salvadori, F.S. Teixeira, I.G. Brown, Nucl. Instrum. Meth. B 243 (2006) 250.
[261] J.T. Van Dongen, A.M.H. Ammerlaan, M. Wouterlood, A.C. Van Aelst, A.C. Borstlap, Ann. Bot.: Lond. 91 (2003) 729.
[262] J.W. Han, Z.L. Yu, Acta Biophys. Sin. 14 (1998) 757.
[263] T. Lu, W.Z. Yu, H.Y. Zhou, G.H. Zhu, X.F. Wang, C. Wang, Chin. Phys. 10 (2001) 0145.
[264] Y.Y. Xia, C.Y. Tan, Y.G. Mu, R.J. Wang, J.H. Zhang, X.D. Liu, J.T. Liu, Z.L. Yu, Phys. Lett. A 256 (1999) 205.
[265] Y.G. Wang, G.H. Du, J.M. Xue, F. Liu, S.X. Wang, S. Yan, W.J. Zhao, Phys. Lett. A 300 (2002) 611.
[266] Y.G. Wang, Q.Z. Chen, J.M. Xue, G.H. Du, H.L. Qin, W.M. Zhang, S. Yan, W.J. Zhao, Nucl. Instrum. Meth. B 245 (2006) 306.
[267] J.M. Xue, Y.G. Wang, F. Liu, S.X. Wang, S. Yan, W.J. Zhao, Surf. Coat. Technol. 128/129 (2000) 139.
[268] J.M. Xue, Y. Wang, G. Du, S. Yan, W. Zhao, Nucl. Instrum. Meth. B 198 (2002) 113.
[269] F. Liu, Y.G. Wang, J.M. Xue, S.X. Wang, S. Yan, W.J. Zhao, Phys. Lett. A 283 (2001) 360.
[270] Z.Q. Wei, H.M. Xie, G.W. Han, W.J. Li, Nucl. Instrum. Meth. B 95 (1993) 371.
[271] C. Wang, T. Lu, X.F. Wang, H.Y. Zhou, G.H. Zhu, Acta Biophys. Sin. 17 (2001) 351 (in Chinese).
[272] L.D. Yu, T. Vilaithong, B. Phanchaisri, P. Apavatjrut, S. Anuntalabhochai, P. Evans, I.G. Brown, Nucl. Instrum. Meth. B 206 (2003) 586.
[273] G.H. Zhu, H.Y. Zhou, X.F. Wang, C. Wang, G.F. Wang, Y.L. Zhou, R.Y. Chen, S.L. Wen, T. Lu, Nucl. Techn. 24 (2001) 456 (in Chinese).
[274] J.Y. Xie, H.Y. Zhou, P. Wang, X.J. Ding, Z.G. Liu, H. Song, T. Lu, G.H. Zhu, Acta Phys. Sin. 52 (2003) 2530 (Abstract in English).
[275] T. Ishitani, T. Yaguchi, Microsc. Res. Techn. 35 (1996) 320.
[276] K. Yonehara, N. Baba, K. Kanaya, J. Electron Microsc. Techn. 12 (1989) 71.
[277] J. Yahiro, T. Nagato, Microsc. Res. Techn. 67 (2005) 240.
[278] A.L. Robinson, Science 225 (1984) 1139.
[279] N. Rizk, I. Bendet, The 30th Annu. Proc. Electron Microsc. Soc. Am., 1972.
[280] E.C. Mendelson, W.W. Newcomb, J.C. Brown, J. Virol. 66 (1992) 2226.
[281] I. Bendet, N. Rizk, Biophys. J. 16 (1976) 357.
[282] J.C. Brown, W.W. Newcomb, J. Virol. 60 (1986) 564.
[283] W.W. Newcomb, J.W. Boring, J.C. Brown, J. Virol. 51 (1984) 52.
[284] M.E. Fromm, L.P. Taylor, V. Walbot, Nature 319 (1986) 791.
[285] V. Vasil, A. Castillo, M.E. Fromm, I. Vasil, Biotechnology 10 (1992) 667.
[286] T.E. McKnight, A.V. Melechko, D.K. Hensley, D.G.J. Mann, G.D. Griffin, M.L. Simpson, Nano Lett. 4 (2004) 1213.
[287] J. Sambrook, D.W. Russell, Molecular Cloning: A Laboratory Manual, Cold Spring Harbor Laboratory Press, Cold Spring Harbor, New York, 2001.
[288] S.B. Gelvin, Microbiol. Mol. Biol. Rev. 67 (2003) 16.

[289] I.A. Hope, C. Elegans, A Practical Approach, Oxford University Press, Oxford, 1999.
[290] Y.J. Wu, Studies on ion implantation induced biological effects in rice and ion beam assisted plant gene transfer, Ph.D. Thesis, Institute of Plasma Physics, Chinese Academy of Sciences, Hefei, 1993.
[291] T. Vilaithong, L.D. Yu, P. Apavatjrut, B. Phanchaisri, S. Sangyuenyongpipat, S. Anuntalabhochai, I.G. Brown, Radiat. Phys. Chem. 71 (2004) 927.
[292] B. Po, Z.L. Yu, Plasma Sci. Technol. 7 (2005) 2693.
[293] J.B. Yang, L.J. Wu, J.D. Wu, Y.J. Wu, Z.L. Yu, Z.H. Xu, Chin. Sci. Bull. 39 (1994) 1530.
[294] H. Li, L.F. Wu, Z.L. Yu, 199, Acta Agric. Nucleatea Sin. 15 (2001) (in Chinese).
[295] L.F. Wu, H. Li, S.D. Song, H.Y. Feng, Z.L. Yu, Genet. Sin. 27 (2000) 982 (in Chinese).
[296] L.F. Wu, H. Li, H.Y. Feng, L.J. Wu, Z.L. Yu, Chin. Sci. Bull. 46 (2001) 318.
[297] Y. Hase, A. Tanaka, I. Narumi, H. Watanabe, M. Inoue, JAERI Rev. 98-016 (1998) 81.
[298] W.J. Zheng, Y. Wang, Z.L. Yu, Acta Laser Biol. Sin. 9 (2000) 241 (in Chinese).
[299] B.J. Cheng, O.Y. Tian, Z.W. Yao, J. Anhui Agric. Univ. 19–22 (Suppl.) (1993) (in Chinese).
[300] S. Anuntalabhochai, R. Chandej, B. Phanchaisri, L.D. Yu, T. Vilaithong, I.G. Brown, Appl. Phys. Lett. 78 (2001) 2393.
[301] Y.J. Wu, Y. Zhang, J.D. Wu, J.P. Tong, H. Li, L.Y. Zheng, M. Song, Z.L. Yu, Plasma Sci. Technol. 7 (2005) 2785.
[302] J.D. Wu, X.F. Wang, Y.J. Wu, L.Y. Zhen, J. Anhui Agric. Sci. 25 (1997) 112 (in Chinese).
[303] L.Y. Zhen, J.D. Wu, Y.J. Wu, G.P. Tong, Acta Agron. Sin. 28 (2002) 401 (in Chinese).
[304] H. Li, L.F. Wu, D.J. Song, Z.L. Yu, Y.J. Wu, Acta Laser Biol. Sin. 8 (1999) 261 (in Chinese).
[305] H.B. Wang, X.W. Gao, J.H. Guo, Q.C. Huang, Z.L. Yu, Plasma Sci. Technol. 4 (2002) 1591.
[306] D.J. Song, R.L. Chen, L.F. Wu, C. Wang, J. Zhang, Z.L. Yu, Progr. Nat. Sci. 11 (2001) 557.
[307] P.H. Mao, K. Lou, X. Jin, Total DNA of Chinese ephedra transfered to yeast by ion beam. Chinese patent No.200610011402.7, 2006.
[308] M. Barinaga, Science 273 (1996) 735.
[309] D. Voet, J.G. Voet, Biochemistry, 2nd ed., John Wiley & Sons, New York, 1995.
[310] T. Morishita, H. Yamaguchi, K. Degi, N. Shikazono, Y. Hase, A. Tanka, A. Abe, Nucl. Instrum. Meth. B 206 (2003) 565.
[311] Okamura, N. Yasuno, M. Ohtsuka, A. Tanaka, N. Shikazono, Y. Hase, Nucl. Instrum. Meth. B 206 (2003) 574.
[312] H. Yamaguchi, S. Nagatomi, T. Morishita, K. Degi, A. Tanaka, N. Shikazono, Y. Hase, Nucl. Instrum. Meth. B 206 (2003) 561.
[313] B.M. Liu, T.P. Tong, J.D. Wu, Z.L. Yu, Y. Zhang, L.Y. Zheng, D.H. She, C. Cheng, M. Song, Y.J. Wu, Mol. Plant Breed. 2 (2004) 326, (in Chinese).
[314] L.Y. Zhen, Y.J. Wu, J.D. Wu, J. Anhui Agric. Sci. 29 (2001) 137 (in Chinese).
[315] X.M. Shi, K. Li, Y.L. Nie, G.F. Zhang, Front. Biol. China 1 (2006) 41.
[316] J.B. Wang, Y.J. Wu, Z.L. Yu, A new soybean [*Glycine max* (L.) Merr.] mutant with multifoliolate compound leaf acquired by ion beam irradiation, Nucl. Instrum. Meth. B, in press, 2007.
[317] F.Q. Chang, X.M. Liu, Y.X. Li, G.X. Jia, J.J. Ma, G.S. Liu, Z.Q. Zhu, Sci. China Ser. C 46 (2003) 503.
[318] B.J. Cheng, X.Z. Kan, S.W. Zhu, P.J. Li, Plasma Sci. Technol. 3 (2001) 659.
[319] G.F. Zhang, K. Li, X.M. Shi, Y.L. Nie, J. Zhang, H.Y. Zhou, T. Lu, Plasma Sci. Technol. 7 (2005) 2880.
[320] G.F. Xu, Y.H. Gu, Plasma Sci. Technol. 3 (2001) 835.
[321] G.J. Dong, W.D. Pan, G.S. Liu, J. Biosci. 31 (2006) 247.
[322] P. Bian, M. Xu, Z.L. Yu, Proceedings of the 14th International Conference on Surface Modification of Materials by Ion Beams, Kusadasi, Turkey, Sept 04–09, 2005, accepted.
[323] G.P. Lin, J. Anhui Agric. Univ. 18 (1991) 317 (in Chinese).
[324] M. Shen, C.L. Wang, Q.F. Chen, Acta Agric. Nucleatae Sin. 11 (1997) 141 (in Chinese).
[325] Y.J. Wu, Y. Zhang, Y. Wang, M. Song, Z.L. Yu, Solid State Phenom. 107 (2005) 37.
[326] Y.J. Wu, J. Nucl.-Agric. Sci. 11 (1990) 154 (in Chinese).
[327] Y. Zhang, Y.J. Wu, J.D. Wu, J.P. Tong, L.Y. Zhen, J. Anhui Agric. Sci. 29 (2001) 565. (in Chinese).
[328] Y. Wu, J. Wu, Y. Zhang, A new rapid crop lipoxygenase isoenzymes detective technique. China Patent Bureau, Invention Patent Communique 17 (2001) 21 (in Chinese).
[329] Y. Zhang, Y.J. Wu, J.D. Wu, J.P. Tong, L.Y. Zheng, J. Chin. Cereals Oils Assoc. 18 (2003) 1 (in Chinese).
[330] Y. Zhang, Z.L. Yu, Y.X. Lu, Y. Wang, D.H. She, M. Song, Y.J. Wu, J. Stored Prod. Res. 43 (2007) 87.
[331] J.K. Li, Y. Zhang, Y.J. Wu, Y.J. Wang, J.Y. Jiang, M. Song, Z.L. Yu, Superior storage stability in low lipoxygenase maize varieties, J. Stored Prod. Res., in press, 2007.
[332] Y.P. Cai, H.Z. Tao, B.J. Cheng, J. Anhui Agric. Univ. 23 (1992) 474 (in Chinese).
[333] H.Z. Tao, Z. Li, C.P. Meng, Y.P. Cai, Z.Y. Cheng, B.J. Cheng, Y.Q. Zhang, Y.P. Fang, Y.P. Zhang, Acta Agron. Sin. 26 (2000) 65 (in Chinese).
[334] D. Jackson, B. Veit, S. Hake, Development 120 (1994) 405.
[335] Q.Y. Tian, B.J. Cheng, Anhui Agric. Sci. 22 (1994) 216 (in Chinese).
[336] C.X. Xie, S.W. Zhu, P.J. Li, B.J. Cheng, Z.L. Yu, High Technol. Lett. 8 (2002) 38 (in Chinese).
[337] Y.Q. Tan, H.Y. Jiang, Z. Wang, S.W. Zhu, B.J. Cheng, Gene, in revision.
[338] G.J. Zhu, Z.X. Wang, Experimental Technique Handbook in Industrial Microbiology, China Light Industry Publishing House, Beijing, 1994 p. 384 (in Chinese).
[339] D.Q. Zhou, Principle of Microbiology, High Education Publishing House, Beijing, 1993, p. 244 (in Chinese).
[340] D.J. Song, Z.L. Yu, Plasma Sci. Technol. 2 (2000) 415.
[341] D.J. Song, R.L. Chen, C.L. Shao, L.J. Wu, Z.L. Yu, Plasma Sci. Technol. 2 (2000) 491.
[342] D.J. Song, L.F. Wu, L.J. Wu, Z.L. Yu, Plasma Sci. Technol. 3 (2001) 665.

[343] B. Phanchaisri, L.D. Yu, S. Anuntalabhochai, R. Chandej, P. Apavatjrut, T. Vilaithong, I.G. Brown, Surf. Coat. Technol. 158/159 (2002) 624.
[344] C.X. Xie, J.H. Guo, B.J. Chen, Z.L. Yu, Plasma Sci. Technol. 5 (2003) 1677.
[345] M.L. Tang, S.C. Wang, T. Wang, S.G. Zhao, Y.J. Wu, L.J. Wu, Z.L. Yu, Mutat. Res-Fund. Mol. M 602 (2006) 163.
[346] M. Wu, S.C. Li, J.M. Yao, R.R. Pan, Z.L. Yu, World J. Microbiol. Biol. 21 (2005) 1045.
[347] S.C. Li, M. Wu, J.M. Yao, R.R. Pan, Z.L. Yu, Plasma Sci. Technol. 7 (2005) 2697.
[348] T. Reichstein, A. Grussner, Helv. Chim. Acta 17 (1934) 311.
[349] Competition Commission, The production of Vitamin C, in: Reports Published 2001 (Series Cm 5209), 2001, online available: http://www.competition-commission.org.uk/rep_pub/reports/.
[350] J. Boudrant, Enzyme Microb. Technol. 12 (1990) 322.
[351] K. Kieslich, Proceedings of the Third European Congress on Biotechnology IV, Munich, Germany, Sept 10–14, 1984, pp. 39–72.
[352] S. Lu, S. Huang, J. Yu, Chem. Reaction Engineering and Technology 1 (1985) 72 (in Chinese).
[353] W. Ning, Z. Tao, C. Wang, S. Wang, Z. Yan, G. Yu, Fermentation process for producing 2-keto-L-gulonic acid, European Patent EP 278447 (1988).
[354] I. Nogami, O.M. Shirafuji, T. Yamaguchi, A method for producing 2-keto-L-gulonic acid, European Patent EP 221707 (1987).
[355] G. Yin, W. Lin, C. Qiao, Q. Ye, Acta Microbiol. Sin. 41 (2001) 709 (in Chinese).
[356] A. Xu, J. Yao, L. Yu, S. Lv, J. Wang, B. Yan, Z. Yu, J. Appl. Microbiol. 96 (2004) 1317.
[357] A. Xu, J.M. Yao, Z.L. Yu, Ind. Microbiol. 29 (1999) 16 (in Chinese).
[358] L. Yu, Z.L. Yu, High Technol. Lett. 11 (2002) 41 (in Chinese).
[359] C. Torres, C. Otero, Enzyme Microb. Technol. 29 (2001) 3.
[360] S.A. Waksman, I.J. Hutchings, J. Am. Chem. Soc 59 (1937) 545.
[361] C.M. Ge, S.B. Gu, X.H. Zhou, J. Microbiol. Biotechnol 14 (2004) 363.
[362] X.H. Zhou, C.M. Ge, J.M. Yao, R.R. Pan, Z.L. Yu, Plasma Sci. Technol. 7 (2005) 3078.
[363] X. Zhao, L.Q. Zhao, C.H. Liu, H. Xie, Biotechnology 14 (2004) 24 (in Chinese).
[364] L. Yu, J. Zhou, Z.L. Yu, Acta Laser Biol. Sin. 14 (2005) 184 (in Chinese).
[365] I. Gill, R. Valivety, Trends Biotechnol. 15 (1997) 401.
[366] S.E. Carlson, S.H. Werkman, J.M. Peeples, R.J. Cooke, E.A. Tolley, Proc. Natl. Acad. Sci. U.S.A. 90 (1993) 1073–1077.
[367] T.J. Ahern, J. Am. Oil Chem. Soc. 61 (1984) 1754–1757.
[368] A. Singh, O.P. Ward, Appl. Microbiol. Biotechnol. 48 (1997) 1.
[369] C. Ratledge, Biochimie 86 (2004) 807.
[370] http://www.alking.com.cn/English/aboutus.htm.
[371] C.L. Yuan, J. Wang, Y. Shang, G.H. Gong, J.M. Yao, Z.L. Yu, Food Technol. Biotechnol. 40 (2002) 311.
[372] C.L. Yuan, J. Wang, J.M. Yao, Z.L. Yu, G.H. Gong, Y. Shang, Y. Qian, High Technol. Lett. 6 (2003) 22 (in Chinese).
[373] US EPA, Office of Pesticide Programs, Biopesticides and Pollution Prevention Division, Biopesticide Registration Document *Bacillus subtilis* Strain QST 713 (PC Code 006479), 2002.
[374] S. Gielen, R. Aerts, B. Seels, Commun. Agric. Appl. Biol. Sci. 69 (2004) 631.
[375] J. Liu, J.M. Yao, Plasma Sci. Technol. 6 (2004) 2433.
[376] J. Liu, M. Liu, J. Wang, J.M. Yao, R.R. Pan, Z.L. Yu, Appl. Microbiol. Biotechnol. 69 (2005) 223.
[377] J. Liu, J. Wang, J.M. Yao, R.R. Pan, Z.L. Yu, Acta Microbiol. Sin. 44 (2004) 511 (in Chinese).
[378] X.H. Cao, B.b. Du, M.F. Lu, J. Chin. Inst. Food Sci. Technol. 5 (2005) 132.
[379] J.S. Gong, Q.J. Liu, L. Xiao, J.M. Yao, Food Ferment. Ind. 26 (1999) 9.
[380] Y.P. Wang, F.Z. Wang, Z.W. Li, J. Wu, L.H. Chen, G.Y. Qin, Y.P. Huo, J. Zhengzhou Inst. Technol. 24 (2003) 71 (in Chinese).
[381] X.L. Chen, X.Y. Tang, L.Y. long, Acta Laser Biol. Sin. 14 (2005) 173.
[382] Y.Q. Hui, J.X. Huang, S.X. Kong, J. Northwest Univ. (Nat. Sci. Ed.) 31 (2001) 1.
[383] S.L. Wang, L.J. Yang, Y.C. Chen, m.J. Chi, X.C. Jia, J. Zhengzhou Inst. Light Ind. (Nat. Sci. Ed.) 19 (2004) 19 (in Chinese).
[384] F.M. Yi, X.H. wu, S.Y. Feng, W.M. Chen, Acta Laser Biol. Sin. 11 (2002) 137 (in Chinese).
[385] S.B. Gu, J.M. Yao, Q.P. Yuan, P.J. Xue, Z.M. Zheng, L. Wang, Z.L. Yu, Appl. Microbiol. Biotechnol. 72 (2006) 456.
[386] C.X. Su, W. Zhou, Y.H. Fan, L. Wang, S.G. Zhao, Z.L. Yu, J. Ind. Microbiol. Biotechnol. 33 (2006) 1037.
[387] J. Wang, H.B. Jiang, J.M. Yao, X.L. Xue, H.J. Xie, Z.L. Liu, J. Microbiol. 18 (1998) 25 (in Chinese).
[388] H.B. Jiang, J. Wang, J.M. Yao, Z.L. Yu, Ind. Microbiol. 30 (200) 1 (in Chinese).
[389] L.F. Yang, L. Yu, L. Zhang, Chem. Bioeng. 1 (2005) 16 (in Chinese).
[390] Z.H. Chen, Q. Ye, G.L. Yin, Microbiology 27 (2000) 174. (in Chinese).
[391] J.R. Sun, J. Zhang, Z.W. Mao, Ind. Microbiol. 32 (2002) 33 (in Chinese).
[392] H. Yang, H.Q. Liang, W. Liao, H.Z. Zhou, Ind. Microbiol. 33 (2003) 30 (in Chinese).
[393] W.J. Zhen, Y. Tuersan, Q. Li, S.F. Zhang, X.X. Zeng, B.H. Wu, Seed 120 (2002) 15 (in Chinese).
[394] T. Shen, H.Z. Chen, Y.Y. Peng, Y. Liu, J.M. Liu, China Condiment 9 (2002) 24 (in Chinese).
[395] L.M. Zheng, J.H. Yu, Y.H. Zhu, L. Wang, X.B. Zhan, Jiangsu Food Ferment. 114 (2003) 3 (in Chinese).
[396] J.L. Sang, L.H. Zhu, X.H. Li, Y.F. Shi, Bull. Sci. Technol. 18 (2002) 63.
[397] C.X. Tian, Y. Meng, X.M. Jia, H. Li, S.M. Zhu, J. China Antibiotic 30 (2005) 505 (in Chinese).
[398] X. Wu, W.P. Xu, L. Wang, Shanghai Chem. Ind. 21 (2002) 21 (in Chinese).
[399] H.Y. Zhao, Y. Li, H.J. Pei, T.C. Zhang, J. Tianjin Inst. Technol. 17 (2001) 14 (in Chinese).
[400] D. Xiang, J. Li, J.M. Yao, Z.L. Yu, Acta Laser Biol. Sin. 11 (2002) 276.

[401] F.Z. Wang, J. Wu, Z.W. Li, Y.P. Wang, G.F. Dai, Q.X. Liang, J. Zhengzhou Univ. 33 (2001) 50 (in Chinese).
[402] Q. Wang, S.Z. Wang, Z.L. Kan, J. Fu, W. Zhang, Hebei Med. J. 27 (2005) 709 (in Chinese).
[403] Y. Chen, Z.X. Lin, Z.Y. Zou, F. Zhang, D. Liu, X.H. Liu, J.Z. Tang, W.M. Zhu, B. Huang, Nucl. Instrum. Meth. B 140 (1998) 341.
[404] Y. Yu, J.M. Yao, L. Yu, Z.L. Yu, k. Li, J. Grad. School Chin. Acad. Sci. 19 (2002) 443 (in Chinese).
[405] X. Zhang, S.L. Wang, C.T. Chen, J. Wei, S.Q. Chen, J. Wuxi Univ. Light Ind. 21 (2002) 347 (in Chinese).